Numerical and experimental study of a new laser-driven proton accelerator

Arthur Hirsch-Passicos

THÈSE PRÉSENTÉE
POUR OBTENIR LE GRADE DE

DOCTEUR
DE L'UNIVERSITÉ DE BORDEAUX

ÉCOLE DOCTORALE SCIENCES PHYSIQUES ET DE L'INGENIEUR

ASTROPHYSIQUE, PLASMAS, NUCLEAIRE

Par **Arthur HIRSCH-PASSICOS**

Étude numérique et expérimentale d'un nouvel accélérateur de protons par voie laser

Sous la direction de :
Emmanuel D'HUMIÈRES

Soutenue le 15 Décembre 2023

Membres du jury :

M. Emmanuel D'HUMIÈRES	Directeur de Recherche	Université de Bordeaux	Directeur
M. Yves ELSKENS	Professeur	Université Aix-Marseille	Examinateur
M. Dino JAROSZYNSKI	Professeur	Strathclyde University	Rapporteur
Mme. Rachel NUTER	Ingénieure-Chercheure	CEA-CESTA	Examinatrice
Mme. Caterina RICONDA	Professeure	Sorbonne Université	Rapportrice
M. João Jorge SANTOS	Professeur	Université de Bordeaux	Président du Jury

Membres invités :

M. Matthieu BARDON	Ingénieur Chercheur	CEA-CESTA	Co-encadrant
M. Vladimir TIKHONCHUK	Professeur Emérite	Université de Bordeaux	Invité

Étude numérique et expérimentale d'un nouvel accélérateur de protons par voie laser

Résumé : Dans le domaine de l'accélération d'ions par interaction laser-plasma, le Target Normal Sheath Acceleration (TNSA) est le schéma d'accélération le plus robuste. Cependant, il présente deux limitations majeures : une grande ouverture angulaire et un spectre d'énergie décroissant de manière exponentielle. Pour surmonter ces limitations, un nouveau schéma utilisant des cibles hélicoïdales (HC) a été proposé. Les cibles hélicoïdales permettent de focaliser et de post-accelérer un faisceau de protons généré par TNSA. Ce schéma utilise le courant de décharge autogénéré par l'éjection de charges lors de l'interaction laser-plasma. Le courant est dirigé à travers une cibles hélicoïdale conductrice, générant une impulsion électromagnétique (EMP) à l'intérieur de l'hélice qui va focaliser, post-accelérer et buncher une partie du faisceau de protons TNSA. Ce schéma a été validé pour des cibles hélicoïdales de pas et de diamètre constants lors de plusieurs expériences et présente un grand intérêt pour de nombreuses applications, allant du chauffage isochore pour l'étude de la matière dense (WDM) à la production de radio-isotopes pour la médecine, en passant par la production de neutrons pour l'astrophysique.

Le travail présenté dans ce manuscrit commence par une étude expérimentale et numérique de l'impact de la géométrie des cibles hélicoïdales sur le faisceau de protons TNSA. La charge d'espace des protons est également identifiée comme le principal processus physique responsable du rendement limité des cibles hélicoïdales.

La deuxième partie du travail présenté est une caractérisation du faisceau de protons lors de sa propagation à l'intérieur des cibles hélicoïdales afin de modéliser la charge d'espace d'un faisceau de protons TNSA à travers l'hélice. L'implémentation de ce modèle dans le code réduit DoPPLIGHT est décrite dans cette partie.

Enfin, ce manuscrit présente le développement d'un nouveau concept de cibles hélicoïdales entourées d'un tube métallique afin de réduire fortement la dispersion du courant de décharge pendant sa propagation le long de l'hélice. Les simulations Particle-In-Cell (PIC) ainsi que les résultats de DoPPLIGHT montrent un fort effet de bunching au-dessus et en dessous de l'énergie caractéristique de la cible hélicoïdale. Ce nouveau schéma ouvre la voie à de nouvelles géométries de cibles hélicoïdales avec des pas variables dans le but d'améliorer l'énergie de coupure des protons.

Mots-clés : Accélération d'ions par voie laser, Cible hélicoïdale, Charge d'espace, Propagation d'impulsion dans un guide d'ondes.

Numerical and experimental study of a new laser-driven proton accelerator

Abstract: In the domain of laser-driven ion acceleration, the Target Normal Sheath Acceleration (TNSA) is the most robust acceleration scheme. However, it suffers from two major limitations: a large angular opening and an exponentially decreasing energy spectrum. To overcome these limitations, a new scheme using helical coils (HC) was proposed. HC targets allow us to focus and post-accelerate a proton beam generated by TNSA. This scheme uses the discharge current self-generated by the charge ejection from the laser-plasma interaction. The current is driven through a conducting HC, generating an electro-magnetic pulse (EMP) inside the coil which can focus, post-accelerate and bunch part of the TNSA proton beam. This scheme was validated for constant pitch and diameter HC on several experiments and is of great interest for numerous applications, from isochoric heating for warm dense matter (WDM) study, radio-isotope production for medecine, or neutron production for astrophysics.

The work presented in this manuscript start with an experimental and numerical study of the impact of the HC geometry on the TNSA proton beam. The proton space charge is also identified as the main physical process responsible for the limited yield of the HC.

The second part of the work presented is a characterisation of the proton beam during its propagation inside the HC in order to model the space charge of a TNSA proton beam through the helix. The implementation of this model in the reduced code DoPPLIGHT is described in this part.

Finally, this manuscript presents the development of a new HC design surrounded by a metallic tube in order to strongly reduce the discharge current dispersion during its propagation along the helix. The Particle-In-Cell (PIC) simulations as well as the results from DoPPLIGHT show a strong bunching effect above and under the characteristic energy of the HC. This new scheme opens the door to new HC geometries with varying pitches in order to improve the proton cut-off energy.

Keywords: Laser-driven ion acceleration, Helical coil target, Space charge, Pulse propagation in a waveguide.

Centre Lasers Intenses et Applications
UMR 5107 Université de Bordeaux-CNRS-CEA, 33405 Talence, France.

Science is not about building a body of known 'facts'. It is a method for asking awkward questions and subjecting them to a reality-check, thus avoiding the human tendency to believe whatever makes us feel good.

Terry Pratchett

Remerciements

Je tiens tout d'abord à remercier mes encadrants et directeurs de thèse Matthieu Bardon et Emmanuel d'Humières de m'avoir offert l'opportunité de mener ce travail qui m'a passionné et occupé durant les trois dernières années (et quelques mois en supplément). Merci pour votre contact humain, tous vos conseils et votre expérience que vous m'avez transmise en partie. Vous m'avez guidé sur une partie de ce chemin qu'est la recherche académique et je vous en suis si reconnaissant. Je ne peux pas non plus parler de mon encadrant sans remercier Vladimir Tikhonchuk, une source de savoir intarissable tout au long des nombreuses réunions que nous avons eu et qui m'a fait l'honneur d'être membre de mon jury en tant qu'invité.

Je suis honoré en particulier Matthieu d'avoir été ton premier thésard, et de t'avoir suivi du CESTA au CELIA. Je suis le premier d'une lignée qui s'annonce déjà longue j'en suis sûr, qui devront tous passé par le rite du karaoké au forum ILP ou de la bière après une bonne nouvelle telle un proposal accepté, un article enfin fini ou trois mois de calcul qui se débloquent enfin. Du début à la fin de cette thèse j'ai pu compter sur ta disponibilité, ta bonne humeur et ton expérience pour m'épauler.

Je remercie tout autant ma famille qui m'a soutenu depuis le plus jeune âge, me poussant à explorer les sujets qui m'intéressaient, à découvrir le monde et à m'interroger. Papa, Maman, merci pour tout ce que vous m'avez transmis : cet amour des mots transmis sur le papier, celui des voyages et de l'oeil toujours ouvert pour absorber la beauté du monde qui nous entoure. Je n'aurais jamais pu atteindre ce titre de Docteur si vous ne m'aviez inculqué toutes ces valeurs et cette curiosité. Merci Maureen, la meilleure petite soeur que je n'aurais jamais pu imaginer. Merci pour ton soutien, pour ton humour incisif (surtout envers ma personne) ainsi que pour les séances de kinésithérapie qui m'auront permis de me remettre de l'intensité de la vie de thésard.

Cette thèse est aussi dûe à toi Lionel. Dr Hirsch premier du nom. Tu es l'une des principales raisons qui m'ont mené vers ce moment. Je me souviens encore avec des étoiles dans les yeux de mon stage de 3ème dans ton laboratoire. Ce premier contact avec la recherche, celui qui m'a fait dire avant même mes 15 ans : "C'est ce que je ferai plus tard". Je ne te remercierai jamais assez pour ce stage prémonitoire dans l'université où j'ai passé ces années de thèse.

Merci aussi à vous tous : Papi, Mamie Hélène, Mamie Cécile, Pascale, Alain, Laurence, Gauthier, Mathilde, Clara, Samuel, Maria et Kévin. Pour votre soutien depuis maintenant plus de 25 ans (presque 30 ans diront certaines mauvaises langues), dans les bons moments comme dans les plus durs. Merci d'avoir été des propriétaires incroyables, des catsitters dévoués, des partenaires d'escape games et de tellement de conversations lors d'un repas de famille.

Et pour finir les remerciements à la famille, même si tu ne pourras jamais lire ces mots, merci Riley. Dernière arrivée dans la famille durant cette thèse, tu as rendu ces

nuits de questionnement sur la nature d'un ressort et de rédaction beaucoup plus douces. Tes ronronnements le long de ma jambe se retrouvent dans les mots de ce manuscrit.

Je tiens aussi à profondément remercier mon jury, en particulier Caterina Riconda et Dino Jaroszinsky d'avoir accepté ce rôle de rapporteur et de votre retour. Merci aussi à Yves Elskens, Rachel Nuter et Joao Santos d'avoir pris le temps de lire ma thèse et votre présence.

Merci à tous mes collègues du LSEM au CEA-CESTA et du CELIA pour leur apport durant ces trois années de thèse. Que ce soit autour de la machine à café, sur la terasse du CELIA, en salle de réunion, en salle de manipulation ou à l'atelier. Je tiens tout particulièrement à remercier Stéphane Coudert et Romain Liotard, mes deux co-bureaux, pour les discussions, les moments de pause essentiels et la chaleur apportée.

Merci en particulier à tous les gens au CELIA et au CESTA avec qui j'ai pu collaborer pendant ces trois années et dont l'expérience et la vision des choses ont éclairé le chemin de ma thèse : Olivier Cessenat à qui je dois des centaines de milliers d'heure de calcul et Laurent Merziau qui malgré les délais horriblement courts que je lui imposais a sauvé mes expériences. Sans oublier Jean-Luc Feugeas, Morad Bentayeb, Äli Joundi et Paul Canel qui m'ont permis de découvrir ce monde qui peut paraître totalement contre-intuitif qu'est celui des réseaux de neurones.

Je tiens aussi à remercier tous les membres de la collaboration avec le PIIM et Thalès sans qui cette thèse n'aurait pas été la même : Yves Elskens, Frédéric André, Damien Minenna, Khalil Aliane, Fabrice Doveil et Alexandre Poyé.

Et surtout, merci à toi Clément. Merci d'être le prochain à porter le flambeau. Cette année à travailler à tes côtés m'a montré que tu étais l'homme de la situation et je suis fier de te transmettre la flamme. Je sens qu'entre tes équations, les ressorts se porteront à merveille.

Merci enfin aux amis, d'où qu'ils viennent. A tous les non-permanents du SMMS : Juliette, Amandine, Luc, Lucas, Bruno, Damien, Julien. Merci pour l'ambiance autour d'une des nombreuses pauses café à l'arrivée de la navette et toutes les discussions autour de celles-ci.

A toute la clique du CELIA et nos soirées à boire des bières, déguster des raclettes ou jouer à lancer des dés autour d'une table, merci pour ces moments de rire, de danse à la Tencha et de camaraderie. Merci Romain, Paul, Diego, Duncan, Edoardo, Clément, Ali, Howel, Corisande, Alana, Alexandre, Morad, Margaux, Thomas, Arnaud, Kristal, Florent, Diluka, Marine, Christos, Philip, Tadeas, Olena et Guillaume.

Merci à tous mes amis en dehors des laboratoires. En particulier Florian et Gaëlle, une paire à laquelle je tiens beaucoup, que ce soit au Hall of Beer ou au Motocultor, merci d'avoir été là, même à plus de 500km.

Et enfin, on garde les meilleurs pour la fin. Que serais je sans les Hipsters ? Ce groupe que j'aime tellement. Maxime et Noémie. Corentin et Sara. Ce groupe a vécu ensemble des soirées au Sur Mesure qui nous ont unies et un mariage incroyable. Merci à vous, pour tout. Pour la connexion qui s'est faite naturellement, pour le soutien, et même les vannes sur mon nom de famille. Atchoum. Peu importe où les vents nous méneront, de la Californie à Sienne en passant par la Bretagne et l'inconnu. Je sais que nous pourrons compter les uns sur les autres.

Pour finir, je tiens à remercier tous ceux que j'ai pu oublier ou que je n'ai eu la place

de citer. Toutes ces rencontres humaines qui m'ont mené ici, tous les échanges que j'ai pu avoir.

Je vous laisse donc à la lecture de ce manuscrit si vous osez ouvrir ces pages. Car d'après Zola : "*Chaque fois que la science avance d'un pas, c'est qu'un imbécile l'a poussée sans le faire exprès.*" Alors j'espère avoir, à mon humble échelle, poussé un peu.

Acknowledgements

I would like to begin by thanking my supervisors and thesis directors, Matthieu Bardon and Emmanuel d'Humières, for giving me the opportunity to conduct this work that has captivated and occupied me for the past three years (and a few additional months). Thank you for your personal support, all your guidance, and the experience you have shared with me. You've guided me along this path of academic research, and I am so grateful to you. I also cannot talk about my supervision without thanking Vladimir Tikhonchuk, an endless source of knowledge throughout the many meetings we've had, and who honored me by serving as a guest member of my committee.

I am particularly honored, Matthieu, to have been your first doctoral student and to have followed you from CESTA to CELIA. I am the first of a lineage that I'm sure is already shaping up, all of whom will have to go through the ritual of karaoke at the ILP forum or having a beer after good news, like an accepted proposal, a finally finished article, or three months of calculations finally unblocked. From the beginning to the end of my PhD, I could count on your availibity, your cheerfulness and your experience to support me.

I'm equally grateful to my family, who has supported me since a young age, encouraging me to explore topics that interested me, discover the world, and ask questions. Mom and Dad, thank you for everything you've imparted to me: the love of words passed down on paper, the love of travel, and the ever-open eye to absorb the beauty of the world around us. I could never have earned this title of Doctor if you hadn't instilled these values and curiosity in me. Thanks, Maureen, the best little sister I could never have imagined. Thank you for your support, your incisive humor (especially aimed at me), and the physiotherapy sessions that helped me recover from the intensity of the doctoral life.

This thesis is also thanks to you, Lionel. Dr. Hirsch, first of the name. You are one of the main reasons that brought me to this moment. I still remember with stars in my eyes my 3rd-grade internship in your laboratory. That initial contact with research, the one that made me say before I even turned 15, "This is what I'll do in the future." I can never thank you enough for that prophetic internship in the university where I spent these years of my thesis.

Thanks also to all of you: Grandpa, Grandma Hélène, Grandma Cécile, Pascale, Alain, Laurence, Gauthier, Mathilde, Clara, Samuel, Maria and Kévin. For your support for over 25 years (some cheeky ones might say almost 30 years), in both good times and the toughest moments. Thanks for being incredible landlords, devoted cat-sitters, escape game partners, and for so many conversations during family meals.

And finally, my thanks to Riley, even though you'll never read these words. Latest addition to the family during this thesis; you've made those nights of questioning the nature of a coil and writing much sweeter. Your purring along my leg is found in the words of this manuscript.

I would also like to express my deep gratitude to my thesis committee, especially Caterina Riconda and Dino Jaroszinsky, for taking on the role of reviewers and providing your feedback. Thanks also to Yves Elskens, Rachel Nuter and Joao Santos for taking the time to read my thesis and for your presence.

Thanks to all my colleagues at LSEM at CEA-CESTA and CELIA for their contributions during these three years of the thesis, whether around the coffee machine, on the

CELIA terrace, in meeting rooms, in the lab, or in the workshop. I want to particularly thank Stéphane Coudert and Romain Liotard, my two office mates, for the discussions, essential breaks, and the warmth they provided.

Special thanks go out to everyone at CELIA and CESTA with whom I collaborated during these three years, whose experience and perspectives illuminated the path of my thesis: Olivier Cessenat, to whom I owe countless hours of computation, and Laurent Merziau, who despite the incredibly tight deadlines I imposed, saved my experiments. Not to forget Jean-Luc Feugeas, Morad Bentayeb, Äli Joundi, and Paul Canel, who allowed me to explore the seemingly counter-intuitive world of neural networks.

I also want to thank all members of the collaboration with PIIM and Thales, without whom this thesis would not have been the same: Yves Elskens, Frédéric André, Damien Minenna, Khalil Aliane, Fabrice Doveil, and Alexandre Poyé.

And most importantly, thank you, Clément. Thank you for being the next in line to carry the torch. This year working alongside you has shown me that you are the right person for the job, and I'm proud to pass on the flame. I feel that, with your equations, the coils will do wonderfully.

Thank you also to my friends, wherever they come from. To all the non-permanent members of SMMS: Juliette, Amandine, Luc, Lucas, Bruno, Damien, Julien. Thanks for the atmosphere at one of the many coffee breaks upon arrival of the shuttle and all the discussions around them.

To the entire CELIA group, and our evenings of drinking beers, enjoying raclettes, or playing dice around a table, thank you for these moments of laughter, dancing at Tencha, and camaraderie. Thanks to Romain, Paul, Diego, Duncan, Edoardo, Clément, Ali, Howel, Corisande, Alana, Alexandre, Morad, Margaux, Thomas, Arnaud, Kristal, Florent, Diluka, Marine, Christos, Philip, Tadeas, Olena, and Guillaume.

Thanks to all my friends outside the laboratories. Especially Florian and Gaëlle, a pair I hold dear, whether at the Hall of Beer or Motocultor, thank you for being there, even more than 500 kilometers away.

And of course, I saved the best for last. What would I be without the Hipsters? This group that I love so much. Maxime and Noémie. Corentin and Sara. This group has lived through evenings at Sur Mesure that have brought us together and an incredible wedding. Thank you all, for everything. For the natural connection, for the support, and even the jokes about my last name. Atchoum. No matter where the winds take us, from California to Sienna, through Brittany and into the unknown, I know we can count on each other.

To conclude, I want to thank all those I may have forgotten or didn't have the space to mention. All these human encounters that brought me here, all the exchanges I've had.

So, I leave you to read this manuscript if you dare to open these pages. Because, as Zola said, "*Each time science advances one step, it's because a fool has pushed it without meaning to.*" So, I hope to have pushed it a little in my own humble way.

Contents

List of Figures

Introduction

A quick history of particle accelerators

The need for particle accelerators has been recognized since the end of the 19$^{\text{th}}$ century to answer the questions raised by nuclear and particle physics. In order to answer these needs, the development of the first accelerators started and led to the first two particle accelerators in the world: the cyclotron of Ernest Lawrence which produced 1.25 MeV protons in 1932 at Berkeley [1] and the electrostatic accelerator of Cockcroft and Walton which produced 400 keV protons in Oxford [2].

Since then, the need for particle beams has generalized to many other fields, such as medicine for the irradiation of cancerous cells or art history as a tool for material analysis. This made particle accelerators a growing field, with more than 30 000 particle accelerators in operation worldwide in the early 2010s. From the small keV electrostatic accelerators to the record breaking TeV Large Hadron Collider at CERN, the technologies have evolved to answer the needs of today's science. However, 'classical' accelerators such as these have some drawbacks: their size and their costs, going up to 27 km of circumference and several billions of euros for the LHC.

One important evolution is the development of laser-plasma accelerators. First theorized by Tajima and Dawson in 1979 [3], they were made possible by the development of chirped pulse amplification (CPA) by Strickland and Mourou [4]. Indeed, the CPA process enabled the development and manufacturing of laser with enough intensity to create very short and intense laser pulses capable to efficiently excite plasma wakefields and create strong electrostatic fields for electrons and/or ions acceleration. These new schemes of acceleration allow very compact accelerators, with interaction zones in the range of the μm to the mm instead of the m to the km.

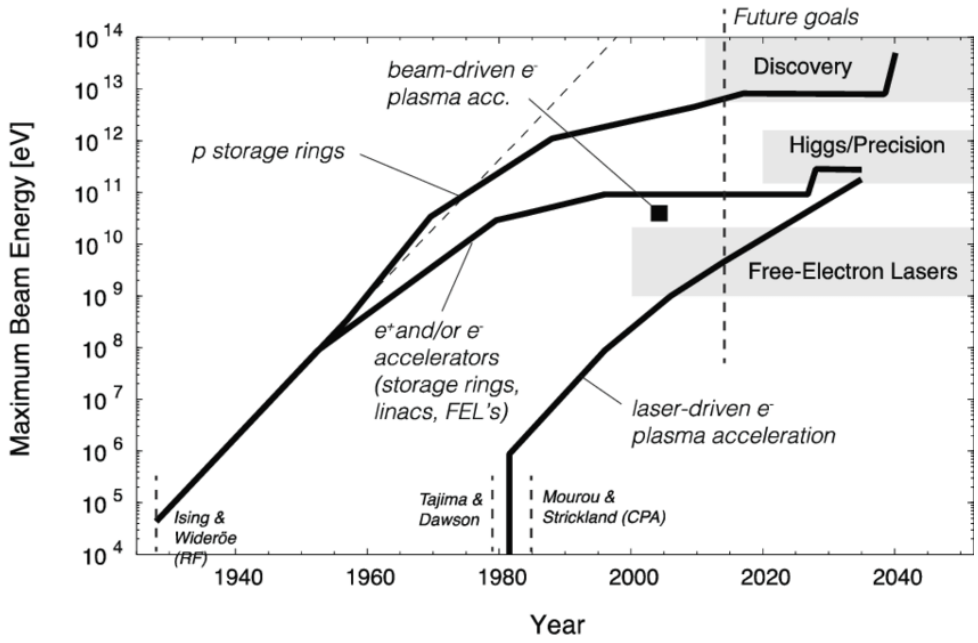

Figure 1 – Livingston curve for accelerators, showing the maximum reach in beam energy for different technologies versus year. Grey bands visualize accelerator applications in science. Data beyond 2014 indicate goals for the various technologies [5].

The evolution of this parallel set of technologies led to new schemes of acceleration whose capacities are still increasing exponentially such as the wakefield acceleration for electrons [6] or the interaction of laser and solid targets for ion acceleration [7]–[9]. Assuming the rate of this exponential growth stays constant, laser plasma accelerators will be competing with classical accelerators before 2040 on several fields of applications (cf. Figure 1).

Laser-driven ion acceleration

My work is performed in the context of laser-driven ion acceleration schemes. Ion acceleration by intense and short laser pulses [7]–[9] has been a growing research field due to the many possible applications of such proton beams: isochoric heating [10], radio-isotope [11] and neutron [12] production, ion-driven fast ignition [13], [14] and plasma radiography [15], [16]. Laser generated proton beams have very interesting properties compared to 'classically' accelerated proton beams: short duration, high current, low emittance, high laminarity and high brightness [8], [17]–[19]. Several laser-driven ion acceleration processes are identified, such as the Target Normal Sheath Acceleration (TNSA) [20], [21], radiation pressure acceleration (RPA) [22], [23] or collisionless shock acceleration [24]. TNSA is of particular interest, as it is the most robust scheme. It is characterized by a large angular divergence ($\sim$40°) [20] and an exponential energy distribution [20] with a cut-off energy depending on the laser intensity and energy [7], [8].

However, the large angular divergence and spectral distribution of TNSA ion beams are limitations for several potential applications, such as isochoric heating for warm dense matter (WDM) studies [10], radio-isotope production for medical applications [11] or neutron production [12] for measurements of nuclear cross sections for processes relevant to astrophysics. In order to improve the quality of TNSA ion beams, several schemes have been designed to focus, post-accelerate and select in energy ions such as the use of an

active plasma lens [25], magnetic self-focusing in a stack of conducting foils [26], proximal target structures [27], target curvature [10], [28]–[31] , target shaping [31], [32], solenoid field [33], [34], ultra-thin foil targets [35], and nano and micro-structured targets [36].

Helical coil targets

To answer the problematic of the experimental limitation of TNSA beams, Kar *et al.* [37] developed a dynamic scheme for the focusing, post-acceleration and bunching of a TNSA proton beam. It consists in attaching a helical coil (HC) normally to the rear side of the target foil.

This scheme uses a simple set-up with a single laser beam. The helix attached to the rear side of the foil acts as an electromagnetic (EM) wave-guide and also as a delay line. The laser interaction generates the proton beam via the TNSA process. Charges are ejected from the target, and as it is connected to the ground through the helix, a discharge current pulse is also self generated. Its propagation along the helix produces an electromagnetic pulse (EMP) that interacts with the proton beam inside the helix. The longitudinal component of the electric field bunches and post-accelerates the proton beam, and the radial component focuses it. The synchronization of the longitudinal pulse propagation speed with the proton one is achieved by adjusting the helix geometric parameters: its radius a and its pitch h.

This mechanism is the only one that enables to bunch, collimate and post-accelerate the proton beam at the same time. Experiments were performed on the ARCTURUS facility [38], with a laser pulse of duration $\tau = 30$ fs and energy $E = 3$ J, producing TNSA beam with a maximum energy of up to 7 MeV. A protonic radiography of the propagation of a current pulse in a conducting wire provided the characterisation of the discharge current as a Gaussian pulse, with an amplitude of the order of a kA and a duration at full-width at half-maximum (FWHM) of the order of 10 ps. This experiment serves as a proof of concept of the post-acceleration and chromatic focusing of TNSA protons with a helical coil (HC) target. However, this campaign showed a low yield of post-accelerated protons at the exit of the target and has to be extended to high laser pulse energy.

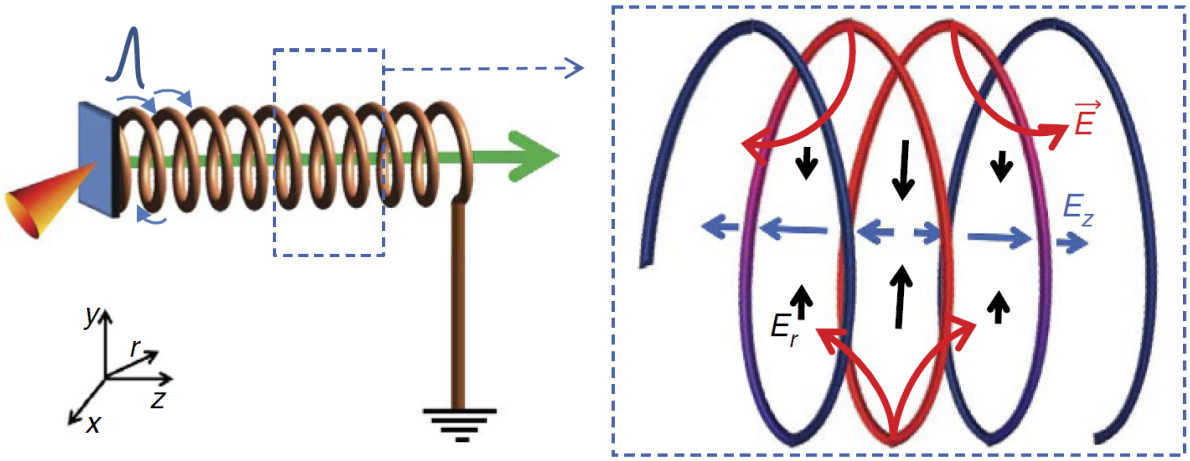

(a) (b)

Figure 2 – Scheme of (a) a helical coil target and (b) the electric fields generated by the propagation of the discharge current inside the helix [37].

Following this work, Bardon *at al.* [39] extended the study of HC targets on a higher energy laser facility: LULI2000 [40], with the PICO2000 laser: a 50 J pulse with a duration of 1 ps. The experimental campaign was supported by a large-scale Particle-In-Cell (PIC) simulation study of the post-acceleration of TNSA protons by HC and of the discharge current dispersion during the propagation through an HC. An agreement between experimental results and PIC simulations in this regime validated the concept of HC targets on higher energy facilities. However, this study also shows a low yield of this post-acceleration scheme and raises the issue of the current dispersion in the helical coil, limiting the efficiency of the proton beam acceleration.

To sum up, it is possible to post-accelerate the proton beam generated by the TNSA process, by injection in a 'classical' accelerator for example, or to focus them, with the use of a cylinder acting as a converging lens after being irradiated by a second laser pulse. But, to this day, only one method allows to both post-accelerate and focus the TNSA beam without the need for a secondary source: helical coil targets. However, this scheme has significant drawbacks: a low yield on the total charge of the beam at the exit of the HC compared to the input TNSA beam, as well as a limited acceleration and bunching efficiency due to the current pulse dispersion in the helix. These issues limit several possible applications.

Research question and layout of the manuscript

The work I performed during these three years of doctoral study was to answer the following research question:

Is it possible to design helical coil targets that produce proton beams with optimal features for specific applications?

The aim of my work was to conduct a numerical and experimental investigation to design new helical target geometries for the post-acceleration, bunching and focusing of TNSA protons that can be adapted for various applications. To succeed in this project, we need to define the main physical processes, to develop an efficient and accurate modelling, and to develop a suitable design method with well identified scaling laws.

The manuscript is organised in four sections, which are the following:

— Chapter 1 introduces the theoretical context behind the post-acceleration with helical coil targets. This chapter presents the notions of laser-plasma acceleration, in particular the TNSA process, as well as the generation of electromagnetic fields by the propagation of a current in a helically-shaped wire.
In Chapter 2, I present the essential tools used during my PhD, both experimental and numerical. The experimental side consists in a presentation of the experimental set-up and an in-depth description of the RCF unfolding of proton energy spectra. The numerical tools presented are the Particle-In-Cell code SOPHIE and the theoretical model DoPPLIGHT developed by our team.
These first two chapters serve as introduction for the next three chapters where is presented my PhD work: experimental analysis, theoretical work and design of new target geometries.

— Chapter 3 is dedicated to the analysis of the PACMAN 2 experimental campaign. It first discusses the sources of shot-to-shot variations in the experimental results

as well as the robustness of our experimental set-up. It then presents the results of the parametric variation on the coil geometry and its impact on the TNSA proton beam. Finally, it identifies the main physical mecanism responsible for the limited proton yield: the proton space charge.

— The third subject is the theoretical and numerical studies of the physical phenomena limiting the helical coil efficiency. In Chapter 4, I consider the space charge of the TNSA proton beam inside the helical coil. First I characterise the shape of the proton beam both in its radial and longitudinal dimension. I then develop the theory of a non-relativistic Gaussian proton beam before implementing this model in the theoretical model DoPPLIGHT.
In Chapter 5, I introduce a new scheme of helical coil targets designed specifically to reduce the dispersion of the discharge current propagating along the helix. I first describe the new scheme and its origin. I then develop the theory behind this new scheme and show the results of a study of the new scheme via PIC simulations and DoPPLIGHT calculations. Finally, I show the first design of these new targets and their impact on the TNSA proton beam.

— The final section of this manuscript is a conclusion answering the question asked in this introduction, discussing the main results presented in the previous chapter and the perspectives for future works on helical targets.

Introduction

Un bref historique des accélérateurs de particules

L'accélération de particules a répondu à un besoin apparu à la fin du 19eme siècle pour répondre aux questions posées par la physique des particules et nucléaire. Pour répondre à ces besoins, le développement des premiers accélérateurs de particules a commencé et conduit aux deux premiers accélérateurs de particules au monde : le cyclotron d'Ernest Lawrence, qui a produit des protons de 1,25 MeV en 1932 à Berkeley [1], et l'accélérateur électrostatique de Cockcroft et Walton, qui a produit des protons de 400 keV à Oxford [2].

Depuis lors, le besoin en faisceaux de particules s'est généralisé à de nombreux autres domaines, tels que la médecine pour l'irradiation des cellules cancéreuses ou l'histoire de l'art pour l'analyse des matériaux. Cela a fait des accélérateurs de particules un domaine en expansion, avec plus de 30 000 accélérateurs de particules en fonctionnement dans le monde au début des années 2010. Des petits accélérateurs électrostatiques accélérant au keV au Large Hadron Collider du CERN allant jusqu'au TeV, les technologies ont évolué pour répondre aux besoins de la science d'aujourd'hui. Cependant, les accélérateurs "classiques" ont certains inconvénients : leur taille et leur coût, allant jusqu'à 27 km de circonférence et plusieurs milliards d'euros pour le LHC.

Une évolution importante est le développement des accélérateurs laser-plasma. D'abord théorisés par Tajima et Dawson en 1979 [3], ils ont été rendus possibles par le développement de l'amplification par dérive temporelle (CPA) par Strickland et Mourou [4]. En effet, le processus CPA a permis le développement et la fabrication de lasers suffisamment intenses pour créer des impulsions laser très courtes et suffisamment intenses pour être capables de générer efficacement des champs de sillage dans un plasma et de créer des champs électrostatiques puissants pour l'accélération des électrons et/ou des ions. Ces nouveaux schémas d'accélération permettent la création d'accélérateurs très compacts, avec des zones d'interaction de l'ordre du μm au mm, au lieu du mètre au kilomètre.

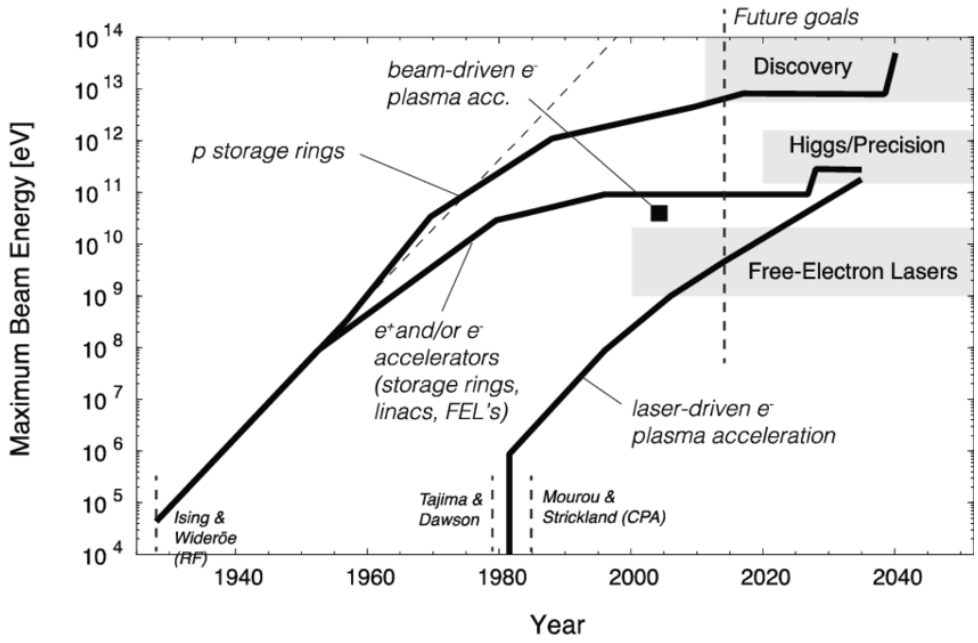

FIGURE 3 – Courbe de Livingston pour les accélérateurs de particules, montrant l'énergie maximale des faisceaux pour différentes technologies par rapport à l'année. Les bandes grises représentent les applications des accélérateurs dans la science. Les données au-delà de 2014 indiquent les objectifs pour les différentes technologies [5].

L'évolution de ce groupe de technologies parallèle a conduit à de nouveaux schémas d'accélération dont les capacités augmentent toujours de manière exponentielle, tels que l'accélération par champ de sillage pour les électrons [6] ou l'interaction entre des lasers et des cibles solides pour l'accélération des ions [7]-[9]. En supposant que le taux de cette croissance exponentielle reste constant, les accélérateurs plasma-laser rivaliseront avec les accélérateurs classiques avant 2040 dans plusieurs domaines d'application (cf. Figure 3).

Accélération d'ions par voie laser

Mon travail s'inscrit dans le contexte de l'accélération d'ions par voie laser. L'accélération d'ions par des impulsions laser intenses et courtes [7]-[9] est un domaine de recherche en pleine croissance en raison des nombreuses applications possibles de ces faisceaux de protons : chauffage isochore [10], production de radio-isotopes [11] et de neutrons [12], allumage rapîde pour la fusion par confinement inertiel [13], [14] et radiographie des plasmas [15], [16]. Les faisceaux de protons générés par laser présentent des propriétés très intéressantes par rapport aux faisceaux de protons "classiquement" accélérés : courte durée, fort courant, faible émittance, grande laminarité et grande brillance [8], [17]-[19]. Plusieurs processus d'accélération d'ions par voie laser sont identifiés, tels que le Target Normal Sheath Acceleration (TNSA) [20], [21], l'accélération par pression de rayonnement (RPA) [22], [23] ou l'accélération par choc sans collision [24]. La TNSA est d'un intérêt particulier, car c'est le schéma le plus robuste. Il se caractérise par une grande divergence angulaire ($\sim$40°) [20] et une distribution d'énergie du faisceau de protons exponentiellement décroissante [20] avec une énergie de coupure dépendant de l'intensité et de l'énergie du laser [7], [8].

Cependant, la grande divergence angulaire et la distribution spectrale des faisceaux d'ions TNSA sont des limitations pour plusieurs applications potentielles, telles que le

chauffage isochore pour les études de la matière dense et chaude (WDM) [10], la production de radio-isotopes à des fins médicales [11] ou la production de neutrons [12] pour les mesures des sections efficaces nucléaires et des processus pertinents pour l'astrophysique. Afin d'améliorer la qualité du faisceau d'ions TNSA, plusieurs schémas ont été conçus pour focaliser, post-accelérer et sélectionner les ions en fonction de leur énergie, tels que l'utilisation d'une lentille plasma active [25], l'auto-focalisation magnétique dans un paquet de feuilles conductrices [26], des structures de cibles proximales [27], la courbure de la cible [10], [28]-[31], la modification de la géometrie de la cible [31], [32], l'ajout d'un champ solénoïdal [33], [34], des cibles ultra-minces [35], et des cibles nano et microstructurées [36].

Cibles hélicoïdales

Pour répondre à la problématique de la limitation expérimentale des faisceaux TNSA, Kar *et al.* [37] ont développé un schéma dynamique pour la focalisation, la post-accélération et le bunching d'un faisceau de protons TNSA. Il consiste à fixer une hélice normalement au verso de la feuille cible.

Ce schéma utilise une configuration simple avec un seul faisceau laser. L'hélice fixée en face arrière de la cible agit comme un guide d'onde électromagnétique (EM) et comme une ligne à retard. L'interaction laser génère le faisceau de protons via le processus TNSA. Des charges sont éjectées de la cible, et comme elle est connectée à la terre par l'intermédiaire de l'hélice, une impulsion de courant de décharge est également auto-générée. Sa propagation le long de l'hélice produit une impulsion électromagnétique (IEM ou EMP) qui interagit avec le faisceau de protons à l'intérieur de l'hélice. La composante longitudinale du champ électrique bunche et post-accélère le faisceau de protons, et la composante radiale le focalise. La synchronisation de la vitesse de propagation de l'impulsion longitudinale avec celle des protons est obtenue en ajustant les paramètres géométriques de l'hélice : son rayon a et son pas h.

Ce mécanisme est le seul qui permet de buncher, collimater et post-accélérer le faisceau de protons en même temps. Des expériences ont été réalisées sur l'installation ARCTURUS [38], avec une impulsion laser d'une durée $\tau = 30$ fs et une énergie $E = 3$ J, produisant un faisceau TNSA avec une énergie maximum pouvant atteindre 7 MeV. Une radiographie protonique de la propagation d'une impulsion de courant dans un fil conducteur a permis la caractérisation du courant de décharge sous forme d'une impulsion gaussienne, avec une amplitude de l'ordre du kA et une durée à mi-hauteur (FWHM) de l'ordre de 10 ps. Cette expérience sert de preuve de concept de la post-accélération et de la focalisation chromatique des protons TNSA avec une cible hélicoïdale (HC). Cependant, cette campagne a montré un faible rendement des protons post-accélérés à la sortie de la cible et doit être étendue à une impulsion laser d'énergie plus élevée.

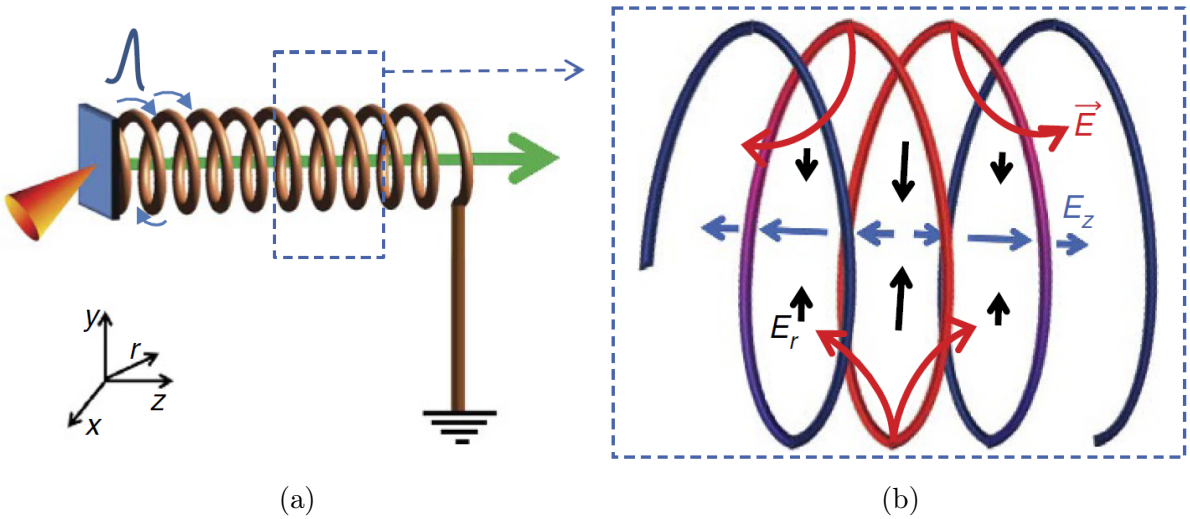

(a) (b)

FIGURE 4 – Schéma (a) d'une cible hélicoïdale et (b) des champs électriques générés par la propagation du courant de décharge le long de l'hélice [37].

Suite à ces travaux, Bardon *et al.* [39] ont étendu l'étude des cibles hélicoïdales sur une installation laser de plus haute énergie : LULI2000 [40], avec le laser PICO2000 : une impulsion de 50 J d'une durée de 1 ps. La campagne expérimentale a été soutenue par une étude de simulation via un code Particle-In-Cell (PIC) à grande échelle de la post-accélération des protons TNSA par cible hélicoïdale et de la dispersion du courant de décharge pendant la propagation à travers une hélice conductrice. Un accord entre les résultats expérimentaux et les simulations PIC dans ce régime a validé le concept des cibles hélicoïdales sur les installations de plus haute énergie. Cependant, cette étude montre également un faible rendement de ce schéma de post-accélération et soulève la question de la dispersion du courant dans l'hélice, limitant l'efficacité de l'accélération du faisceau de protons.

Pour résumer, il est possible de post-accélérer le faisceau de protons généré par le processus TNSA, par exemple en l'injectant dans un accélérateur "classique", ou de le focaliser en utilisant un cylindre agissant comme une lentille convergente après avoir été irradié par une seconde impulsion laser. Cependant, à ce jour, une seule méthode permet à la fois de post-accélérer et de focaliser le faisceau TNSA sans nécessiter de source secondaire : les cibles hélicoïdales. Toutefois, ce schéma présente des inconvénients significatifs : un faible rendement de la charge totale du faisceau à la sortie de l'hélice par rapport au faisceau TNSA d'entrée, ainsi qu'une efficacité limitée en termes d'accélération et de bunching en raison de la dispersion du courant de l'impulsion dans l'hélice. Ces problèmes limitent plusieurs applications potentielles.

Structure du manuscrit

Le travail que j'ai effectué au cours de ces trois années d'études doctorales avait pour objectif de répondre à la question suivante :

> Est-il possible de concevoir des cibles à hélice produisant des faisceaux de protons présentant des caractéristiques optimales pour des applications spécifiques ?

L'objectif de mon travail était de mener une enquête numérique et expérimentale pour concevoir de nouvelles géométries de cibles hélicoïdales pour la post-accélération, le bunching et la focalisation de protons TNSA qui puissent être adaptées à diverses applications. Pour réussir dans ce projet, nous devons définir les principaux processus physiques, développer une modélisation efficace et précise, et mettre au point une méthode de conception adaptée avec des lois d'échelle bien identifiées.

Le manuscrit est organisé en quatre sections, qui sont les suivantes :

— Le chapitre 1 introduit le contexte théorique derrière la post-accélération avec des cibles hélicoïdales. Ce chapitre présente les notions d'accélération d'ions par voie laser, en particulier le processus TNSA, ainsi que la génération de champs électromagnétiques par la propagation d'un courant dans un fil en forme d'hélice.
Dans le chapitre 2, je présente les outils essentiels utilisés au cours de ma thèse, à la fois expérimentaux et numériques. Du côté expérimental, je décris l'installation expérimentale et fournis une description approfondie de la déconvolution des films radiochromiques pour l'analyse des spectres en énergie des protons. Les outils numériques présentés incluent le code Particle-In-Cell SOPHIE et le code réduit DoPPLIGHT développé par notre équipe.

— Le chapitre 3 est dédié à l'analyse de la campagne expérimentale PACMAN 2. Il aborde d'abord les sources des variations tir à tir dans les résultats expérimentaux ainsi que la robustesse de notre dispositif expérimental. Ensuite, il présente les résultats de la variation paramétrique de la géométrie des cibles hélicoïdales et son impact sur le faisceau de protons TNSA. Enfin, il identifie le principal mécanisme physique responsable du faible rendement en protons : la charge d'espace des protons.

— Le troisième sujet concerne les études théoriques et numériques des phénomènes physiques limitant l'efficacité des bobines hélicoïdales. Dans le chapitre 4, je traite de la charge d'espace du faisceau de protons TNSA à l'intérieur de la bobine hélicoïdale. Tout d'abord, je caractérise la forme du faisceau de protons tant dans sa dimension radiale que longitudinale. Ensuite, je développe la théorie d'un faisceau de protons gaussien non relativiste avant d'implémenter ce modèle dans le code réduit DoPPLIGHT.
Dans le chapitre 5, j'introduis un nouveau schéma de cibles hélicoïdales conçu spécifiquement pour réduire la dispersion du courant de décharge se propageant le long de la bobine. Tout d'abord, je décris le nouveau schéma et son origine. Ensuite, je développe la théorie derrière ce nouveau schéma et présente les résultats d'une étude du nouveau schéma via des simulations PIC et des calculs DoPPLIGHT. Enfin, je présente la première conception de ces nouvelles cibles et leur impact sur le faisceau de protons TNSA.

— La dernière section de ce manuscrit est une conclusion qui répond à la question posée dans cette introduction et discute des principaux résultats présentés dans les chapitres précédents et des perspectives pour les futurs travaux sur les cibles hélicoïdales.

Chapter 1

Theoretical context

In this chapter, I present the theoretical context essential to understand the physical phenomena happening inside a helical coil target.

I first introduce the basics of relativistic laser-plasma interaction and then the process of Target Normal Sheath Acceleration which is the proton source used throughout this manuscript.

I also introduce the space charge field of a proton beam and its effect on the particle beam dynamics.

Finally, I describe the physical effect of the propagation of a transient current inside a helix which is the source of the electromagnetic fields used in helical coil targets to post-accelerate and focus the TNSA proton beam.

1.1 Laser-plasma interaction

This section presents the concept of high-power lasers and their interaction with a plasma, necessary to explain the TNSA ion acceleration process.

1.1.1 High-power lasers

The development of high-power lasers was made possible by the invention of the 'Chirped Pulse Amplification' by Strickland and Mourou in 1985 [4]. Before the 1980s, the highest peak intensity achieved was of the order of 10^{15} W.cm^{-2}. The CPA process enabled the development of lasers reaching peak intensities of the order of 10^{23} W.cm^{-2} in the early 2020s [41]. The principle of the CPA is described schematically in Figure 1.1

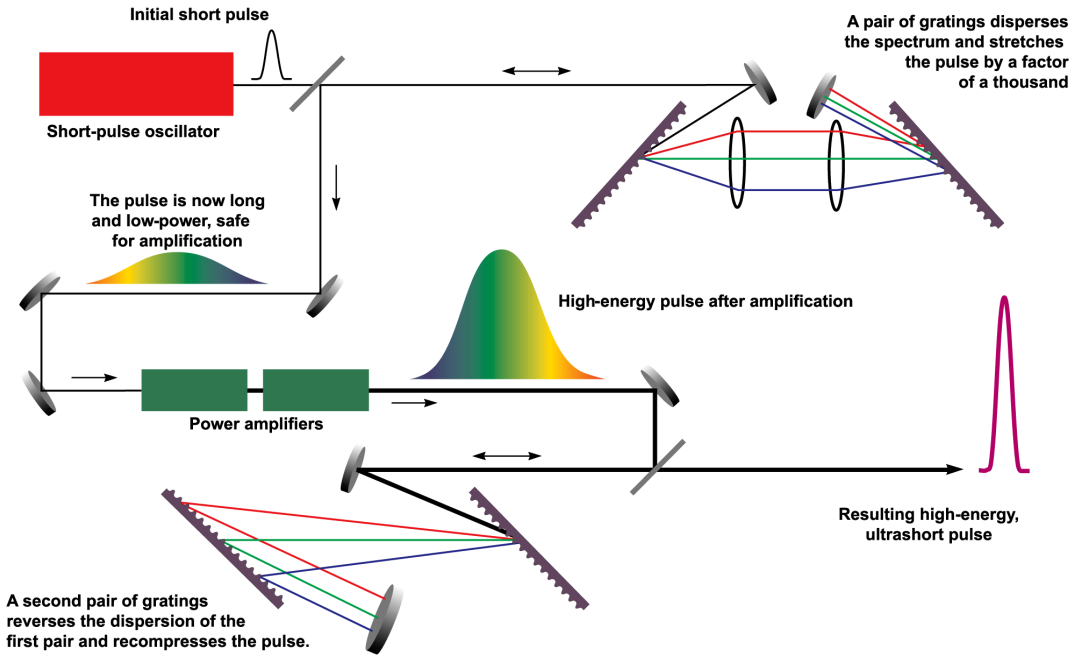

Figure 1.1 – Schematics of the Chirped Pulse Amplification [42].

It can be explained as follows: a short femtosecond laser pulse of low energy is temporally spread through a grating by a factor 1000 to 100 000 before going through the amplification module of the laser line. Once amplified, the laser pulse goes through a grating opposite to the first, recombining the pulse to a femtosecond duration. This enables the amplification of ultra short pulses without damaging the amplificator medium, which was the previous limitation of short pulse amplification.

1.1.2 Relativistic laser-plasma interaction

We describe our laser by a plane wave vector potential propagating along the z-axis and polarised in the plane perpendicular to the z-axis:

$$\mathbf{A} = A_0 \cos(k_L z - \omega_L t)\mathbf{e}_\perp \tag{1.1.1}$$

with $\mathbf{k}_L$ the wave vector of the laser, ω_L its angular frequency and $\mathbf{e}_\perp$ the unit vector of the polarisation direction.

We describe the relativistic motion of an electron in this EM wave by the relativistic equation of motion:

$$\frac{d\mathbf{p}}{dt} = q\left(\frac{\partial \mathbf{A}}{\partial t} + \mathbf{v} \wedge (\nabla \wedge \mathbf{A})\right) \tag{1.1.2}$$

with $\mathbf{p} = m_e \gamma \mathbf{v}$ the electron momentum and $\gamma = \sqrt{1 + \frac{|\mathbf{p}|^2}{m_e^2 c^2}}$ the Lorentz factor of the electron.

In the case of plane wave, we have $\frac{\partial A_y}{\partial x} = \frac{\partial A_x}{\partial y} = 0$ and $\mathbf{A_z} = 0$. We can then substitute for all vector in the perpendicular plane $\xi_\perp \mathbf{e}_\perp = \xi_x \mathbf{e_x} + \xi_y \mathbf{e_y}$, i.e. $\mathbf{e}_\perp \cdot \mathbf{e_z} = 0$, and we get:

$$\begin{cases} \frac{d\mathbf{p}_\perp}{dt} = -q\left(\frac{\partial \mathbf{A}_\perp}{\partial t} + v_z \frac{\partial \mathbf{A}_\perp}{\partial z}\right) \\ \frac{d\mathbf{p}_z}{dt} = q\left(v_\perp \frac{\partial \mathbf{A}_\perp}{\partial z}\right) \end{cases} \tag{1.1.3}$$

From the kinetic energy of the particle $E_c = (\gamma - 1)m_e c^2$ and the relation $\frac{\partial E_c}{\partial \mathbf{p}} = \mathbf{v}$, we obtain, by multiplying (1.1.2) by the speed, the electron energy conservation law:

$$\frac{dE_c}{dt} = e\mathbf{v} \cdot \frac{\partial \mathbf{A}}{\partial t} \tag{1.1.4}$$

Assuming particles at rest at $t = 0$, we can integrate the perpendicular momentum to get the new form of the longitudinal component of the motion equation:

$$\frac{dp_z}{dt} = -\frac{q^2}{2\gamma m}\frac{\partial |\mathbf{A}_\perp|^2}{\partial z} \tag{1.1.5}$$

The previous equation shows that the acceleration in the longitudinal direction is proportional to $A^2 \propto E_L \propto I_L$, with E_L and I_L the energy and intensity of the laser.

From the previous equations, we can calculate a new conservation law:

$$\frac{dE_c}{dt} = \frac{q^2}{2\gamma m}\frac{\partial |\mathbf{A}_\perp|^2}{\partial t} \tag{1.1.6}$$

By summing (1.1.5) and (1.1.6) multiplied by c, we get:

$$\frac{d}{dt}\left((\gamma - 1)mc^2 - cp_z\right) = \frac{q^2}{2\gamma m}\left(\frac{\partial |\mathbf{A}_\perp|^2}{\partial t} + c\frac{\partial |\mathbf{A}_\perp|^2}{\partial z}\right) = \frac{q^2}{2\gamma m} \cdot 0 \tag{1.1.7}$$

As we assume particles at rest at $t = 0$, we have:

$$E_c = cp_z \tag{1.1.8}$$

And so, we obtain:

$$p_z = \frac{p_\perp^2}{2mc} \tag{1.1.9}$$

In conclusion, we have a positive longitudinal component of the particle momentum, meaning the particles are accelerated in the direction of the wave propagation. The angle between the wave propagation and the particle trajectory is given by:

$$\tan(\phi) = \frac{p_\perp}{p_z} = \sqrt{\frac{2}{\gamma - 1}} \tag{1.1.10}$$

For relativistic particles, i.e. $\gamma \gg 1$, the particles move in the direction of the laser propagation, while for non-relativistic particle, i.e. $\gamma \approx 1$, they oscillate in the particle plane.

In the case of electrons, we can combine equations (1.1.1), (1.1.8) and (1.1.9) to obtain the normalised vector potential a_0, using the relation $E_c = \frac{p_\perp^2}{2m} = (\gamma - 1)mc^2$:

$$a_0 = \frac{eA_0}{mc} = \frac{p_\perp}{mc} = \sqrt{2(\gamma_M - 1)} \approx \sqrt{\gamma_M - 1} \tag{1.1.11}$$

with γ_M the maximum Lorentz factor achieved by the electrons.

We consider the interaction between the EM wave and the particles to be relativistic for $a_0 \approx 1$ and higher, as it generates relativistic electrons.

We also defined the intensity of the laser as:

$$I_L = \frac{1}{\mu_0}\langle |\mathbf{E} \wedge \mathbf{B}| \rangle_{2\pi/\omega_L} = \frac{1}{\mu_0 c}\frac{(A_0\omega_L)^2}{2} \tag{1.1.12}$$

From the previous equations, we obtain that the intensity regime necessary for relativistic interaction with electrons is $I_L > 10^{18}$ W.cm^{-2} with $\lambda_L \approx 1$ μm.

Intermediary steps of this calculations can be found in the works of J. Bonvalet [43], S. Carrier-Vallières [44] and V. Ospina-Bohorquez [45].

1.1.3 Plasma generation

For our experiments, our laser is focused on a target initially in a solid state. The interaction between the laser and the target ionizes the atoms composing the latter, creating a plasma. Two processes co-exist : the first one is the multiphotonic ionisation [46], where an electron absorbs several photons at once. This process happens only for high photon flux, i.e. high intensity laser. The second phenomenon is the tunnel ionization [47] in which the laser fields are strong enough to modify the electromagnetic fields seen by the atomic electrons. In this case, the potential barrier lowers under the action of the laser fields and the electrons can cross it by tunnel effect. This process is also called "Over the Barrier Ionization" when the barrier is lowered under the electron potential energy [48]. All of these processes are represented in Figure 1.2:

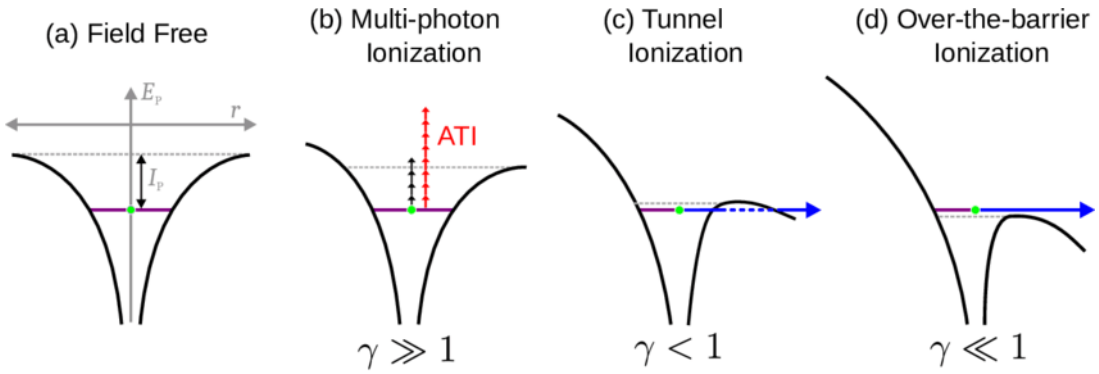

Figure 1.2 – Schematics of the different ionization processes [49], with $\gamma = \gamma_K$ the Keldysh parameter.

Tunnel ionization is governed by the Keldysh parameter γ_K [48], representing the time the electron needs to cross the potential barrier of length l_{tunnel} (dashed line on the tunnel ionization scheme in Figure 1.2) on the duration of the barrier lowering. Indeed, as the laser oscillates, so does the lowering of the potential barrier.

To cross the barrier, the electron must achieve an energy E_e in the laser field,

$$E_e = eE_{laser}l_{tunnel} = \frac{1}{2}m_e\langle v_e\rangle^2. \tag{1.1.13}$$

And we get the tunnel frequency,

$$\nu_{tunnel} = \frac{\langle v_e\rangle}{l_{tunnel}} = \frac{\sqrt{2}eE_{laser}}{\sqrt{m_eE_e}}. \tag{1.1.14}$$

We note the laser frequency as ω_L and we define the Keldysh parameter as,

$$\gamma_K = \frac{2\omega_L}{\nu_{tunnel}} = \frac{\omega_L\sqrt{2m_eE_e}}{eE_{laser}}. \tag{1.1.15}$$

If $\gamma_K \gg 1$, the ionization is multiphotonic as the laser frequency is too high and the laser amplitude is too low for the electron to cross the potential barrier as it does not have

the time or the energy. If $\gamma_K \ll 1$, the ionization is mainly due to the tunnel ionization process.

γ_K is the ratio between the binding energy of the electron over the ponderomotive energy given by the laser to the electron. When $\gamma_K \ll 1$, the binding energy cannot keep the electron around the nucleus anymore. With this vision, we can rewrite,

$$\gamma_K = \sqrt{\frac{E_e}{2U_p}} = \sqrt{\frac{E_e}{2}\frac{4m_e\omega_L^2}{e^2E_{laser}^2}}. \tag{1.1.16}$$

In order to work with this parameter, we need to know the binding energy of the atoms in the target. In the case of a hydrogen atom, we have $E_e = 13.6$ MeV. With a laser intensity $I_L = 10^{20}$ W.cm^{-2}, we get a Keldysh parameter $\gamma_K \approx 0.001$, sufficient to ionize our hydrogen atom by tunnel ionization.

To generalise to other atoms, the atomic potential barrier of an atom can be expressed as $V_{\text{atom}}(r) = -\frac{Ze}{4\pi\epsilon_0 r}$ and the laser potential as $V_{\text{laser}} = -E_{\text{laser}}r$. The sum of these potentials is maximal for $r_{\max} = \sqrt{\frac{Ze}{4\pi\epsilon_0 E_{\text{laser}}}}$. The electron needs an energy $E_e = eV(r_{\max})$ to get out of the potential well. We need the laser energy to be, for $r = r_{max}$, greater than

$$E_{\text{laser}} = \frac{E_e^2\pi\epsilon_0}{Ze^3}. \tag{1.1.17}$$

Which means, we ionise a target of hydrogen when $I_L > 1.4 \times 10^{14}$ W.cm^{-2}. We can justify the complete ionization of our solid target during the laser plasma interaction as our laser intensity is superior to 10^{18} W.cm^{-2} in the case of an ultra-thin target. For thicker targets, we have to take into account collision ionization generated by the electrons crossing the solid target. Hence the process of acceleration of electrons and ions described in the next section.

1.2 Target Normal Sheath Acceleration

The interaction of ultra high intensity (UHI) laser pulses with a plasma explained in the previous section enables to accelerate ions inside the plasma to energies reaching tens of MeV. These acceleration processes are order of magnitudes more intense than in 'classical accelerators', with electric fields a few TV/m. In this section, I present one of these ion acceleration processes, called Target Normal Sheath Acceleration (TNSA), as it is the proton source for all the beams studied in this manuscript. Other acceleration schemes could be used with helical coil targets as long as they produce an ion beam and a discharge current, but my PhD only studied helical coil targets in conjunction with TNSA beams.

The first observations of protons reaching a few MeV after the irradiation of a thin solid target by an intense laser pulse were made in 2000 [20], [50]. This led to the first theories of TNSA in the following years [21], [51].

The TNSA process is schematically shown in Figure 1.3 and can be described by the following steps:

— A UHI laser pulse ($I > 10^{18}$ W.cm^2) hits the front side of our solid target. The pre-pulse creates a pre-plasma, influencing the absorption of the main pulse by the target. This creates a hot electron population through several process explained in the next section.

— The hot electron population, created in the previous step, crosses the target at a speed close to c and reaches the back side of the target. The most energetic hot electrons escape the target through the back side, charging the target positively. The fields created by the charging of the target trap the rest of the hot electrons population [52]. The trapped electrons create a charge separation field, which takes the form of an electrostatic field of the order of the TV/m at the back side of the target.

— The layer of contaminants situated at the back side of the target [53] is ionised, generating many different ions, including protons that have the highest q/m ratio. These contaminants come from the oil and water vapors present inside the experimental chamber [54], [55]. Under the influence of the sheath field generated during the previous step, the ions are accelerated normally to the target back side. With the electron cloud at the back side (and also at the front side), the ions expand and are accelerated until the hot electrons lose their energy in this expansion process and cannot sustain the charge separation anymore.

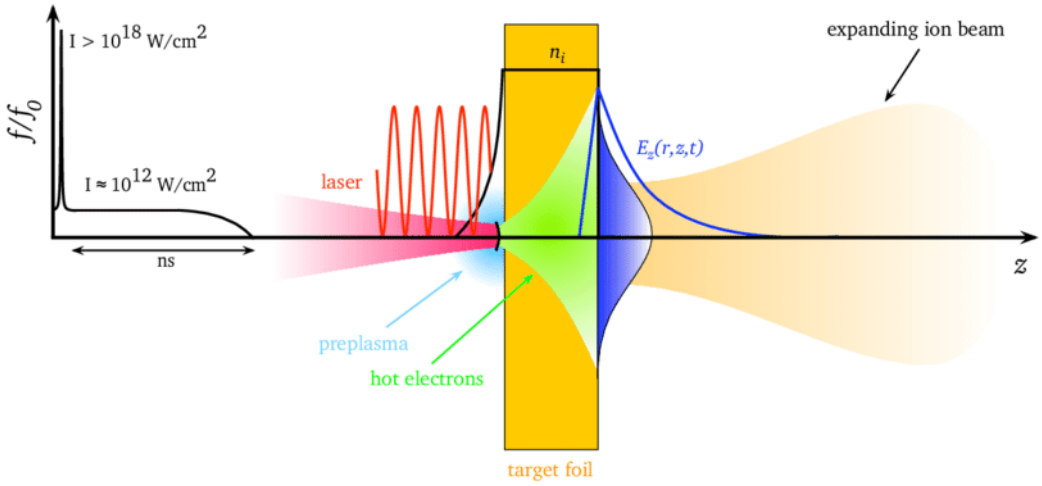

Figure 1.3 – Schematics of the Target Normal Sheath Acceleration [56].

The TNSA process happens on a timescale of a few ps and over a length of the order a few μm.

1.2.1 Hot electrons dynamics

The heating of the electrons by the laser pulse during TNSA comes from different sources: Brunel heating (or vacuum heating) [57], anomalous skin effect [58], [59], resonance heating [60], [61], sheath inverse bremsstrahlung absorption [62], stochastic heating by counter propagating EM waves [63]–[65] and relativistic $\mathbf{J} \wedge \mathbf{B}$ heating [66], [67]. For laser pulses with intensities higher than 10^{18} W.cm^2, this last source is the predominant one.

$\mathbf{J} \wedge \mathbf{B}$ heating occurs when the plasma density is higher than the critical density. In this case, as the laser cannot penetrate the target further than the skin depth, the interaction between the laser and the plasma only happens at the surface.

This acceleration regime only happens when the magnetic component of the Lorentz force $\mathbf{v} \wedge \mathbf{B}$ is large enough, i.e. for relativistic laser intensities. The process behind

$\mathbf{J} \wedge \mathbf{B}$ heating is the following: first the electron is accelerated by the electric component of the laser field transversally. At the same time, the electron is under the effect of the magnetic component of the laser field, driving a longitudinal motion. If the interaction was happening deeper than on the surface, the electrons would oscillate back and forth longitudinally. As the plasma is denser than the critical density, the laser is stopped at the skin depth and the electrons are not slowed down longitudinally by the magnetic component of the Lorentz force. The electrons are injected in the target with the kinetic energy they gained during the acceleration phase.

Electrons accelerated by this process develop a thermal energy distribution [68] and an angular opening of several tens of degrees [69]. The propagation of the electrons through the target creates an intense electron current [70]. The electrostatic field generated by the displacement of charge slows down the electrons injected inside the target. The electrons with the highest energy, even though slowed by the induced electrostatic field, can propagate through the target and exit through the backside if the target is thin enough (i.e. a few μm of thickness or less).

The energy distribution of the electrons accelerated by $\mathbf{J} \wedge \mathbf{B}$ heating is exponentially decreasing, with an effective temperature given by [70]

$$T_e^{\mathbf{v}\wedge\mathbf{B}} = \left(\sqrt{1 + a_0^2/2} - 1\right) m_e c^2. \tag{1.2.1}$$

This means a temperature of a few MeV to a few tens of MeV depending on the laser intensity.

1.2.2 Ion acceleration

Now that we know how the hot electrons are accelerated the hot electrons during the TNSA process, I introduce the ion acceleration mechanism. This mechanism has been explained by Wilks *et al.* [71] and Mora [72] by fluids model describing the expansion of a hot plasma in vacuum. This model describes the expanding plasma as quasi-neutral for an expansion length x_{lim} behind the plasma. The ions in the beam reach their maximal energy E_{max} at x_{lim}. This energy is expressed by Fuchs *et al.* [9] as:

$$E_{\max} = 2T_{\text{hot}} \left(\ln\left(t_p + \sqrt{t_p^2 + 1}\right)\right)^2 \tag{1.2.2}$$

with $t_p = \omega_{\text{pi}}\tau_{\text{acc}}/\sqrt{2\exp(1)}$ is the normalised acceleration duration, $\omega_{\text{pi}} = \sqrt{\frac{Z_{\text{i}}e^2 n_{\text{e0}}}{m_{\text{i}}\epsilon_0}}$ the ionic plasma frequency, Z_{i} the ion charge, m_{i} their mass, n_{e0} the hot electron density and T_{hot} their temperature.

In the same article, Fuchs *et al.* [9] experimentally determined acceleration duration t_{acc} as $t_{\text{acc}} = 1.3\tau_{\text{laser}}$, with τ_{laser} the duration of the laser pulse. Wilks *et al.* [67] rewrite the hot electron temperature given in equation (1.2.1) as

$$T_{\text{hot}} = m_e c^2 \left(\sqrt{1 + \frac{I\lambda_{\mu m}^2}{1.37 \times 10^{18}}} - 1\right). \tag{1.2.3}$$

Now that we have everything to express the maximum energy of the ion population, we need to determine the shape of the ion energy spectrum. We can estimate the number of hot electrons accelerated by

$$N_e = \frac{f E_{\text{laser}}}{T_{\text{hot}}} \tag{1.2.4}$$

where E_{laser} is the incident laser energy and f the absorption fraction of the laser energy which can be written as $f = 1.2 \times 10^{-15} I_{\text{W.cm}^2}^{0.74}$ [9]. In the regime of TNSA, f is usually between 10 and 20%.

The hot electrons interact with the ions in a volume of interaction $V = c\tau_{\text{laser}} S_{\text{sheath}}$ where c is the speed of light and S_{sheath} the surface of the electron sheath on the backside of the target. We can express S_{sheath} as a function of the laser focal spot radius r_0, the target thickness d and the electron beam angular divergence θ:

$$S_{\text{sheath}} = \pi(r_0 + d\tan(\theta))^2 \tag{1.2.5}$$

That gives us the electronic density n_{e0} and Mora's model [72] enables us to calculate the shape of the ion spectrum $\frac{dN}{dE}$ which can be expressed, in number of ions per MeV, as:

$$\frac{dN}{dE} = \left(\frac{n_{\text{e0}} c_s t_{\text{acc}} S_{\text{sheath}}}{\sqrt{2ET_{\text{hot}}}}\right) \exp\left(-\sqrt{\frac{2E}{T_{\text{hot}}}}\right) \tag{1.2.6}$$

with $c_s = \sqrt{\frac{Z_{\text{i}} k_b T_{\text{hot}}}{m_{\text{i}}}}$ the ionic acoustic speed of the expanding plasma.

These theoretical results are in agreement with observed experimental results of the back side proton beam. The proton spectrum, as the hot electron spectrum, is Maxwellian, with a cut-off energy of a few MeV to tens of MeV depending on the laser energy, with a number of low energy protons orders of magnitude higher than the high energy ones [9], [17], [20], [21].

1.2.3 Target composition

While the theoretical approach of the TNSA process does not take into account the target composition, due to the fact that the accelerated protons come from the contaminants layer on the back side of the target, studies have shown the impact of the target composition on the proton beam.

Indeed, high Z targets have a higher number of electrons and a better absorption ratio of the laser energy, leading to more energetic hot electrons. On the other hand, low Z targets with high H compositions, such as CH targets, have a greater number of available protons to accelerate [20], [73]. This is why some double layer target, with a front face made of a high Z layer and a back side of CH have been tested, to optimise both the hot electrons energy and the number of accelerated protons [74].

1.2.4 Beam characteristics

The proton beam issued from the TNSA process has several characteristics that define it:

— The charge inside the beam depends on the laser facility. Low energy facilities give proton beams of a few nC [75] and can reach a few μC on high energy facilities [76].

— The proton cut-off energy scales with the laser energy following the relation $E_{cut-off} \propto E_{las}^{3/2}$ [77]

— The protons angular opening depends on their energy. The highest energy protons in the beam have a half-opening angle of about 5° while the lowest energy ones have an half-opening of about 20-25° [78]. The range of opening angle for low and high energy is the same on every laser facility [79].

The TNSA proton beam has interesting properties, but its Maxwellian spectrum and its large angular opening are limiting for numerous applications. The work I performed during this PhD aimed to optimise the features of this TNSA proton beam to make it more suitable for different applications.

1.3 Space charge of a charged particle beam

To perform the works presented in Chapter 4, one must understand the principle of the space charge of a charged particle beam.

Let us consider the case of two particles of same charge q, located at a distance r of each other. At rest, these particles are under the influence of only the Coulomb force applied on them by the other particle:

$$\mathbf{F_{qq}^{E}} = \frac{q^2 \mathbf{r}}{4\pi\epsilon_0 r^3} \tag{1.3.1}$$

This repulsive force is represented in Figure 1.4:

Figure 1.4 – Schematics of the Coulomb interaction between two particles of same charge q.

Suppose that these two particles are moving along the same axis at the velocity $v = \beta c$. Every charged particle motion creates a current $I = qv$ and this current induces a magnetic field $\mathbf{B}$ which applies on the particle the following force

$$\mathbf{F_{qq}^{M}} = q\mathbf{v} \wedge \mathbf{B}. \tag{1.3.2}$$

This force is attractive and represented in Figure 1.5:

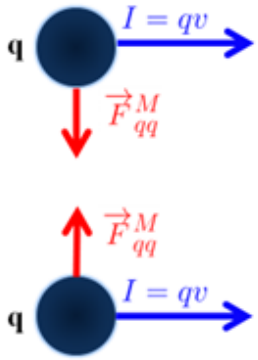

Figure 1.5 – Schematics of the magnetic interaction between two particles of same charge q moving at the speed $\mathbf{v}$.

Suppose a beam of identical particles, of charge q, moving along the same axis at the speed $\mathbf{v}$. Each particle is subject to the influence of the Coulomb field generated by every single other particle of the beam, which creates a repulsive force. On the other hand, as the particles all move in the same direction, they produce an electric current inducing a magnetic field $\mathbf{B}$ and an attractive magnetic force. The space charge force is the sum of these two opposite forces, i.e. the Lorentz force generated by the beam itself.

The question is: which of the electric and magnetic force is predominating? To answer this question, we consider a continuous beam, with a cylindrical symmetry, moving along the axis z at a constant speed $v = \beta_z c$. For a density constant along z, the charge density of the particle beam can be written in the form $\rho(x, y, z) = \rho(r)$ with $r = \sqrt{x^2 + y^2}$.

The Maxwell equation $\nabla \cdot \mathbf{E} = \frac{\rho}{\epsilon_0}$ enables us to write the electric field as

$$\mathbf{E}(r) = \frac{\hat{\mathbf{r}}}{\epsilon_0 r} \int_0^r \rho(u) u du \tag{1.3.3}$$

with $\hat{\mathbf{r}}$ the unit vector in the radial direction.

The second Maxwell equation $\nabla \wedge \mathbf{B} = \mu_0 \mathbf{J}$ provides the magnetic field as

$$\mathbf{B}(r) = \hat{\theta} \frac{\mu_0 \beta_z c}{r} \int_0^r \rho(u) u du = \hat{\theta} \frac{\beta_z}{c} E(r) \tag{1.3.4}$$

with $\hat{\theta}$ the unit vector in the azimuthal direction.

The Lorentz Force $\mathbf{F}$ applied on every particle of the beam reads

$$\mathbf{F} = q(\mathbf{E} + \mathbf{v} \wedge \mathbf{B}) \tag{1.3.5}$$

which can be expressed, using the previously calculated expressions of $\mathbf{E}$ and $\mathbf{B}$

$$\mathbf{F} = q\mathbf{E}(1 - \beta_z^2). \tag{1.3.6}$$

From this formula we conclude that the space charge force of a particle beam is a combination of a strong electric defocusing force compensated by a focusing magnetic force. This compensation is proportional to $1 - \beta^2$, meaning a relativistic beam is not strongly affected by its space charge while a non-relativistic beam diverges under the effect of its space charge.

1.4 Physics of transient current in a helix

The electromagnetic fields used to post-accelerate, focus and bunch a proton beam inside the helical coil are generated from the propagation of the discharge current inside a helix. This set-up is very close to a travelling wave tube (TWT), an RF structure used for signal amplification. A model, called the sheath helix, was proposed by J. R. Pierce [80]. In this one, the helix is approximated by an infinitely thin cylinder with an anisotropic conductivity which is non-zero only in the helical direction. The equations of this model were then developed into a circuit approach by Kino and Paik [81]. This model is set in the Fourier domain, under the assumption that the pulse wavelength along the longitudinal z-axis is larger than the pitch length of the helix.

In this section, we approximatie a helix of radius a and pitch h by an infinitesimally thin cylinder of radius a anisotropically conducting only in the direction Ψ, with Ψ defined as $\Psi = \arctan(h/2\pi a)$, as shown in Figure 1.6

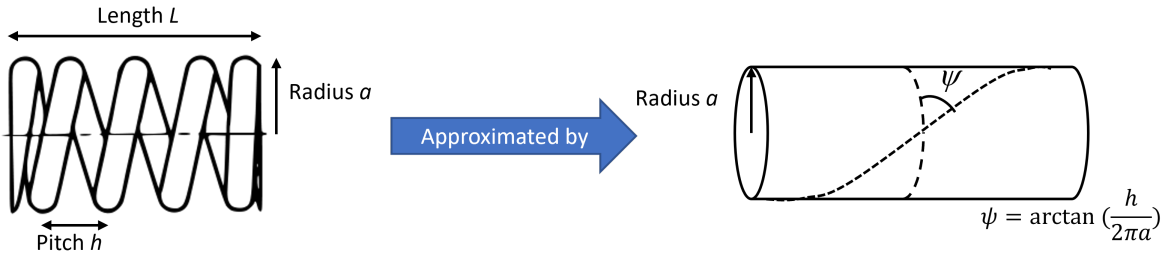

Figure 1.6 – Approximation of a helix of radius a and pitch h in the sheeth helix model.

All the calculations in this section are made in a 2D axi-symmetric coordinate system (r, z, t).

1.4.1 Propagation of a transient current in a helix

Let's first consider the continuity equation of a current propagating along the z-axis:

$$\frac{\partial i(\omega, z)}{\partial z} = -\frac{\partial q}{\partial t} + 2i_0(\omega)\delta'(z), \tag{1.4.1}$$

along with the propagation equation for the charge in a transmission line without dissipation

$$-\frac{1}{C}\frac{\partial q}{\partial z} = L\frac{\partial i(\omega, z)}{\partial t}, \tag{1.4.2}$$

where C is the capacitance of the transmission line and L its inductance.

By differentiating the continuity equation along z and inserting it into the propagation equation, and by taking $k^2(\omega, z) = LC\omega^2$ the wave number squared, we get

$$\frac{\partial^2 i(\omega, z)}{\partial z^2} + k^2(\omega, z)i(\omega, z) = 2i_0(\omega)\delta'(z) \tag{1.4.3}$$

For HC with constant diameter and pitch, one can consider a current of the form $i(\omega, z) = A(\omega, z)e^{j\Psi(\omega)}$. Inserting it into the previous equation, we obtain, by taking the real part of the current,

$$i(\omega, z) = \frac{i_0(\omega)}{2} \cos(k(\omega)z) \tag{1.4.4}$$

By taking into account a phase Ψ dependence on z, we can take into account a coil with a varying pitch or diameter. These calculations are the subject of the PhD work of Clément Lacoste [82].

1.4.2 Propagation of an electromagnetic pulse (EMP) in a helix

As previously shown, the calculation methodology behind this section comes from the sheath helix model presented by Pierce [80]. To obtain the electromagnetic fields generated by the propagation of a current inside a helix, we first need to express the scalar and vector potentials ϕ and $\mathbf{A}$.

The integral formula of the Poisson equation applied to the current gives, after a Fourier transform in phase space (ω, k),

$$\phi(R, \omega, k) = \frac{q(\omega, k)}{2\pi\epsilon_0} I_0(\alpha R) K_0(\alpha a)$$

with $\alpha^2 = k^2 - \left(\frac{\omega}{c}\right)^2$, I_0 and K_0 the modified Bessel function of first and second kind respectively.

Using the continuity equation, we have $\omega q(\omega, k) = k i(\omega, k)$ and finally

$$\phi(R, \omega, k) = \frac{i(\omega, k)}{2\pi\epsilon_0} \frac{k}{\omega} I_0(\alpha R) K_0(\alpha a). \tag{1.4.5}$$

The retarded vector potential calculation gives, with the same methodology,

$$\begin{cases} A_\theta(R, \omega, k) = \frac{\mu_0 \cos(\Psi)}{2\pi} i(\omega, k) I_1(\alpha R) K_1(\alpha a) \\ A_z(R, \omega, k) = \frac{\mu_0 \sin(\Psi)}{2\pi} i(\omega, k) I_1(\alpha R) K_1(\alpha a) \end{cases} \tag{1.4.6}$$

with $\Psi = \arctan(h/2\pi a)$ the helix phase and h the helix pitch.

And we finally obtain the following electromagnetic fields:

$$\begin{cases} E_r = \frac{\partial \phi}{\partial r} \\ E_\theta = j\omega A_\theta \\ E_z = \frac{\partial \phi}{\partial z} - j\omega A_z \end{cases} \tag{1.4.7}$$

$$\begin{cases} B_r = \frac{1}{r} \frac{\partial A_z}{\partial \theta} - \frac{\partial A_\theta}{\partial z} \\ B_\theta = -\frac{\partial A_z}{\partial r} \\ B_z = \frac{1}{r} \frac{\partial r A_\theta}{\partial r} \end{cases} \tag{1.4.8}$$

We can express the fields as,

$$\begin{cases} E_r = \frac{jk}{\alpha} \left(B_3 I_1(\alpha r) - B4 K_1(\alpha r)\right) \\ E_\theta = \frac{j\omega\mu_0}{\alpha} \left(-B_1 I_1(\alpha r) + B_2 K_1(\alpha r)\right) \\ E_z = B_3 I_0(\alpha r) + B_4 K_0(\alpha r) \end{cases} \tag{1.4.9}$$

$$\begin{cases} H_r = \frac{jk}{\alpha} \left(B_1 I_1(\alpha r) - B_2 K_1(\alpha r)\right) \\ H_\theta = \frac{j\omega\epsilon_0}{\alpha} \left(B_3 I_1(\alpha r) - B_4 K_1(\alpha r)\right) \\ H_z = B_1 I_0(\alpha r) + B_2 K_0(\alpha r) \end{cases} \tag{1.4.10}$$

For the rest of the calculation, we will use the notation X^- for the value of a variable X inside the helix and X^+ for the value of a variable X outside the helix.

In $r = +\infty$, we have $E_z = 0$ and $B_z = 0$, which gives us the conditions on the variables B_1 and B_3,

$$\begin{cases} B_1^+ = 0 \\ B_3^+ = 0 \end{cases} \tag{1.4.11}$$

In the same way, the electromagnetic fields cannot be infinite in $r = 0$, so we get conditions on the variables B_2 and B_4:

$$\begin{cases} B_2^- = 0 \\ B_4^- = 0 \end{cases} \tag{1.4.12}$$

We can now take $B_1 = B_1^-$, $B_2 = B_1^+$, $B_3 = B_3^-$ and $B_4 = B_4^+$. To get expressions of the constants B_1 to B_4, we have to take into account the boundary conditions which must be satisfied at the radius $r = a$. They are the following:

— The tangential electric field must be perpendicular to the helix direction:

$$\begin{cases} E_z^- \sin(\Psi) + E_\theta^- \cos(\Psi) = 0 \\ E_z^+ \sin(\Psi) + E_\theta^+ \cos(\Psi) = 0 \end{cases} \tag{1.4.13}$$

— The tangential electric field must be continuous:

$$\begin{cases} E_z^+ = E_z^- \\ E_\theta^+ = E_\theta^- \end{cases} \tag{1.4.14}$$

— The tangential magnetic field parallel to the helix direction must be continuous since there can be no current in the surface perpendicular to this direction:

$$H_z^- \sin(\Psi) + H_\theta^- \cos(\Psi) = H_z^+ \sin(\Psi) + H_\theta^+ \cos(\Psi) \tag{1.4.15}$$

These conditions can be rewritten as the system of equations

$$\begin{cases} B_3 I_0(\alpha a) \tan(\Psi) - B_1 \frac{j\omega\mu_0}{\alpha} I_1(\alpha a) = 0 \\ B_4 K_0(\alpha a) \tan(\Psi) + B_2 \frac{j\omega\mu_0}{\alpha} K_1(\alpha a) = 0 \\ B_3 I_0(\alpha a) = B_4 K_0(\alpha a) \\ -B_1 I_1(\alpha a) = B_2 K_1(\alpha a) \\ B_1 I_0(\alpha a) \tan(\Psi) + B_3 \frac{j\omega\epsilon_0}{\alpha} I_1(\alpha a) = B_2 K_0(\alpha a) \tan(\Psi) - B_4 \frac{j\omega\epsilon_0}{\alpha} K_1(\alpha a) \end{cases} \tag{1.4.16}$$

This system can be simplified to

$$\begin{cases} B_3 = B_1 \frac{j\omega\mu_0}{\alpha} \frac{I_1(\alpha a)}{I_0(\alpha a)} \cot(\Psi) \\ B_4 = -B_2 \frac{j\omega\mu_0}{\alpha} \frac{K_1(\alpha a)}{K_0(\alpha a)} \cot(\Psi) \\ B_4 = B_3 \frac{I_0(\alpha a)}{K_0(\alpha a)} \\ B_2 = -B_1 \frac{I_1(\alpha a)}{K_1(\alpha a)} \\ B_1 \left[I_0(\alpha a) - \frac{\omega^2}{\alpha^2 c^2} \frac{I_1^2(\alpha a)}{I_0(\alpha a)} \cot^2(\Psi) \right] = -B_1 \frac{I_1(\alpha a)}{K_1(\alpha a)} \left[K_0(\alpha a) - \frac{\omega^2}{\alpha^2 c^2} \frac{K_1^2(\alpha a)}{K_0(\alpha a)} \cot^2(\Psi) \right] \end{cases} \tag{1.4.17}$$

By simplifying and reworking the last equation, we get

$$
\begin{aligned}
&I_0(\alpha a) - \frac{\omega^2}{\alpha^2 c^2}\frac{I_1^2(\alpha a)}{I_0(\alpha a)}\cot^2(\Psi) = \frac{-I_1(\alpha a)K_0(\alpha a)}{K_1(\alpha a)} + \frac{\omega^2}{\alpha^2 c^2}\frac{I_1(\alpha a)K_1(\alpha a)}{K_0(\alpha a)}\cot^2(\Psi) \\
\Rightarrow &\alpha^2\left[I_0(\alpha a) + \frac{I_1(\alpha a)K_0(\alpha a)}{K_1(\alpha a)}\right] = \frac{\omega^2}{c^2}\cot^2(\Psi)\left[\frac{I_1^2(\alpha a)}{I_0(\alpha a)} + \frac{I_1(\alpha a)K_1(\alpha a)}{K_0(\alpha a)}\right] \\
\Rightarrow &\alpha^2\frac{I_0(\alpha a)K_0(\alpha a)}{I_1(\alpha a)K_1(\alpha a)} = \frac{\omega^2}{c^2}\cot^2(\Psi)
\end{aligned}
$$

We get the dispersion relation of the helix that we can rewrite as

$$
\omega = \frac{kc}{\sqrt{1 + \cot^2(\Psi)\frac{I_1(\alpha a)K_1(\alpha a)}{I_0(\alpha a)K_0(\alpha a)}}}. \tag{1.4.18}
$$

The HC characteristic velocity is defined as $V_{HC} = c/\sqrt{1 + (2\pi a/h)^2}$. We plot the dispersion relation and the phase velocity $v_\phi(\omega) = \omega/k(\omega)$ for a helix characterised by $a = 0.5$ mm and $h = 0.35$ mm:

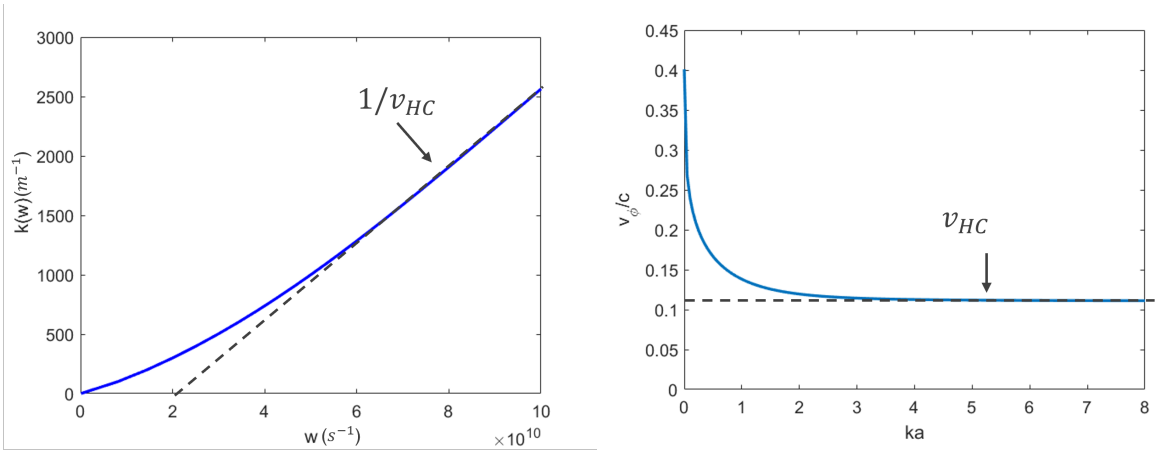

(a)

Figure 1.7 – (a) Dispersion relation as a function of the frequency ω in blue. In black and dashed is the inverse of the characteristic velocity of the helical coil. (b) Phase velocity as a function of ka in blue. In black and dashed is the characteristic velocity of the helical coil. All plots are made for a helix characterised by $a = 0.5$ mm and $h = 0.35$ mm.

We observe in Figure 1.7 that the helix is a dispersive medium, especially at low frequencies, where the phase velocity is larger than the geometrical velocity of a current propagating through the helix.

By coming back to the system solving the B_i constants, we get

$$
\begin{cases}
B_1 = B_3\frac{\alpha}{j\omega\mu_0\cot(\Psi)}\frac{I_0(\alpha a)}{I_1(\alpha a)} \\
B_2 = -B_3\frac{\alpha}{j\omega\mu_0\cot(\Psi)}\frac{I_0(\alpha a)}{K_1(\alpha a)} \\
B_4 = B_3\frac{I_0(\alpha a)}{K_0(\alpha a)}
\end{cases} \tag{1.4.19}
$$

We give the full expressions of the fields inside the helix

$$\begin{cases} E_r = jB_3 \frac{k}{\alpha} I_1(\alpha r) \\ E_\theta = -B_3 \frac{1}{\cot(\Psi)} \frac{I_0(\alpha a)}{I_1(\alpha a)} I_1(\alpha r) \\ E_z = B_3 I_0(\alpha r) \end{cases} \tag{1.4.20}$$

$$\begin{cases} H_r = B_3 \frac{k}{\omega\mu_0 \cot(\Psi)} \frac{I_0(\alpha a)}{I_1(\alpha a)} I_1(\alpha r) \\ H_\theta = jB_3 \frac{\omega\epsilon_0}{\alpha} I_1(\alpha r) \\ H_z = -jB_3 \frac{\alpha}{\omega\mu_0 \cot(\Psi)} \frac{I_0(\alpha a)}{I_1(\alpha a)} I_0(\alpha r) \end{cases} \tag{1.4.21}$$

The electric and magnetic fields are proportional to the constant B_3. To get the value of B_3, we have to take into account another boundary condition: the discontinuity of the perpendicular magnetic field at the helix.

$$B_\perp^+ - B_\perp^- = \frac{\mu_0 i(\omega, k) \cot(\Psi)}{2\pi a} \tag{1.4.22}$$

with $i(\omega, k)$ the current following the helix direction, i.e. $i(\omega, k) = i_z(\omega, k)/\sin(\Psi)$.

We can reformulate the boundary condition as

$$H_z^+ \cos(\Psi) - H_\theta^+ \sin(\Psi) - H_z^- \cos(\Psi) + H_\theta^- \sin(\Psi) = \frac{i(\omega, k) \cot(\Psi)}{2\pi a}. \tag{1.4.23}$$

We can rewrite this equation as

$$\begin{aligned} &B_3 \frac{\alpha}{j\omega\mu_0 \cot(\Psi)} \frac{I_0^2(\alpha a)}{I_1(\alpha a)} \cos(\Psi) - B_3 \frac{j\omega\epsilon_0}{\alpha} I_1(\alpha a) \sin(\Psi) \\ +B_3 &\frac{\alpha}{j\omega\mu_0 \cot(\Psi)} \frac{I_0(\alpha a) K_0(\alpha a)}{K_1(\alpha a)} \cos(\Psi) - B_3 \frac{j\omega\epsilon_0}{\alpha} \frac{I_0(\alpha a) K_1(\alpha a)}{K_0(\alpha a)} \sin(\Psi) = \frac{i(\omega, k) \cot(\Psi)}{2\pi a} \end{aligned}$$

$$\Rightarrow -jB_3\epsilon_0 \sin(\Psi) \left[\frac{\alpha c^2}{\omega} \frac{I_0^2(\alpha a)}{I_1(\alpha a)} + \frac{\omega}{\alpha} I_1(\alpha a) + \frac{\alpha c^2}{\omega} \frac{I_0(\alpha a) K_0(\alpha a)}{K_1(\alpha a)} + \frac{\omega}{\alpha} \frac{I_0(\alpha a) K_1(\alpha a)}{K_0(\alpha a)} \right] = \frac{i(\omega, k) \cot(\Psi)}{2\pi a}$$

$$\Rightarrow -jB_3\epsilon_0 \sin(\Psi) \left[1 + \cot^2(\Psi)\right] \left[I_1(\alpha a) + \frac{I_0(\alpha a) K_1(\alpha a)}{K_0(\alpha a)} \right] = \frac{\alpha}{2\pi a} i(\omega, k) \cot(\Psi)$$

We can finally express B_3 as

$$B_3 = j \frac{\alpha \sin(\Psi)}{2\pi a \epsilon_0 \omega} \frac{K_0(\alpha_a)}{I_1(\alpha a) K_0(\alpha a) + I_0(\alpha a) K_1(\alpha a)} i(\omega, k) \cot(\Psi) \tag{1.4.24}$$

We replace in this equation α by its expression calculated in (1.4.18) and $i(\omega, k)$ by its expression in $i_z(\omega, k)$ and we obtain

$$B_3 = j \frac{Z_0 \cot^2(\Psi)}{2\pi a} \sqrt{\frac{I_1(\alpha a) K_1(\alpha a)}{I_0(\alpha a) K_0(\alpha a)}} \frac{K_0(\alpha_a)}{I_1(\alpha a) K_0(\alpha a) + I_0(\alpha a) K_1(\alpha a)} i_z(\omega, k) \tag{1.4.25}$$

with $Z_0 = \sqrt{\mu_0/\epsilon_0}$ the vacuum impedance.

We take $i_z(\omega, k) = i_0(\omega) \exp(j(k(\omega)z - \omega t))$ and we can now express the electric and magnetic fields inside the helix as

$$\begin{cases} E_r(r,z,t) = -\frac{Z_0 c}{2\pi h}\int_0^\infty d\omega \frac{1}{v_\phi(\omega)} \frac{K_0(\alpha_a)}{I_1(\alpha a)K_0(\alpha a)+I_0(\alpha a)K_1(\alpha a)} I_1(\alpha r) i_0(\omega)\cos(k(\omega)z-\omega t) \\ E_\theta(r,z,t) = -\frac{Z_0}{2\pi h}\int_0^\infty d\omega \sqrt{\frac{I_0(\alpha a)K_0(\alpha a)K_1(\alpha a)}{I_1(\alpha a)}} \frac{I_1(\alpha r)}{I_1(\alpha a)K_0(\alpha a)+I_0(\alpha a)K_1(\alpha a)} i_0(\omega)\sin(k(\omega)z-\omega t) \\ E_z(r,z,t) = \frac{Z_0 a}{h^2}\int_0^\infty d\omega \sqrt{\frac{I_1(\alpha a)K_1(\alpha a)}{I_0(\alpha a)K_0(\alpha a)}} \frac{K_0(\alpha_a)}{I_1(\alpha a)K_0(\alpha a)+I_0(\alpha a)K_1(\alpha a)} I_0(\alpha r) i_0(\omega)\sin(k(\omega)z-\omega t) \end{cases} \tag{1.4.26}$$

$$\begin{cases} B_r(r,z,t) = \frac{\mu_0 c}{2\pi h}\int_0^\infty d\omega v_\phi(\omega) \sqrt{\frac{I_0(\alpha a)K_1 \alpha a)}{I_1(\alpha a)K_0(\alpha a)}} \frac{K_0(\alpha_a)}{I_1(\alpha a)K_0(\alpha a)+I_0(\alpha a)K_1(\alpha a)} I_1(\alpha r) i_0(\omega)\sin(k(\omega)z-\omega t) \\ B_\theta(r,z,t) = \frac{-\mu_0}{2\pi h}\int_0^\infty d\omega \frac{K_0(\alpha_a)}{I_1(\alpha a)K_0(\alpha a)+I_0(\alpha a)K_1(\alpha a)} I_1(\alpha r) i_0(\omega)\cos(k(\omega)z-\omega t) \\ B_z(r,z,t) = \frac{\mu_0 a}{h^2}\int_0^\infty d\omega \frac{K_1(\alpha_a)}{I_1(\alpha a)K_0(\alpha a)+I_0(\alpha a)K_1(\alpha a)} I_0(\alpha r) i_0(\omega)\cos(k(\omega)z-\omega t) \end{cases} \tag{1.4.27}$$

These are the fields we implement in DoPPLIGHT in Section 2.2.2 in the case of a regular helical coil with a constant pitch and radius.

1.5 Conclusion

The notions introduced in this chapter, from the relativistic laser-plasma interaction to the generation of electromagnetic fields inside a helix, explain the basics of the physics inside helical coil targets and enable us to perform the work presented in this thesis.

The next chapter describes the experimental and numerical tools that I used during my PhD.

Chapter 2

Tools and Methods

In this chapter, I introduce the experimental and numerical tools that were essential for my work during the three years of my thesis. I first present the unfolding of radiochromic films (RCF), the only diagnostic available to obtain the proton spectra of shots in this campaign.

I then describe the numerical tools that I have used throughout my work: both for experimental analysis and theoretical understanding of the physics behind HC targets. First are Particle-In-Cell codes, in particular SOPHIE developed at CEA-CESTA. Secondly, I introduce DoPPLIGHT, the theoretical tool developed by our team in order to design our future experiments. And lastly, I define the numerical parameters used during the simulations and calculations throughout my doctoral work.

2.1 Analysis of radiochromic films

During PACMAN 1 and 2 experiments, the only diagnostic for measuring the proton spectrum at HC exit was a stack of radiochromic films (RCF). In this section, I explain how the spectra from our experimental campaigns were determined from the irradiated RCFs. The method comes from the work of I. Lantuéjoul and B. Vauzour at CEA-DIF [83].

2.1.1 Theoretical unfolding of radiochromic films

As protons pass through the films, the radiosensitive coating of the films darkens as a function of the energy deposited by the beam, as shown in Figure 2.1. A calibration of this relation between optical density (OD) and the deposited energy in a film has been made by I. Lantuéjoul and B. Vauzour at CEA-DIF [83].

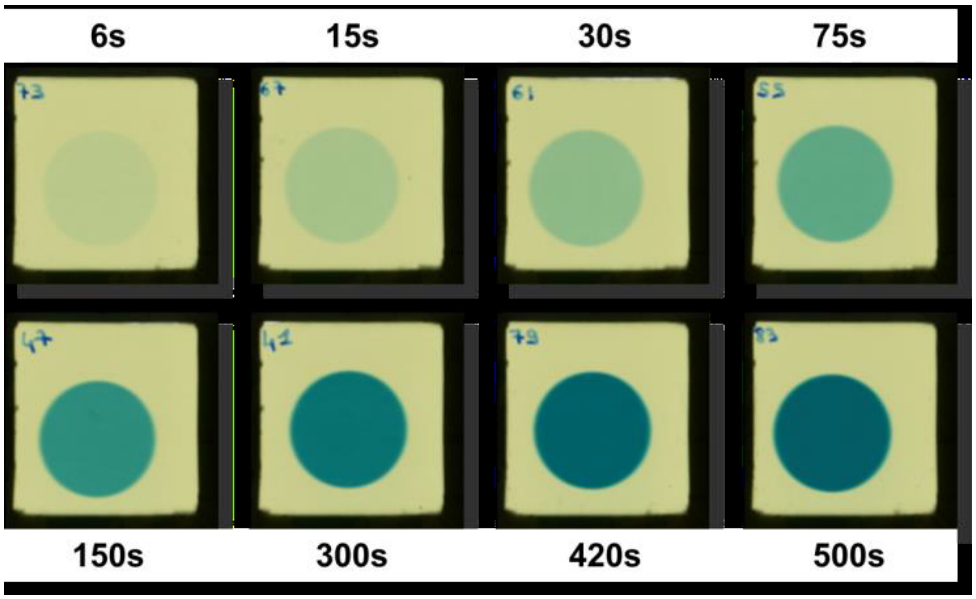

Figure 2.1 – Progressive darkening of HDV-2 radiochromic film as a function of the irradiation time (i.e. the deposited energy) on a 4MV Van de Graaff particle accelerator [I. Lantuéjoul].

When a proton interacts with matter, it loses its energy along its path inside the traversed matter following a Bragg curve - an example can be seen in Figure 2.2: first in a relatively uniform manner before depositing the majority of its energy in a very localised spatial zone around the Bragg peak. The shape of this curve depends on the traversed matter and on the incident proton energy. We can then attribute to each film a depth and an associated energy of the protons stopped by that film. Low energy protons deposit their energy in the first films, and the high energy ones in the last films of the stack.

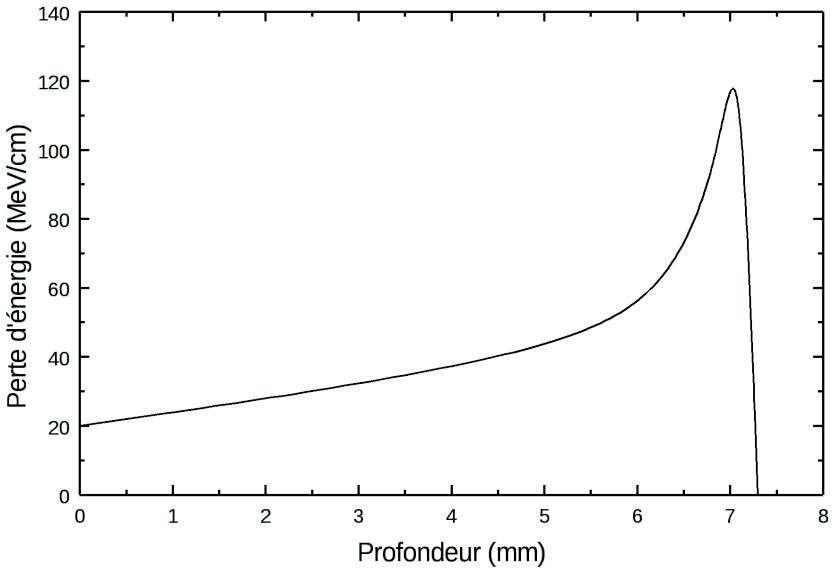

Figure 2.2 – Example of a Bragg curve.

2.1.1.1 First and second-order approximation

For the PACMAN campaigns, these energies have been determined by I. Lantuéjoul and B. Vauzour using Monte-Carlo simulations and the response function. The results are shown in Figure 2.3.

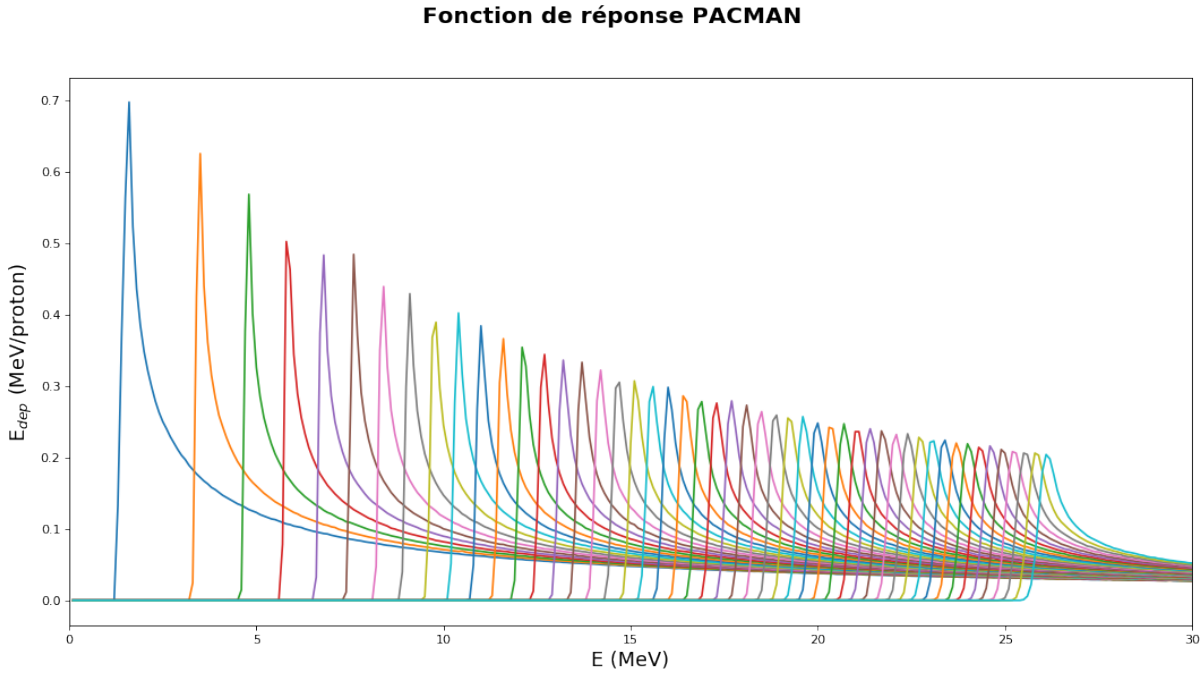

Figure 2.3 – Response function of the RCF stack used during the PACMAN campaigns shots. Each curve describes the deposited energy in a film i as a function of the proton energy before it is slowed down by the RCF stack. Each curve corresponds to a different film in the stack, going from the front to the back of the stack from left to right.

For the analysis of PACMAN 1 results, a first-order approximation was made to analyse the spectrum: protons stopping in the film i deposit all of their energy in this film. In this case we have a non-deconvoluted spectrum. It was then quickly upgraded to a second-order approximation where the protons stopping in the film i also deposit energy in films 1 to $i-1$.

We set X_{films} to be the total number of films, $f_i(E)$ the response function of film i depending on the incident proton energy, E_i the Bragg peak energy associated with the film i, $E_{i,\text{dep}}$ the deposited energy in the film i and N_i the number of protons of incident energy E_i. We calculate N_i using the formula,

$$N_i = \frac{\left(E_{i,\text{dep}} - \sum_{j=i+1}^{X_{\text{films}}} N_j f_i(E_j)\right)}{f_i(E_i)}. \tag{2.1.1}$$

2.1.1.2 Third-order approximation

For the PACMAN 2 campaign, a third-order analysis was used. We first define the number of irradiated films from the experimental shot and we define E_i as in the previous method. For each film, we set ΔE_i the interval in energy between two films, from the point before the Bragg peak where the energy deposited is half the maximum observed at the Bragg peak to the equivalent point on the film $i+1$. For the last film, we simply set $\Delta E_{X_{\text{films}}} = 1$ MeV. Ideally, we want a signal-free last film so that the bin width has no importance. We then calculate the average energy deposited in film i by the protons stopped in film j, which we call $e_{\text{moy,i,j}}$. This is represented in Figure 2.4.

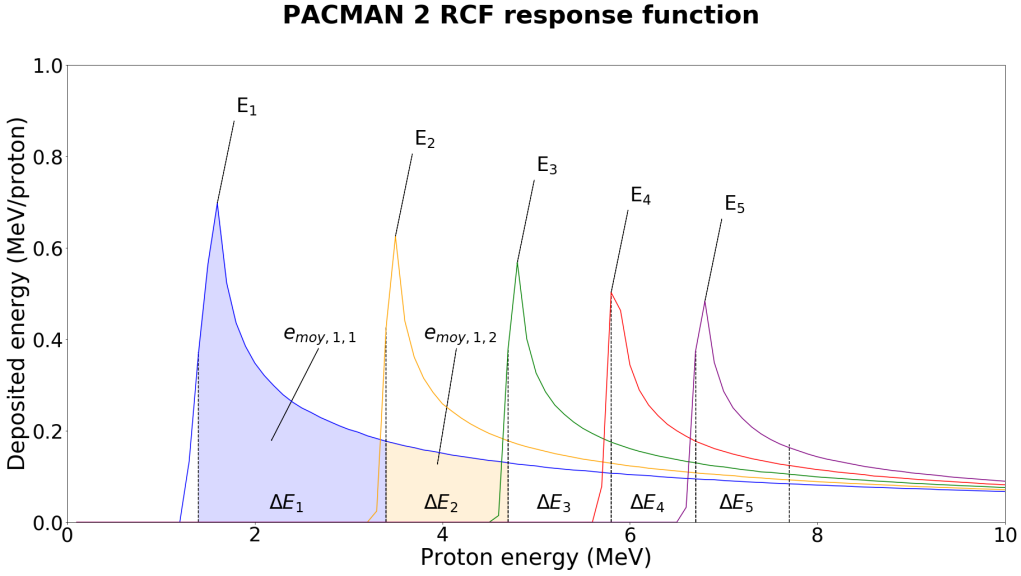

Figure 2.4 – Treatment of an RCF stack response function to unfold the spectrum of a shot.

Once all of this is calculated we can then unfold the spectrum with the following method:

— We first measure the total deposited energy in film i. The method is explained in the next section.

— We then calculate the number of protons stopped in the last film with a simple division

$$\frac{\Delta N_{X_{\text{films}}}}{\Delta E_{X_{\text{films}}}} = \frac{e_{\text{dep,total,X}_{\text{films}}}}{e_{\text{moy,X}_{\text{films}},\text{X}_{\text{films}}}} \tag{2.1.2}$$

— Finally, going backwards from film $N-1$ to film 1, we calculate the number of protons stopped in bin ΔE_i via the following formula:

$$\frac{\Delta N_i}{\Delta E_i} = \frac{\left(e_{\text{dep,total,i}} - \sum_{j=i+1}^{X_{\text{films}}} \frac{\Delta N_j}{\Delta E_j} \times e_{\text{moy,i,j}} \right)}{e_{\text{moy,i,i}}} \tag{2.1.3}$$

At the end of this unfolding, we obtain the number of protons per energy bin. We then normalise these values to obtain the spectrum in N_{protons}/MeV. The difference with the second-order is that we do not take the maximum energy of the response function into account but the mean energy in a ΔE bin.

2.1.1.3 Test case validation

To validate this new analysis method, a set of GEANT 4 simulations was undertaken by I. Lantuéjoul and B. Vauzour. The goal is to retrieve, with the unfolding method, the proton spectrum set as input to the GEANT 4 simulation. The simulation consists of irradiation by a known and chosen proton beam of an RCF stack identical in composition to the ones used in the experiment. Each simulation output is the energy deposited in

every simulated film of an RCF stack, pixel per pixel. Several RCF stack layouts and input spectra have been tested [83]. The method has been tested with the same process for a PACMAN spectrum.

Test case PACMAN The case *PACMAN* is a test case representing the PACMAN experiment [39]. The layout of the RCF stack corresponds to any shot of the campaign, composed of 50 HDV2 films. We have 50 images of 600x600 pixels at a resolution of 600 dpi, as in the experiment. These images are in the format of 2D histograms. We also have the input spectrum as a 1D histogram. The proton source is circular, with a 10 mm diameter, emitting normally to the RCF stack. Their energy distribution follows the output results of a large-scale Particle-In-Cell simulation of the PACMAN experiment. The simulations were made for 10^7 incident protons.

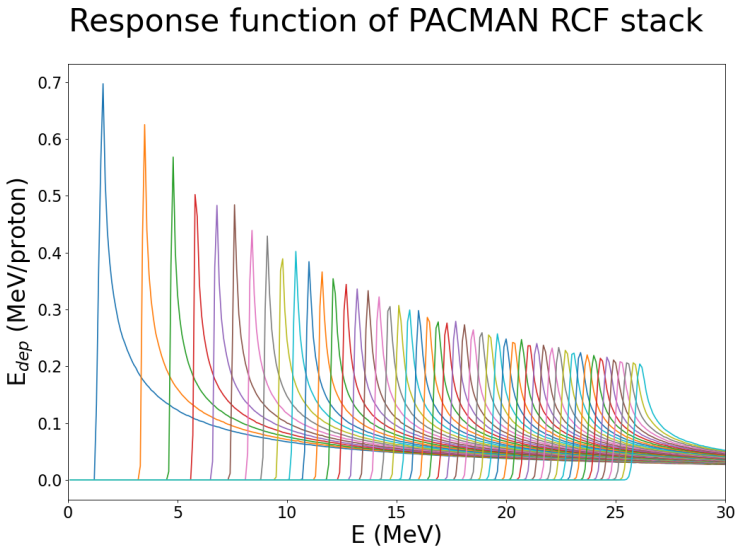

Figure 2.5 – Response function of the RCF stack of the *PACMAN* test case.

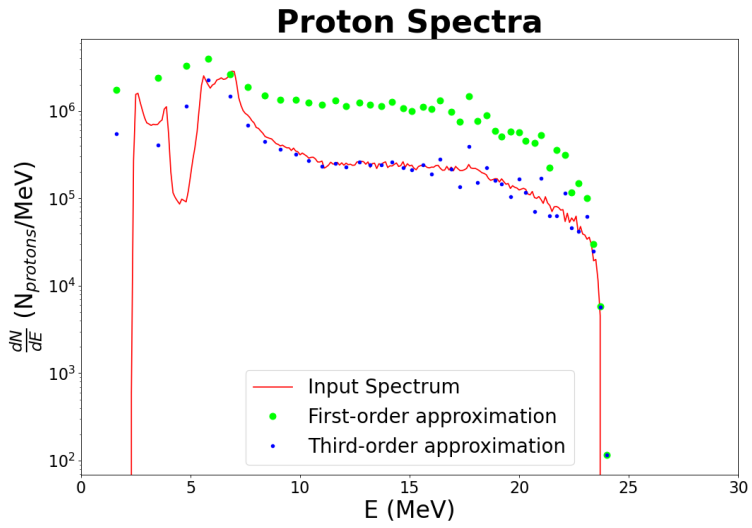

Figure 2.6 – Input spectrum (red line), first-order approximation spectrum unfolding (green dots) and third-order approximation spectrum unfolding (blue dots) for the *PACMAN* test case.

Conclusion After the deconvulotion method on a simulated PACMAN spectrum, we have a very good agreement between the unfolded spectra using the third-order approximation and the input spectra, which proves the efficiency of our unfolding method.

2.1.2 Experimental method analysis

To unfold the experimental spectra from our RCF stacks scans, I developed a Matlab code adapted to reading and analysis of the experimental data obtained during the PACMAN 1 and 2 experiments. This code can also be used for other similar experiments.

It is suitable to any stack made of HDV2 and/or EBT3 RCFs and of any form as long as they are scanned in one image. The program can only read TIFF files, both in black and white and in colour. Figure 2.7 is an example of such a scan.

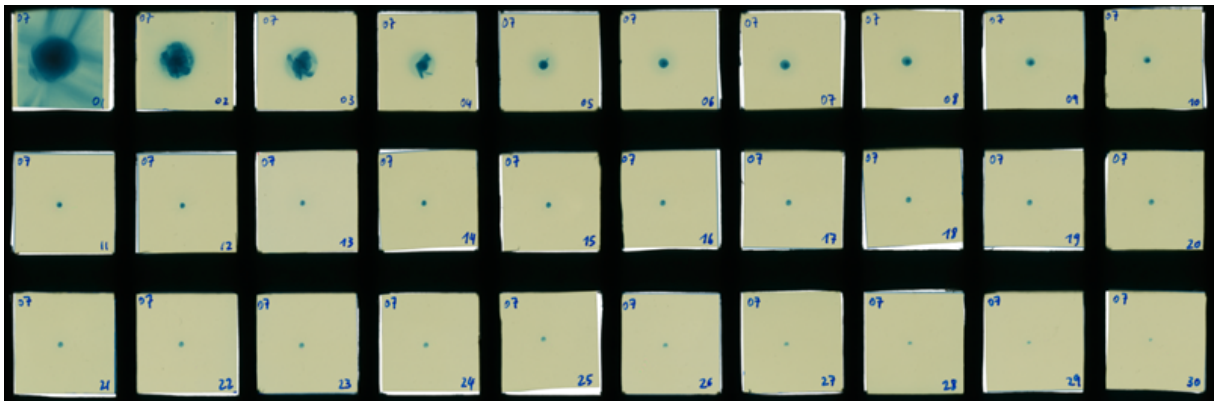

Figure 2.7 – Scanned RCF stack after a shot of the PACMAN2 campaign.

Selection of the regions of interest First of all, we must select the region of interest (ROI) for each shot and on every single film as well as the last film where the beam darkened the film. To achieve that, we increase the contrast of the image artificially to see the last film and the clear outline of the spot which is not visible without contrast. In Figure 2.8, we can clearly observe the absence of signal on the 29th film of the stack.

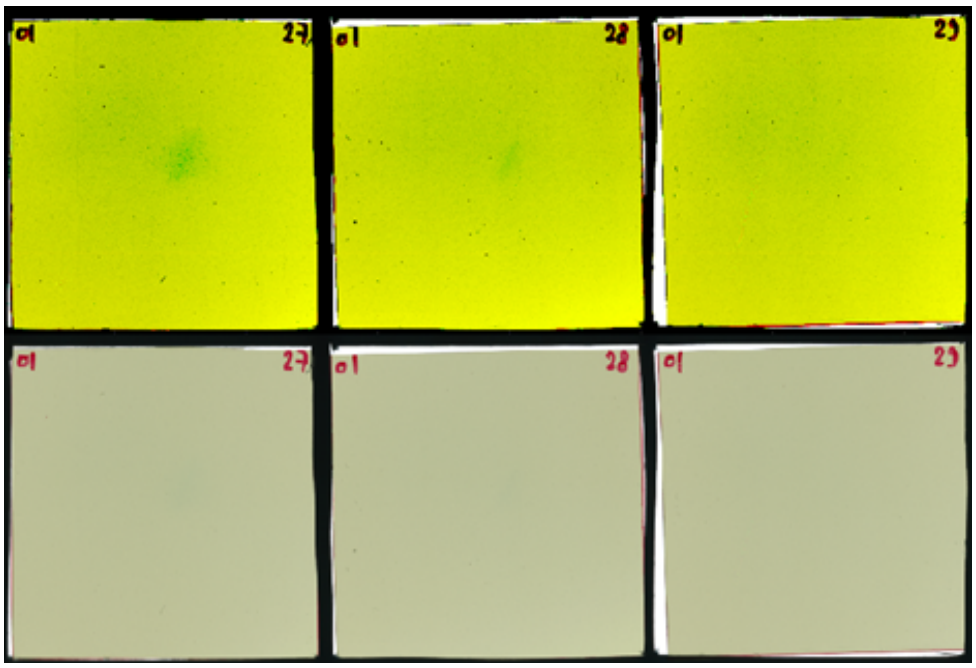

Figure 2.8 – Contrast enhanced (on top) vs. original (bottom) irradiated RCF films.

The program asks us to select the centre of the spot to observe the spectrum in a specific radius or to select the full spot shape only on every film by drawing a polygon filter on the contrast-enhanced image.

The contrast-enhanced image also allows us to select a non-irradiated part on each film so we can measure the background signal on each film and measure the optical density at the next step.

Calculation of the deposited energy To obtain the spectrum via the unfolding algorithm presented previously, we need to calculate from the TIFF file the deposited energy in every film. For that, the first step is to calculate the optical density of each of the RGB channels in the ROI using the formula

$$\mathrm{OD_i} = -\log_{10}\left(\frac{\mathrm{I_i}}{\mathrm{I_{0,i}}}\right) \tag{2.1.4}$$

where i is one of the RGB channels, I_i is the intensity of the signal of the selected channel in the ROI and $I_{0,i}$ is the intensity of the signal of the selected channel in the background region. If the OD is negative, it is brought back to 0 as if there were no signal.

The sensitivity of every channel being different, the RGB files allow a finer calculation of the spectrum than B&W as we can select the channel according to the sensitivity of the channel. By default, we chose the blue channel. If the OD in the ROI is superior to 0.9, we consider the film saturated, and if it is less than 0.1, we switch to the green channel. Then, if the OD of the green channel is less than 0.1 we switch to the most

sensitive red channel. Finally, if the OD of the red channel is less than 0.01, then the signal is insufficient to be processed and the OD is fixed to 0.

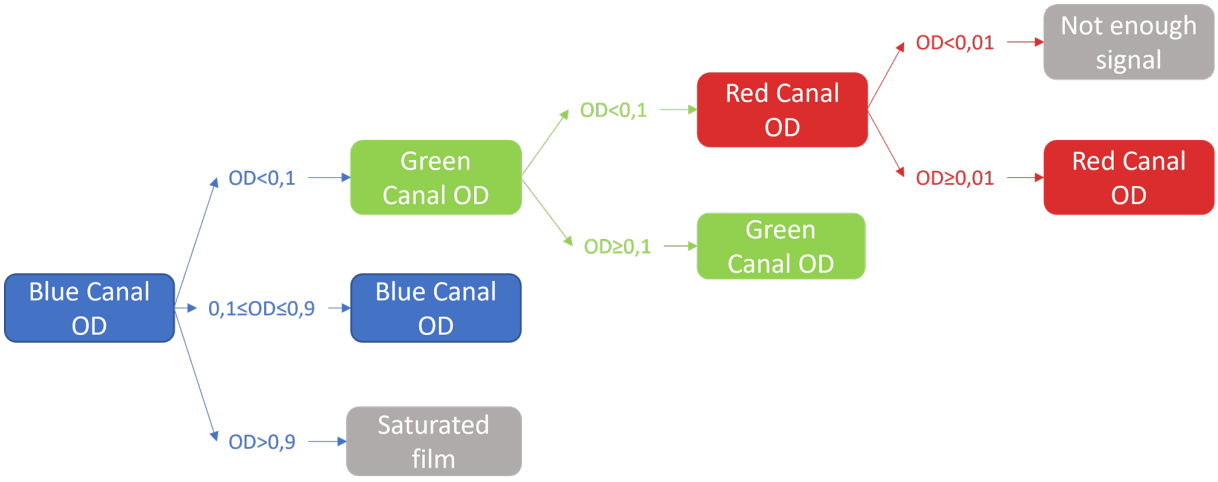

Figure 2.9 – Channel choice selection algorithm according to the OD.

Once we obtained the OD, we calculate the deposited energy in the films using a function obtained during the calibration measurement of the RCF made on the particle accelerators 4MV and NENUPHAR at CEA-DAM:

$$E_{\text{dep}} = \exp\left(A + B \times \text{OD}^{\text{k}} + \text{C} \times \text{OD} + \text{D} \times \text{OD}^2\right) \tag{2.1.5}$$

with the values of the coefficients A, B, C, D and k calculated experimentally by I. Lantuéjoul and B. Vauzour [83] and given in Table 2.1:

	A	B	C	D	k
HDV2 Red Channel	15.5	11.3	-1.8	1.7	0.2
HDV2 Green Channel	18.7	15.3	-12.2	8.0	0.4
HDV2 Blue Channel	17.4	10.5	1.2	1.6	0.2

Table 2.1 – Parameters of the calibration function of HDV2 films.

From this formula, we obtain the total deposited energy in the ROI. By applying the unfolding algorithm I introduced previously, we obtain the energy spectrum of the proton beam in $N_{\text{protons}}/\text{MeV}$.

2.2 Numerical Tools

In this section, I describe the main numerical tools I used during my work: the Particle-In-Cell (PIC) code SOPHIE developed by Olivier Cessenat at CEA-CESTA and the theoretical model DoPPLIGHT developed with Matthieu Bardon and Clément Lacoste at CELIA, specifically designed to model helical coil targets.

2.2.1 SOPHIE

To present the code SOPHIE, I first discuss general features of a PIC code and then describe the details of SOPHIE.

2.2.1.1 Particle-In-Cell codes

PIC codes are very powerful tools for modelling plasma physics. They were first developed in the 1950s to simulate the macroscopic behaviour of plasmas [84]. To simulate a plasma (or, in our case, a particle beam, which we can consider as a non-neutral plasma), we need to understand how it behaves.

A plasma is a state of matter where part or all of the matter is ionized, meaning a plasma is composed in majority or exclusively of ions and electrons. Its behaviour, both on the macroscopic scale and on the individual particle state, is dominated by the electromagnetic force, expressed by the Lorentz force as follows

$$\frac{\mathrm{d}\mathbf{p}}{\mathrm{d}t} = q\mathbf{E}(\mathbf{r},t) + q\mathbf{v} \wedge \mathbf{B}(\mathbf{r},t) \tag{2.2.1}$$

with $\mathbf{r}$ the particle's position, $\mathbf{v}$ its velocity, $\mathbf{p}$ its momentum defined as $\mathbf{p} = \gamma m\mathbf{v}$, m the particle's mass, q its charge, $\gamma = \sqrt{1 + (p/mc)^2}$ its Lorentz factor, t the time, $\mathbf{E}$ the electric field and $\mathbf{B}$ the magnetic field.

In vacuum, the electromagnetic fields $\mathbf{E}$ and $\mathbf{B}$ follow the Maxwell equations:

$$\nabla \cdot \mathbf{E} = \frac{\rho}{\epsilon_0} \tag{2.2.2}$$

$$\nabla \cdot \mathbf{B} = 0 \tag{2.2.3}$$

$$\frac{\partial \mathbf{B}}{\partial t} = -\nabla \wedge \mathbf{E} \tag{2.2.4}$$

$$\frac{\partial \mathbf{E}}{\partial t} = c^2 \nabla \wedge \mathbf{B} - \frac{1}{\epsilon_0}\mathbf{J} \tag{2.2.5}$$

with ϵ_0 the vacuum permittivity, ρ the electric charge density and $\mathbf{J}$ the electric current.

The electromagnetic fields are the sum of contributions of every charged particle and current propagating in space. This physical phenomena is self-consistent as the fields apply to the particles, modify the charge density and the electric current, which then modify the electromagnetic fields and so on.

If we had to take into account every particle, this would become a very lengthy process as our proton beams are composed of 10^{10} up to 10^{14} particles, each of them impacting the others in an 'N-body' problem. To reduce the complexity of the simulation, PIC codes use macro-particles following these conditions:

— they have the same q/m ratio as the real particles
— they follow the same dynamics in the electromagnetic fields as the real particles introduced previously
— they are defined by a distribution function f following the Vlasov equation:

$$\frac{\partial f}{\partial t} + \mathbf{v} \cdot \frac{\partial f}{\partial \mathbf{r}} + q(\mathbf{E} + \mathbf{v} \wedge \mathbf{B}) \cdot \frac{\partial f}{\partial \mathbf{p}} = 0 \tag{2.2.6}$$

All of this leads to the PIC loop which is shown in Figure 2.10

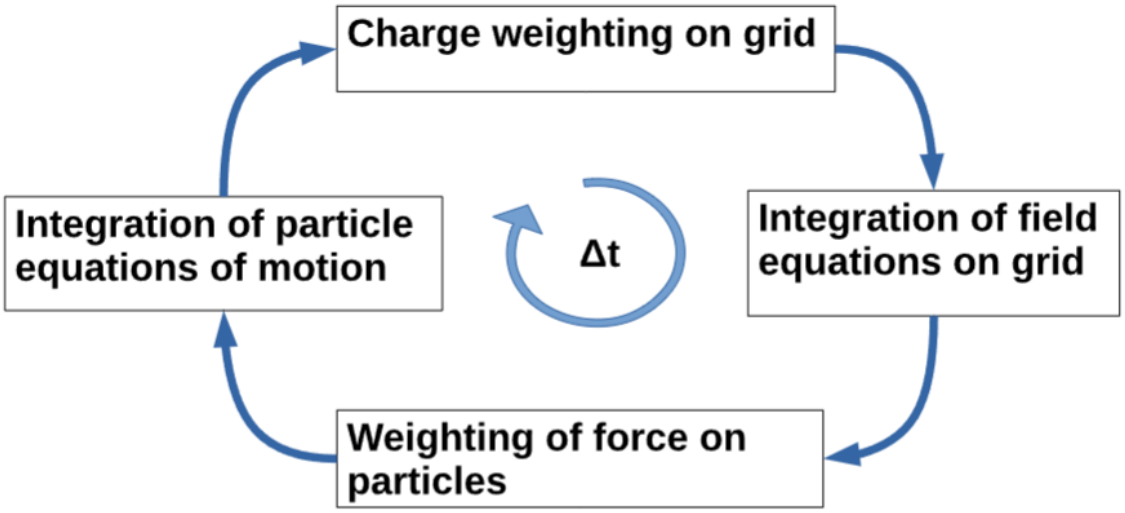

Figure 2.10 – Description of a PIC loop on a time-step of length Δt [85].

At every time-step, a PIC code must follow four successive steps:
— Interpolate the electromagnetic fields on the position of every macro-particle.
— Solve the dynamics for every macro-particle and determine their new position $\mathbf{r_t}$ and velocity $\mathbf{v_t}$ at the time-step t.
— Interpolate the new charge distribution ρ and current $\mathbf{J}$ on the mesh grid.
— Solve the Maxwell equations on the grid to obtain the new fields $\mathbf{E}$ and $\mathbf{B}$.

In conclusion, a PIC code solves the fields and particles propagation in a self-consistent way.

2.2.1.2 Description of SOPHIE

Now that we know the fundamentals of how a PIC code works, we can describe the specifics of SOPHIE and why we chose this code. SOPHIE is a PIC code developed at CEA-CESTA by Olivier Cessenat [86].

It is a Finite Difference in Time Domain (FDTD) code [87] developed specifically for the CEA high-performance computing (HPC) centre, which is highly parallelised. First adapted for the Tera 10 supercalculator of CEA/DAM, it has been adapted for every subsequent upgrade of the CEA HPC center, which is now Exa 1 (or CEA-HF) [88].

SOPHIE is a 3D FDTD-PIC code that solves, in a self-consistent manner, Maxwell's equations for the fields propagation in vacuum as well as in matter, using boundary conditions such as a perfect electric conductor, dielectric and magnetic materials, and then Newton's second law of dynamics for the propagation of relativistic particles in vacuum using Boris' solver [89]. Self-consistence is achieved using Buneman currents collector. SOPHIE allows a limited sub-cycling of Vlasov steps: a particle may not travel over more than the distance that light can achieve over the associated Maxwell steps. This is an implementation choice for easing particles communication using MPI, not a CFL constraint. Maxwell's equations are solved on the so-called Yee mesh with centered electric and magnetic fields using the finite-difference time-domain (FDTD) method or related methods.

SOPHIE is designed for high performances on massively-parallel super-computers as well as on a set of workstations - or "grid" - using a multi-blocks (aka multi-domains) per process feature that enables reasonable load balancing even for highly space charged

configurations. For the highly tuned performance of SOPHIE for multi-core processors, at best reusing cache [86], it implements an MPI scheme where computations are overlapped with only one communication array over a full Maxwell step. It also implements a standard fine grain OpenMP parallelism for EM fields, as well as over particles in a given domain, but also a coarse grain OpenMP dynamic load balancing over blocks (i.e. domains), both for fields and particles.

A separate mesh tool has been developed at CEA/CESTA, the meshing file is an ASCII file that can be generated by any other means. A key feature of Sophie for performing numerical experiments that aim to better understand physics, is its deep interaction with "VisIt" [90] where SOPHIE can generate Silo files at a requested time frequency, for specific zones. VisIt allows second to none 3D parallel scalable visualization.

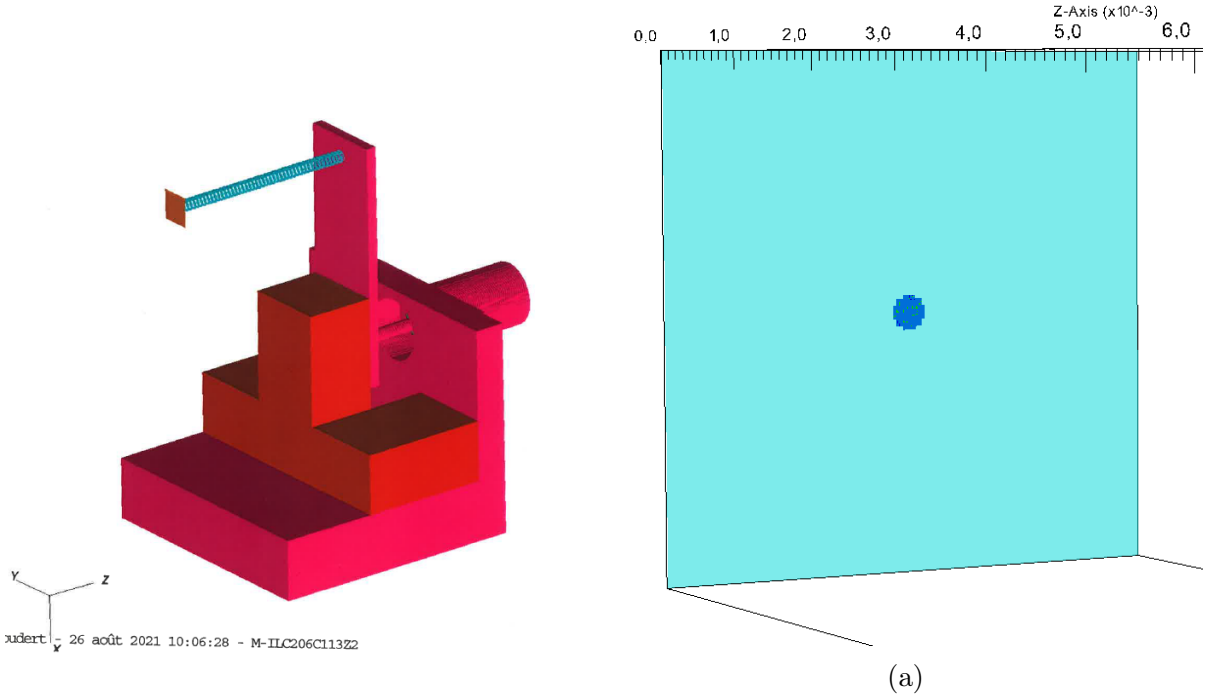

(a)

Figure 2.11 – Mesh of (a) a PACMAN 2 full target and (b) a gold foil of thickness $e = 20$ μm with an emissive zone of radius $r = 100$ μm for a SOPHIE simulation.

Contrary to usual PIC codes in the fields of laser-plasma acceleration, SOPHIE is not used to model a plasma on a short time scale and in a small simulation box, such as CALDER [91] or Smilei [92]. It is used on large scale grids (of the order of several cm) and long time scale (of the order of the ns) to model the propagation of the current through the helical coil and the propagation of a particle beam in vacuum. Boundary conditions such as perfect electric conductor enable to simulate the fields propagation at the mesh surface without the need of macroparticles to propagate the current $\mathbf{J}$. This relaxes the constraints on the problem size. The boundary conditions allow simulations of perfectly conductive and dielectric materials.

Input of particles and current SOPHIE's input for particles is defined in the block SOUR of the input file. First, an emissive surface is designed, which can emit several types of particles at once. Every spectrum must be defined as follows:

— the ratio q/m of the particle composing the emitted beam

— the charge Q of the emitted beam

— a normalised fluence law: $\frac{\mathrm{d}N}{\mathrm{d}t}$
— two normalised angular laws in both θ and ϕ: $\frac{\mathrm{d}N}{\mathrm{d}\theta}$ and $\frac{\mathrm{d}N}{\mathrm{d}\phi}$
— a normalised law in energy $\frac{\mathrm{d}N}{\mathrm{d}E}$
— the number of macro-particles to be emitted

In SOPHIE all of the distribution laws are uncorrelated and the particles are emitted from the designated emissive surface.

Finally, the current source terms is self-generated by the particle emission. Any charged particle emitted creates a current of opposite sign at the point of exit and any particle absorbed by a material creates a current of the same sign at the point of contact. In both case, the amplitude is equal to the charge divided by Δt, the length of a time-step.

Output diagnostics SOPHIE presents several different systems enabling us to study the physics of helical coil targets used during my work:

— CIRC: a current diagnostic in the shape of a circle or a square. By integrating the magnetic circulation along the path of the CIRC, it gives the current going through the diagnostic. Usually with an acquisition frequency of 1 save every 10 time steps.
— CIRP: a particle diagnostic in the shape of a disk. At every time step, the CIRP notes the energy of all the particles with the selected q/m ratio. Once integrated in time, one gets the spectrum $\frac{\mathrm{d}N}{\mathrm{d}E}$ of the particles that passed through the disk. The acquisition frequency is 1 save every time step.
— OBSC: a selection of grid points at which SOPHIE saves the electric field, magnetic fields and electric current in all three dimensions. Usually with an acquisition frequency of 1 save every 10 time steps.
— MOUT: a visualisation diagnostic, enabling mapping of the electric and magnetic fields in 3D with the mesh. Usually with an acquisition frequency of 1 save every 100 time steps.
— VOUT: a visualisation diagnostic, enabling mapping the particle position, energy and velocity in 3D with the mesh. Usually with an acquisition frequency of 1 save every 100 time steps.

Figure 2.12 shows the representation of CIRCs and CIRPs in a mesh for a simulation of a shot with a HC.

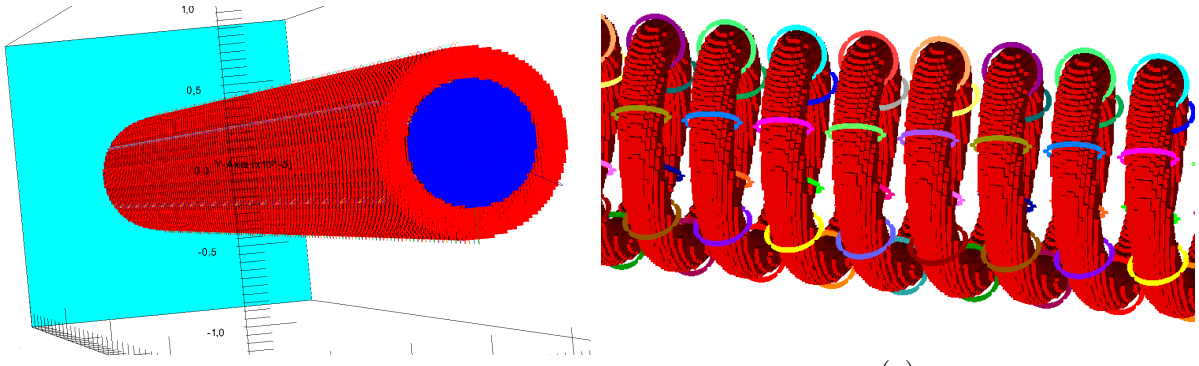

(a)

Figure 2.12 – Mesh of a HC with (a) a CIRP at the exit and (b) 6 CIRC diagnostics per loop.

In conclusion, SOPHIE is adapted to geometries of helical coils and for simulation of the proton beam dynamics and current propagation on the time-scale we need to study.

Its agreement with experimental data in the case of HC has been proven during the PACMAN 1 campaign by Julien Moreau and Matthieu Bardon [39].

2.2.2 DoPPLIGHT

The second numerical tool used during my work is the theoretical code DoPPLIGHT (Dynamics of Particles Produced by Laser Interaction in Grounded Helical Targets) developed in our team [93]. Originally developed by Matthieu Bardon and Julien Moreau, additional modules and updates have been added by Clément Lacoste and myself throughout the last three years.

2.2.2.1 Structure of the code DoPPLIGHT

The workflow of the model DoPPLIGHT, represented in Figure 2.13, can be summarised as follows:

— It takes as input the helix geometry, the particle source terms and the current at the input of the helix in the time domain $i_{z=0}(t)$. It is possible to input several particle species or several sources of the same particle species. The geometries supported during my work were only helices with constant pitch and radius, but the implementation of varying pitch and radius has been completed by Clément Lacoste and Matthieu Bardon in October 2023.

— It then performs a Fourier transform of the current and uses it to calculate the fields according to Maxwell's equations. The boundary conditions are defined at the radius $r = a$ (with a the helix radius). Following Pierce [80], the coil is modeled as an infinitely thin cylinder with the current propagating in the helical direction, the sheath helix model is presented in Section 1.4. The tube is modeled as a perfect conductor. The fields are then transformed in the space-time domain by applying the inverse Fourier transform. These calculations in the case of a helix with constant pitch and radius have been introduced in Section 1.4.

— The DoPPLIGHT model also calculates the space charge fields for a Gaussian shaped non-relativistic proton beam. This module was developed by myself and Matthieu Bardon and is presented in Chapter 4.

— The protons and electrons are then injected into the coil and their trajectories are calculated with the Boris pusher with the helix and space charge fields interpolated at each time step on the particle's position. At the exit of the coil, the code can calculate the proton energy distribution and their positions.

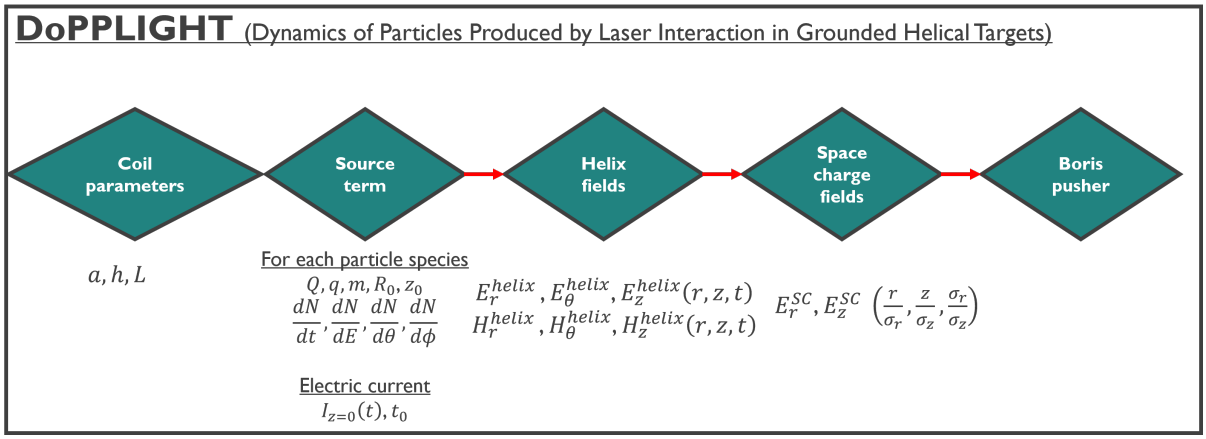

Figure 2.13 – Scheme of DoPPLIGHT modules and calculation steps.

DoPPLIGHT operates in a 2D-axi-symmetric geometry; it is time-resolved but not a self-consistent model. Contrary to a full-scale PIC simulation which takes between 5000 and 20000 hours.processors on a super-computer like EXA 1, a DoPPLIGHT calculation runs in 5 to 10 minutes on a laptop.

In addition to the gain in calculation time compared with a PIC code, DoPPLIGHT also has the advantage of not needing to generate a simulation mesh for every run, as it just needs an input file with a new coil geometry.

2.2.2.2 Validation of the code DoPPLIGHT

Now that we have explained how the theoretical code DoPPLIGHT works, we need to validate its results by comparing with our PIC code results.

Firstly, a PIC simulation with only hot electrons emitted has been performed, to observe the fields generated by the discharge current propagating through the helix and compare them with the DoPPLIGHT calculated fields when injecting the same current [93].

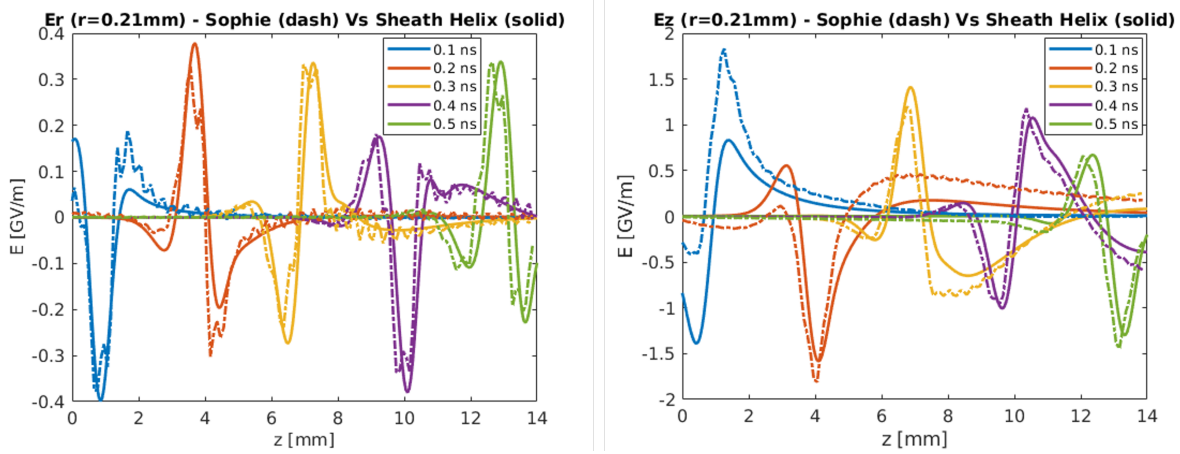

Figure 2.14 – Comparison of DoPPLIGHT calculated (full lines) and PIC simulated (dashed lines) radial (left) and longitudinal (right) electric fields as a function of z in the case of an emission of hot electrons only. The HC parameters are: length $L = 15$ mm, radius in the heart of the coil $a = 0.5$ mm, external radius 0.6 mm and step $h = 0.35$ mm. The particles features are defined in Table 2.2 for LULI. The current is defined analytically by a Gaussian with FWHM $\tau_{FWHM} = 8.5$ ps and amplitude $I_0 = 30$ kA at $z = 0$ mm, delayed with respect to the particle emission by 6 ps.

In Figure 2.14, we observe a good agreement of the radial and longitudinal electric fields, i.e. the dominant fields on the proton dynamics, between the theoretical model DoPPLIGHT and the PIC code SOPHIE. This agreement is sufficient to validate the fields calculation in DoPPLIGHT.

We then need to validate the dynamics of the protons inside the helix in DoPPLIGHT. For that, we add the emission of protons in both DoPPLIGHT and SOPHIE and observe the proton spectrum at the exit of the helical coil [93].

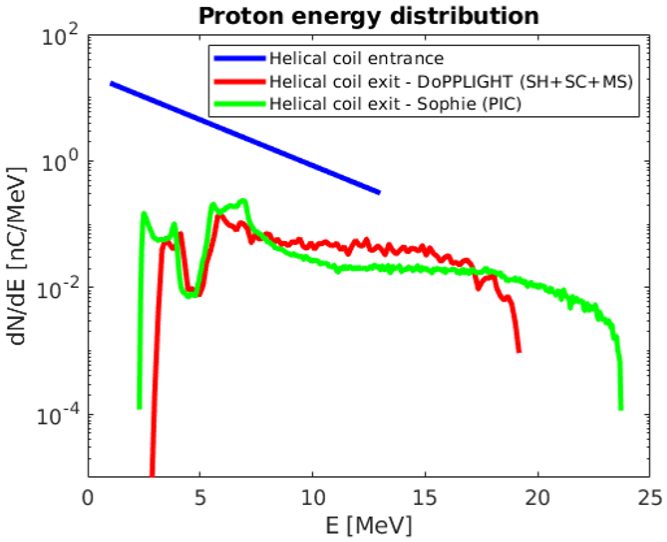

Figure 2.15 – Comparison of the DoPPLIGHT calculated (red line) with all the modules (sheath helix model (SH), space charge fields (SC), multi-species (MS)) and PIC simulated (green line) proton spectrum at the exit of the coil. The blue line is the input spectrum. The HC parameters are: length $L = 15$ mm, radius in the heart of the coil $a = 0.5$ mm, external radius 0.6 mm and step $h = 0.35$ mm. The particles features are defined in Table 2.2 for LULI. The current is defined analytically by a Gaussian with FWHM $\tau_{FWHM} = 8.5$ ps and amplitude at $z = 0$ mm $I_0 = 30$ kA, delayed with respect to the particle emission maximum by 6 ps.

We see in Figure 2.15 two very similar spectra at the exit of the coil between SOPHIE and DoPPLIGHT. While we observe differences between the two, especially in terms of cut-off energy, we have a fairly good agreement in terms of proton charge and structures in the spectrum at low and medium energy.

In conclusion, while the agreement is not perfect between DoPPLIGHT and SOPHIE, it is sufficiently close to be able to use DoPPLIGHT in the study of the physics inside an HC targets. As it is faster to use, DoPPLIGHT enables us to run a larger number of case. Only interesting cases are run with full-scale PIC simulations.

2.2.2.3 Outputs of the code DoPPLIGHT

DoPPLIGHT offers a large amount of diagnostic outputs for the study of the current and fields propagation as well as the particle dynamics:

- Observation of the current and electromagnetic fields at any position and time of the grid (r, z, t).
- Colourmap of the current and electromagnetic fields as a function of time and longitudinal position.
- Tracking of particle position and energy throughout their propagation inside the helix. This can only be done for a limited number of particles because of memory limits of laptops.
- Observation of the exit output energy of a particle as a function of its input energy,.
- Proton spectrum at the exit of the helical coil.

With such a variety of diagnostics, DoPPLIGHT is a tool adapted to the study of the physics inside helical coils and for the design of future experiments.

2.2.3 Numerical Parameters

Throughout this manuscript, many PIC simulations and theoretical model calculations are presented. I introduce in this section the essential numerical parameters used for them.

2.2.3.1 Particle source terms

I introduce the source terms of the particle population emitted during my simulations and calculations. Simulations and calculations have been performed for two different sets of laser parameters, one corresponding to the ALLS laser facility at INRS [94], and the other corresponding to the PICO2000 laser beam at LULI2000 [40]. In each case, the emitted particles are separated into two different populations: the first consists of protons, with charge and energy distributions taken from experimental data [39], [75], which also provides the co-moving low energy electron charge distribution. The second population consists of fast electrons, with charge and temporal distributions calculated from the numerical model ChoCoLaT [95], developed by Poyé *et al.*, with the laser parameters of each facility. We assume the same temporal distribution for protons and electrons. The source terms of ejected particles are defined in Table 2.2:

	ALLS	PICO200
Energy distribution	Maxwellian, $T = 0.9$ MeV	Maxwellian, $T = 2.9$ MeV
Energy range	1 MeV$< E <$ 6 MeV	1 MeV$< E <$ 19 MeV
Temporal distribution	Gaussian, $\tau = 3$ ps	Gaussian, $\tau = 10$ ps
Proton charge	$Q_p = 12$ nC	$Q_p = 175$ nC
Fast electron charge	$Q_e = 160$ nC	$Q_e = 600$ nC

Table 2.2 – Physical parameters of the ALLS and PICO2000 TNSA proton and fast electron populations.

In both cases, the proton and co-moving electron angular distribution has the shape of a super-Gaussian function, defined by the function $\exp\left(-\frac{1}{2}\left(\theta/\theta_{\mathrm{p}}\right)^{10}\right)$, centred around the longitudinal axis and defined by $\theta_{\mathrm{p}} = 19°$ while the fast electron population is isotropically ejected in a solid angle of 2π.

The particle source terms also serve as a current source for the PIC simulation, as explained in Section 2.2.1.

2.2.3.2 Mesh parameters for PIC simulations

For all PIC simulations, the mesh characteristics have been set with fixed parameters: the solid structures in this set of simulation (target foil, coil and grounds) are modelled with a resolution of $\Delta x = \Delta y = \Delta z = 20$ μm as shown in Figure 2.16.

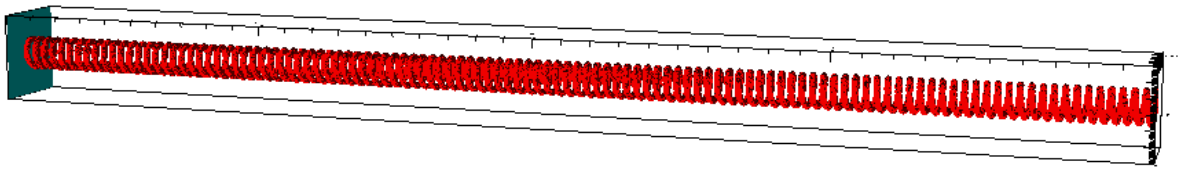

Figure 2.16 – Mesh of a HC in SOPHIE. The target is in cyan and the helical coil in red.

2.2.3.3 Mesh parameters for DoPPLIGHT

For all DoPPLIGHT calculations, the simulation box was discretised with $\Delta r = 50\ \mu$m and $\Delta z = 50\ \mu$m, with a time-step $\Delta t = 0.4$ ps in the case of a ALLS input spectrum and $\Delta t = 2$ ps in the case of a LULI input spectrum. The current is defined analytically by a Gaussian function with full width at half maximum (FWHM) $\tau_{FWHM} = 3$ ps and amplitude $I_0 = 7$ kA at $z = 0$ mm for ALLS and by a Gaussian function with full width at half maximum (FWHM) $\tau_{FWHM} = 8.5$ ps and amplitude $I_0 = 30$ kA at $z = 0$ mm for LULI2000.

2.3 Conclusion

In this chapter, I introduced the essential tools for my doctoral work. First is a description of the unfolding of a proton energy spectrum from the scan of a RCF stack. Then the numerical tools with an introduction of PIC codes are presented, in particular the PIC code SOPHIE developed at CEA-CESTA, and our theoretical model DoPPLIGHT developed specifically for the study of helical coil targets.

These tools are used in the next chapter where I analyse the results of the experimental campaign PACMAN 2 whose goal was to study the parametric variations of the helical coil geometry and their impact on the proton beam.

Chapter 3

Analysis of the experimental campaign PACMAN 2

The objective of this chapter is to observe the impact of parametric variations of helical targets on the TNSA proton beam, which was the aim of the PACMAN 2 campaign. I first studied the impact of helical coil diameter variations, as a larger diameter increases the number of protons injected into the coil but reduces the intensity of the fields inside the coil. I then studied the influence of the length of the helical coil, as a charged particle spending more time in the accelerating field will have an increased energy at the end of the coil. Finally, I studied the impact of progressive pitch helical coils, to synchronise the accelerating fields with the accelerated protons.

In this chapter, I present experimental and simulation results of a parametric study of the coil geometry performed at LULI2000 [40] during the campaign PACMAN 2 in February 2020. The goal of this experiment was to obtain a scaling law from the helix geometry parameters. This work was motivated by the need to optimize future helical coil targets for different applications. This is not a trivial work as the diameter and the pitch of the helix are not independent variables when it comes to calculate the geometrical speed of the current pulse inside the helical coil.

3.1 Experimental set-up of PACMAN 2

The experimental campaign PACMAN 2 was conducted at the LULI2000 facility [40] at Ecole Polytechnique in Palaiseau, France. The laser used for this campaign was PICO2000, which delivered a pulse with a duration $\tau = 1.3$ ps, a wavelength $\lambda = 1.053$ μm and an energy on target $E_0 = (40 \pm 4)$ J.

The laser pulse was focused on the target at normal incidence to a Gaussian spot of 10 μm full-width at half-maximum (FWHM) using an $f/4$ off-axis parabola, providing a peak intensity of the order of 10^{19} W.cm^{-2}. The contrast of the pulses of PICO2000 is characterised as follows: 10^{-10} at 1 ns before the main pulse, increasing to $10^{-6.5}$ between 1 ns and 0.5 ns. It then plateaus at this level until 0.08 ns.

Three different target holders were used during the experiment (see Figure 3.1). The target was a gold (Au) foil of thickness $e = 20$ μm and of width of a few mm. The foil was either supported on a copper (Cu) mast on a dielectric holder made of PEEK (PolyEther Ether Ketone) in the case of regular TNSA shots (Figure 3.1a) or by a helical coil glued

on the backside of the target (Figures 3.1b and 3.1c). Two different holders were used to connect the helical coil (HC) to the ground: the first was an aluminium slab of thickness 1 mm pierced to the size of the helical coil external diameter and in which the coil was inserted (Figure 3.1b). The slab was supported by a dielectric holder made of PEEK. The second holder was a vertical pin directly connected to the ground (Figure 3.1c).

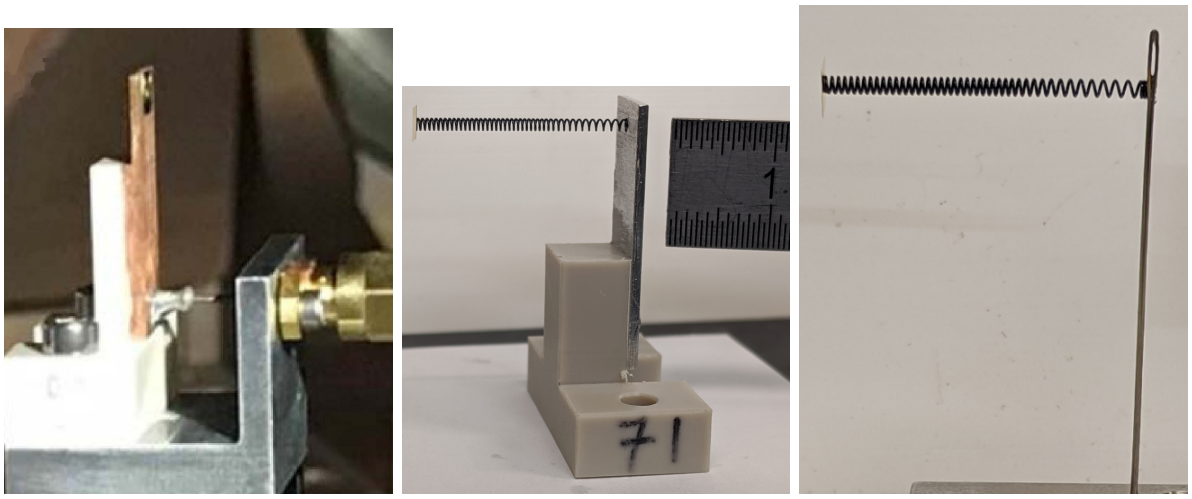

(a) (b) (c)

Figure 3.1 – Different target holders used for the PACMAN 2 campaign: (a) Foil alone, (b) HC with Al slab and (c) HC with pin holder.

During the PACMAN 2 experiment, several geometries of helical coils have been tested. The helical coils are springs manufactured in stainless steel. The HC are all made from 200 μm diameter wire, the HC radius varies from a=0.5 mm to 1 mm, the HC length from L=5 mm to 20 mm and the pitch from h=0.3 mm to 0.95 mm. Some of the coils had progressive pitches or radius along the longitudinal axis.

Finally, there were three diagnostics during the PACMAN 2 experiment:

— A stack of radiochromic films (RCF) located behind the foil target at a distance of 2 to 6 cm. The RCFs are protected by two Al foils of thickness 10 μm located at the front of the stack to stop ions heavier than protons. By measuring the opacity of the irradiated RCFs, we obtain the angular and spectral distribution of the proton beam. The details of the analysis are given in Section 2.1.

— A direct current measurement was made for some shots with and without HC at the end of the target holder.

— A B-dot probe was located at 22.5 cm from the target chamber center to measure the far magnetic field.

This full set-up is shown in Figure 3.2.

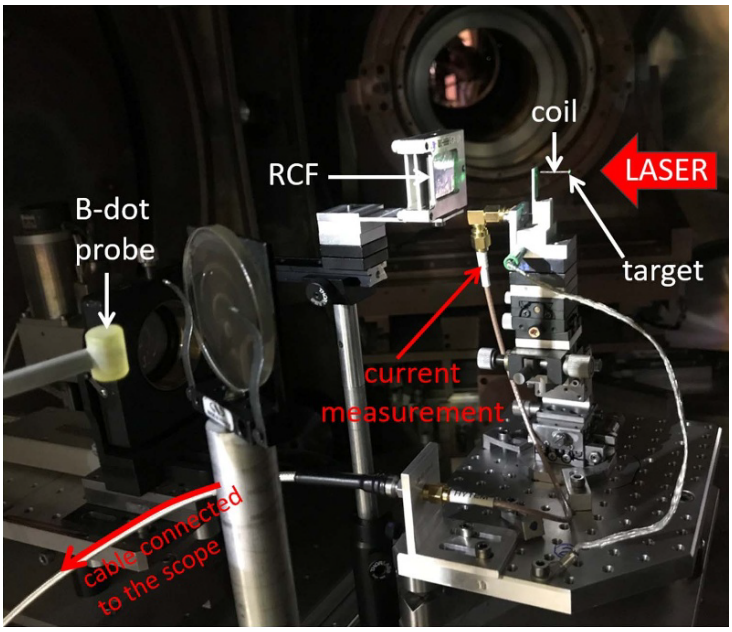

Figure 3.2 – Experimental set-up of the PACMAN 2 campaign.

3.2 Limitations

Before the full analysis of the results of this experiment, I present the two main limitations we observed: the experimental shot-to-shot variation of the TNSA spectrum and the space charge fields that were identified as the main yield limitation factors.

3.2.1 Experimental shot-to-shot variations

To correctly interpret the results that are presented in the following sections, we discuss the cut-off energy of the experimental proton energy spectra. As we see in Figure 3.3, this cut-off is visible on the spectra calculated on the full proton spot, but we don't see a clear drop of charge in the spectra calculated within a 2° opening angle, i.e. the equivalent opening angle of most helical coil targets shot in this campaign, which is the observable used for most of the result analysis.

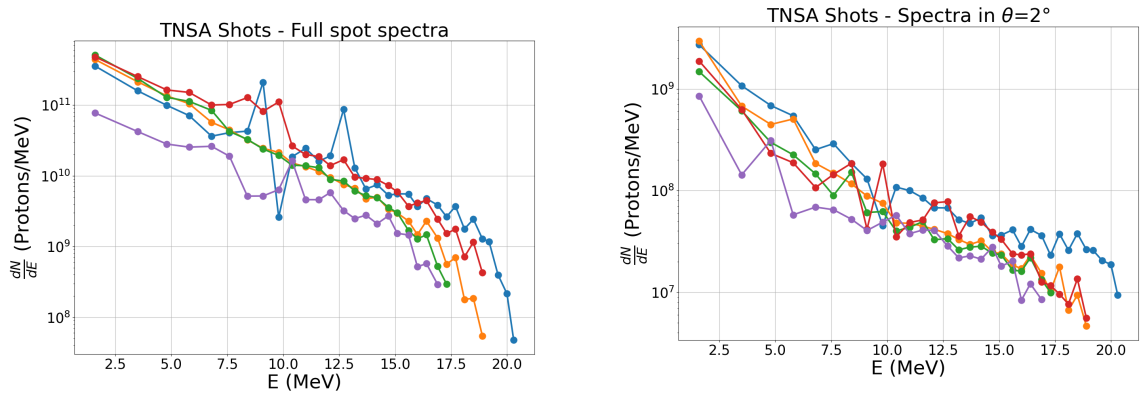

(a)

Figure 3.3 – Experimental TNSA spectrum for: (a) the full proton spot, (b) 2° opening angle.

This is due to the energy dependence of the angular distribution of TNSA protons: the more energetic protons are more collimated than the low energy protons [56], which means that they are more represented in small opening angles, reducing drastically the cut-off drop observed in the spectra.

We also observed shot-to-shot variations for shots made with the same geometry, especially around intermediate proton energies (around 7.5-10 MeV), as shown in Figure 3.4a.

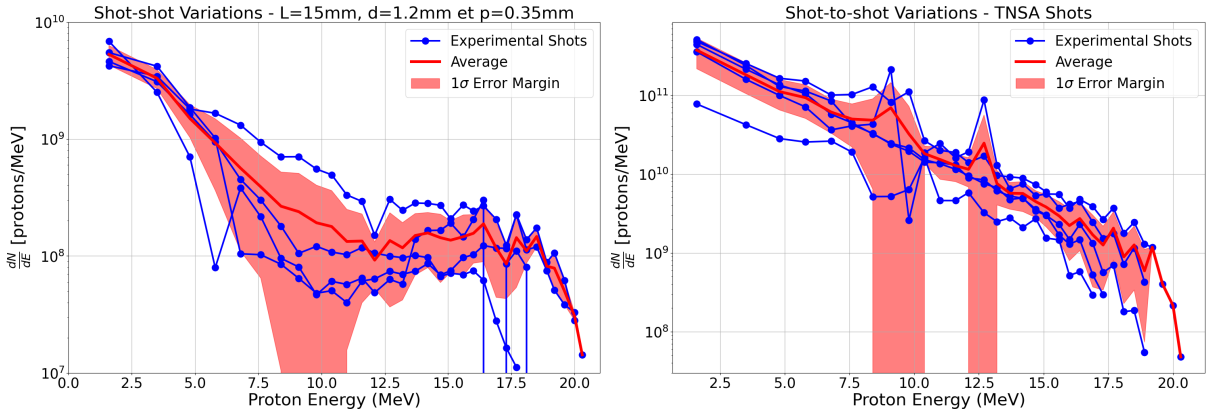

(a) (b)

Figure 3.4 – Shot-to-shot variation of the experimental proton energy spectra for: (a) helical coil targets of length $L = 15$ mm, pitch $p = 0.35$ mm and $d = 1.2$ mm, (b) regular TNSA shots.

By comparing variations observed in the shots with a coil in Figure 3.4a and the TNSA shots in Figure 3.4b, we conclude that the source of the observed variations comes from the TNSA spectra obtained on this facility, for which we don't know the source. The dispersion of results could be reduced by shooting at lower laser energies in order to increase shot-to-shot stability in future campaigns.

3.2.2 Robustness study

These observed experimental shot-to-shot variations led us to perform a robustness study of other experimental parameters than the TNSA variation that could lead to experimental errors. For that, we made a series of PIC simulations using SOPHIE to perform a sensitivity study of the proton spectrum to experimental parameters: the distance between the helical coil and the gold foil due to the glue, the angle between the coil axis and the gold foil, the position of the proton emission zone with respect to the coil axis and the shot-to-shot laser energy variation.

3.2.2.1 Study of the impact of the foil-coil distance

The first experimental parameter we studied via simulation was the distance Δz between the gold foil and the helical coil. This experimental error is due to the glue coat used to fix the helical coil to the gold foil, which can create a small gap of a few tens of μm between the target and the conducting helical coil, as show in Figure 3.5.

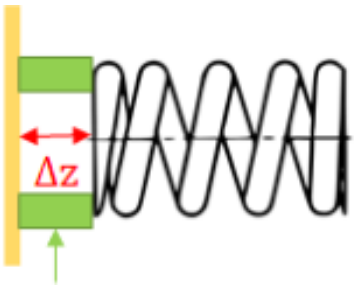

Figure 3.5 – Schematic of the foil-coil distance.

Such a gap could impact the shape and intensity of the discharge current pulse by increasing the impedance mismatch between the foil and the helical coil, reducing the intensity of the electromagnetic fields inside the helical coil.

To take into account this phenomenom, we simulated a set of perfectly conductive coils of length $L = 20$ mm, radius $a = 0.5$ mm and pitch $p = 0.4$ mm and of emissive perfectly conducting foils of size 3x3 mm, with an emissive zone in the center of the foil of radius 100μm. We variated the distance Δz between the foil and the coil from $\Delta z = 0$ μm to $\Delta z = 400$ μm.

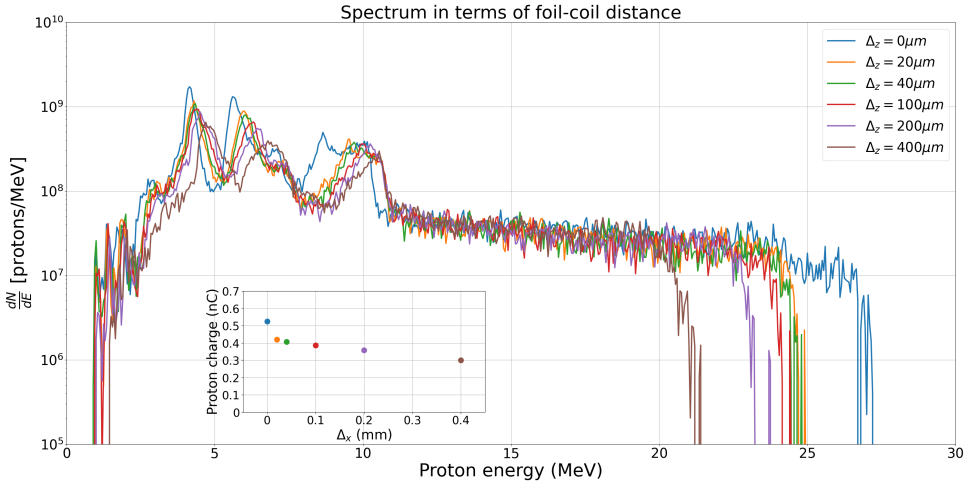

Figure 3.6 – Simulated proton energy spectra at the exit of the helical coil for a coil defined by $L = 20$ mm, radius $a = 0.5$ mm and pitch $p = 0.4$ mm with a variation of the foil-coil distance Δz.

As shown in Figure 3.6, the gap between the foil and the coil has a small impact on the proton beam for Δz below 100 microns whether we look at the structures of the proton beam, the total charge at the exit of the coil (yield is reduced by 20% for $\Delta z = 100$ μm) or the cut off energy (the cut-off energy is only lower by 2.5MeV for $\Delta z = 100$ μm).

We conclude that our experimental results are robust to the experimental variation of Δz as experimentally it is always below $z = 100$ μm.

3.2.2.2 Study of the impact of the foil-coil angle

We studied the effect of the angle between the gold foil and the helical coil θ. Experimentally, this is due to the imperfect planarity of the gold foil and the fact that the end of the HC is not always perfectly perpendicular to the longitudinal axis, which can create an angle up to 10° between the target and the conducting helical coil, as shown schematically in Figure 3.7.

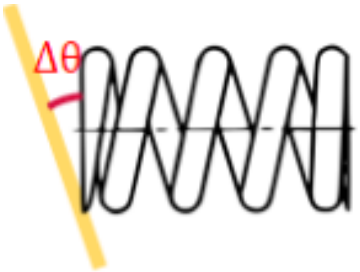

Figure 3.7 – Schematic of the foil-coil angle.

This angle can reduce the yield of the helical coil as less protons leave the target along the coil axis.

To take into account this phenomenom, we simulated a set of perfectly conductive coils of length $L = 20$ mm, radius $a = 0.5$ mm and pitch $p = 0.4$ mm connected to a perfectly conducting foils of size 3x3mm, with an emissive zone in the center of the foil of radius 100μm. We varied the angle θ between the foil and the coil from $\theta = 0°$ to $\theta = 20°$.

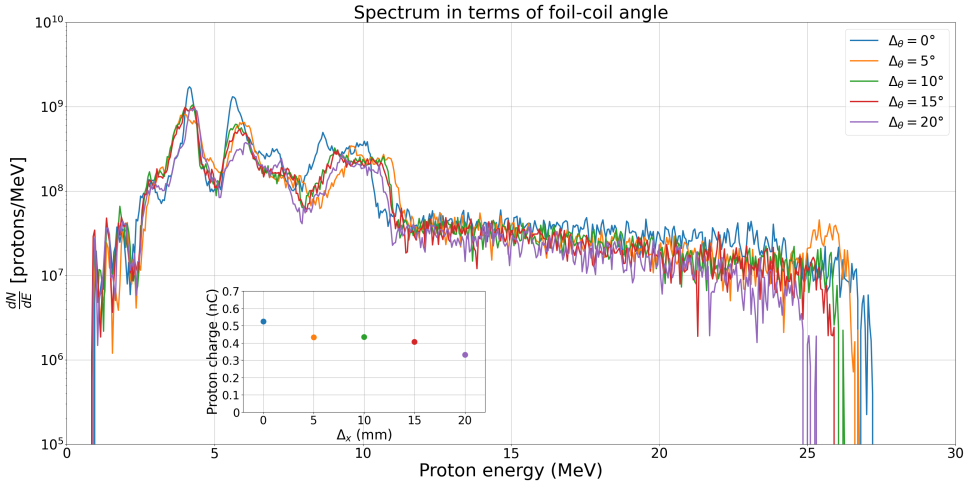

Figure 3.8 – Simulated proton energy spectra at the exit of the helical coil for a coil defined by $L = 20$ mm, radius $a = 0.5$ mm and pitch $p = 0.4$ mm with a variation of the foil-coil angle θ.

As shown in Figure 3.8, the angle between the foil and the coil has virtually no impact on the proton beam for all the observed parameters: spectrum shape, total charge at the exit of the coil and cut-off energy of the proton beam.

We conclude that our set-up is robust to experimental variations of θ.

3.2.2.3 Study of the impact of a pointing error

The third experimental parameter we studied was the deviation Δx of the laser focal spot from the center of the helix, as show in Figure 3.9.

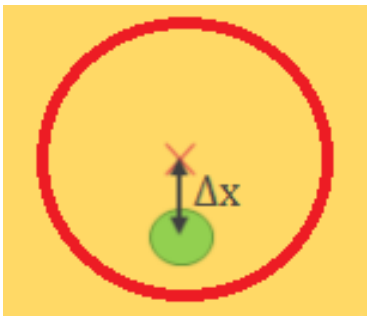

Figure 3.9 – Schematic of the deviation of the focal spot from the center of the helix. The emissive zone is in green, the outline of the helix is in red.

This deviation can reduce the yield of the helical coil target as more protons hit the metallic coil and the cut-off energy as the protons are not emitted on the coil axis where the coil longitudinal fields are the strongest.

To study the effect of this deviation, we simulated a set of perfectly conductive coils of length $L = 20$ mm, radius $a = 0.5$ mm and pitch $p = 0.4$ mm and of emissive perfectly conducting foils of size 3x3mm, with an emissive zone deviated from the center of the foil by a distance Δx. We varied the distance Δx from $\Delta x = 0$ μm to $\Delta x = 400$ μm.

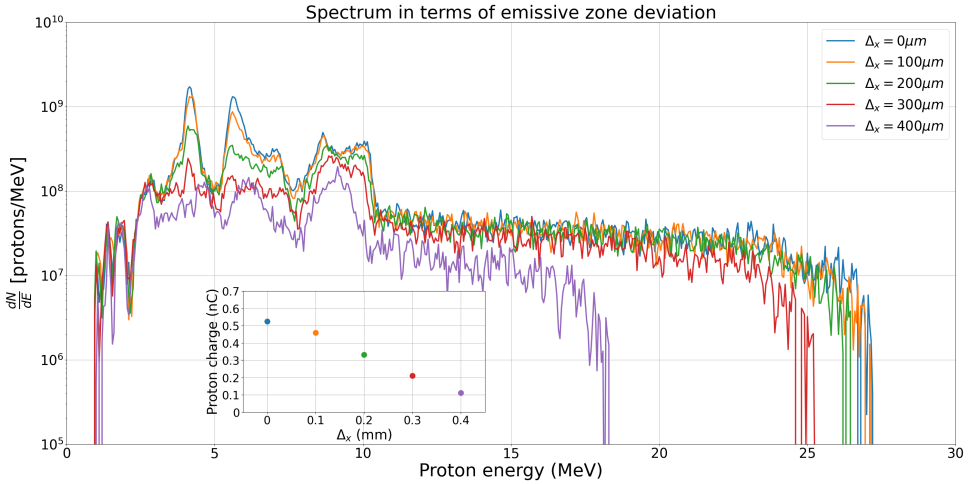

Figure 3.10 – Simulated proton energy spectra at the exit of the helical coil for a coil defined by $L = 20$ mm, radius $a = 0.5$ mm and pitch $p = 0.4$ mm with a deviation of the emissive zone from the center of the foil Δx.

We observe a very limited impact for an emissive zone not touching the inside of the helical coil, i.e. for $\Delta x < 300$ μm, only the yield is impacted. When the emissive zone just touches the inside of the coil, i.e. $\Delta x = 300$ μm, we also observe a strong reduction of the low energy structures and the yield decrease starts to become consequent, a small drop of the cut-off energy. When the centre of the emissive zone is deviated at the level of the inside radius of the coil, i.e. $\Delta x = 400$ μm, we notice a drastic reduction of the yield and the cut-off energy.

In conclusion, as long as our emissive zone is fully inside the internal radius of the helical coil, the experimental results are robust to the variation of Δx.

3.2.2.4 Study of the impact of the laser energy variation

The last experimental variation we studied was the impact of the laser energy variation ΔE_{laser}. Experimentally, PICO2000, the laser used for the PACMAN2 campaign, had its energy variation between 35J and 50J with an average laser energy of $E_0 = 40$ J, i.e. ΔE_{laser} of the order of $\pm 30\%$ E_0.

To study, this variation, we used PIC simulations of perfectly conducting helical coil targets defined by $L = 20$ mm, radius $a = 0.5$ mm and pitch $p = 0.4$ mm and with a variation of the laser energy from $E_{\text{laser}} = 0.7$ E_0 to $E_{\text{laser}} = 1.3$ E_0 by changing appropriately the protons and electrons cut-off energy with $E_{\text{cut-off}} \propto E_{\text{laser}}^{3/2}$ [77] and the total charge of the proton and electron beam with $Q \propto E_{\text{laser}}$.

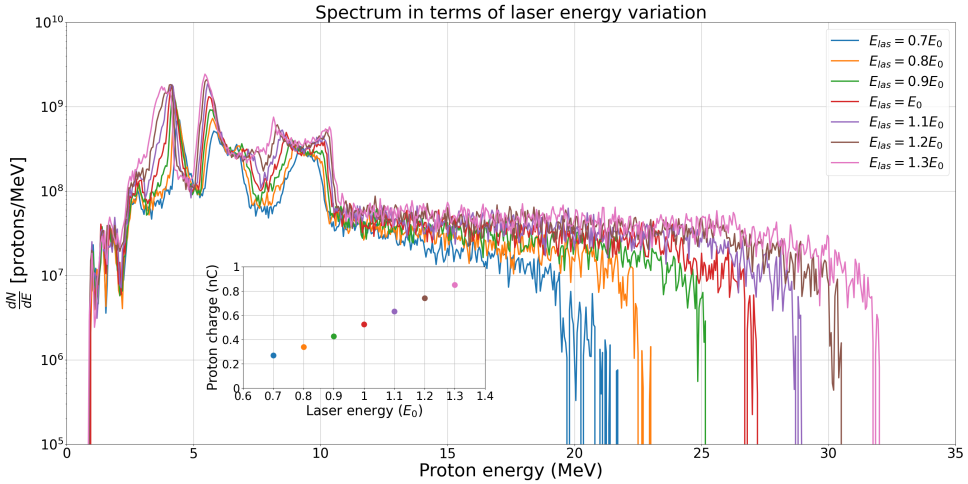

Figure 3.11 – Simulated proton energy spectra at the exit of the helical coil for a coil defined by $L = 20$ mm, radius $a = 0.5$ mm and pitch $p = 0.4$ mm with a variation of the laser energy ΔE_{laser} around $E_0 = 40$ J.

We notice that the variation of E_{las} has a strong impact on the spectrum, with the total charge increasing linearly with E_{las} and the cut-off energy increasing with a sub-linear law, as the high-energy protons see the accelerating time for less time. We also notice a similar spectrum shape for $E < 10$ MeV.

This leads us to conclude that the laser energy variation has a strong impact on the high energy protons, especially the cut-off energy. It is a secondary source of the shot-to-shot variation after the TNSA itself.

3.3 Parametric study of the variation of the helical coil diameter

3.3.1 Helical coil with constant diameter

The first parametric study I present is on the helical coil diameter and its impact on the total charge of the beam exiting the target. The motivation behind this study was to see whether we could identify an optimum coil diameter for the coil yield. Two conflicting phenomena are observed: the number of protons injected in the coil increases with the diameter and the amplitude of the electromagnetic fields inside the helix decreases with the diameter.

3.3.1.1 Experimental study

For that study, four shots were performed at constant parameters (pitch $p = 0.4$ mm and $L = 16$ mm) with the coil diameter varying from 1 to 1.6mm.

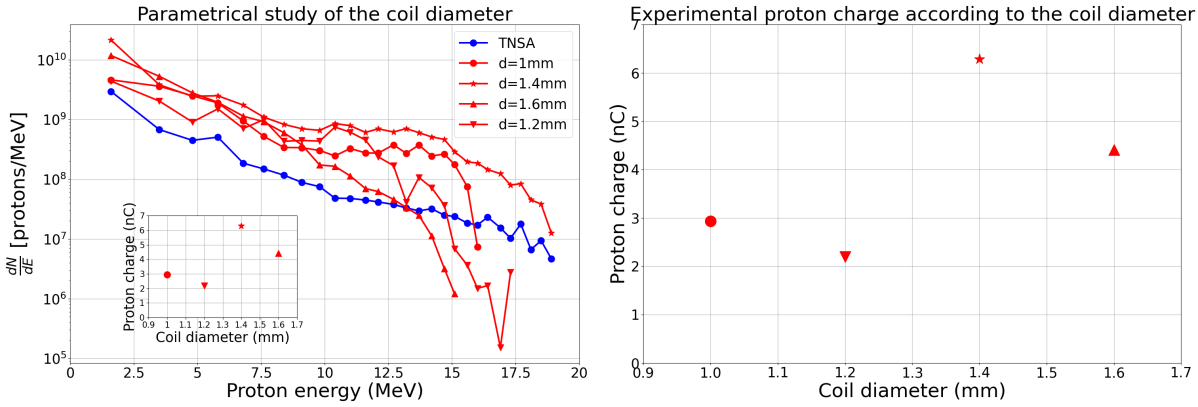

(a) (b)

Figure 3.12 – Experimental (a) proton energy spectra and (b) charge of the proton beam in 2° opening angle for the parametric study of the coil diameter for $L = 16$ mm and $p = 0.4$ mm.

We observe in Figure 3.12a spectra of similar shapes for the 4 shots, characterised by a strong focus compared to the TNSA shot. We also notice in Figure 3.12b a variation of the total charge of the proton beam in a 2° opening angle. There is a maximum in the case d=1.4 mm, which implies the presence of a compromise to find between the proton injection in the helical coil and the amplitude of the electromagnetic fields inside the coil, which increase as the coil diameter decreases. But the lack of statistics in the experimental results lead us to analyse the results with PIC simulations.

3.3.1.2 PIC simulation study

We then simulated the experiment with the code SOPHIE, that was successfully used in the PACMAN 1 experiment [39]. For that we modeled four perfectly conducting helical coils of length $L = 16$ mm and pitch $p = 0.4$ mm with a variation of external diameter going from $d = 1$ mm to $d = 1.6$ mm as in the experiment. They are all connected on one end to a perfectly conducting emissive foil of thickness $e = 20$ μm and width $w = 3 \times 3$ mm with an emissive spot of radius $r = 100$ μm and on the other end to a metallic stick of thickness $e = 1$ mm and width $w = 5 \times 5$ mm, pierced at the connection with the helical coil.

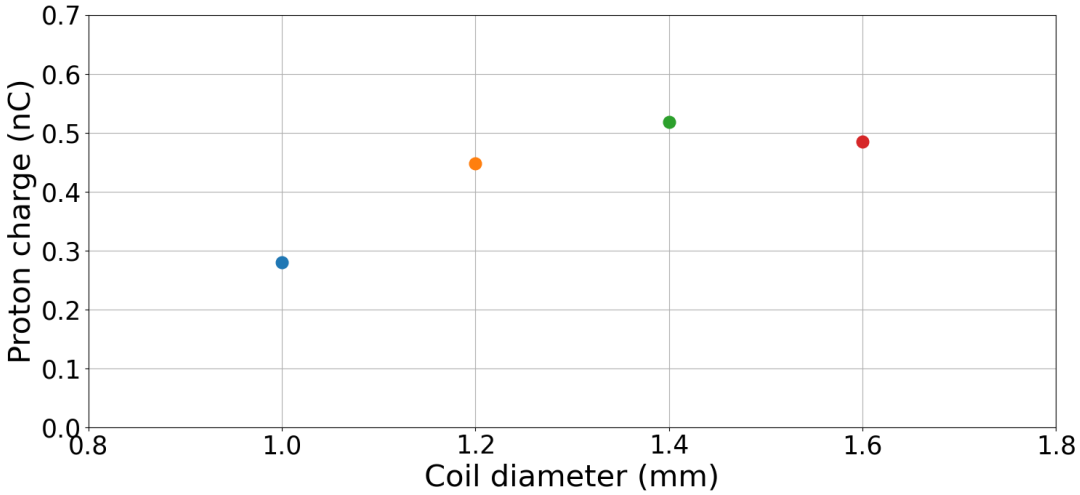

Figure 3.13 – SOPHIE simulated charge of the proton beam in a 2° opening angle for the parametric study of the coil diameter for $L = 16$ mm and $p = 0.4$ mm.

We observe in Figure 3.13 on the simulated results a qualitative agreement with experimental results observed in Figure 3.12b as for the optimal diameter for proton injection.

There is therefore a need for an optimisation study to find the optimal diameter for proton injection using more PIC simulations or a dedicated numerical model of helical coil. This optimization will be specific to each laser installation, due to the evident influence of the TNSA and current source terms.

3.3.2 Helical coil with varying diameter

We also conducted a parametric study on helical coils with progressive diameters and their impact on the total charge of the beam exiting the helix. The motivation was to hopefully observe an increase of charge with a funnel like helix, allowing a larger injected proton charge with the bigger diameter at the entrance of the coil and stronger electromagnetic fields as the diameter decreases along the longitudinal axis. Such a coil is shown in Figure 3.14.

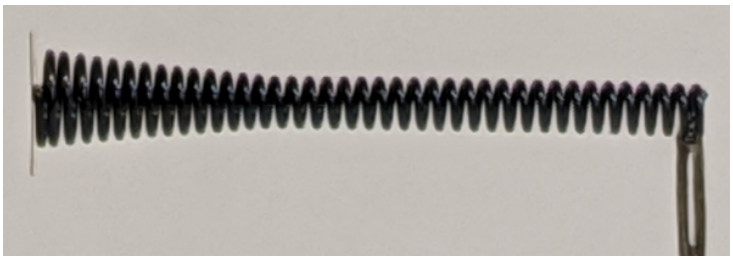

Figure 3.14 – Funnel-like helical coil on a pin holder.

3.3.2.1 Experimental study

For this parametric variation, all studied targets have the same length $L = 20$ mm, pitch $p = 0.35$ mm and final diameter $d = 1.2$ mm. The diameter at $z = 0$ mm is either 1.7 mm or 2.2 mm and linearly decreases to 1.2 mm on the first 3, 5 or 8 mm.

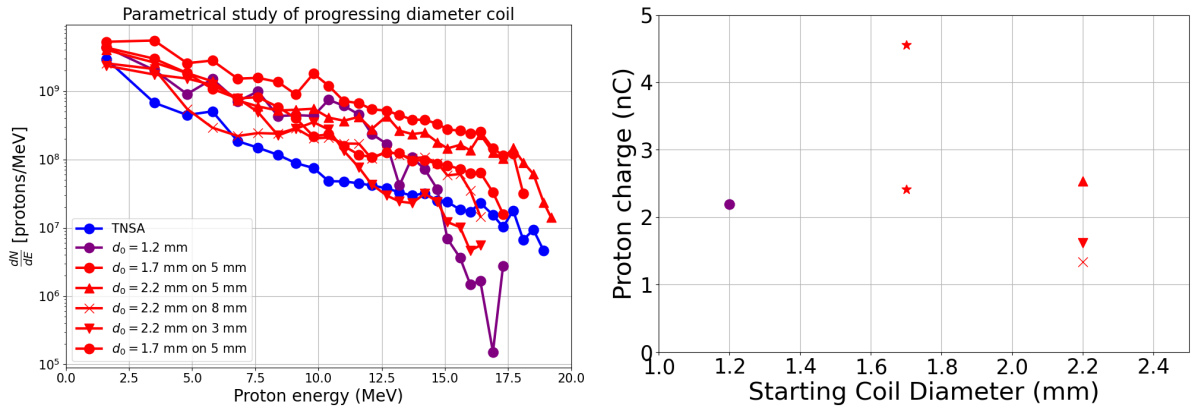

(a) (b)

Figure 3.15 – Experimental (a) proton energy spectra and (b) total charge of the proton beam in a 2° opening angle for the parametrical study of varying-then-constant diameter coils for $L = 20$ mm, $p = 0.4$ mm and $d_{final} = 1.2$ mm. In purple is a coil of constant diameter $d = 1.2$ mm, $L = 20$ mm and $p = 0.4$ mm.

We cannot observe experimentally the impact of such coils on the beam charge in 2° opening angle. We expected an increase in total charge with the increase of the initial opening as the coils could impact a larger number of protons, but this was not confirmed by experiment: the total charge of the protons beam is around the same level as most HC targets with constant diameter and pitch.

This idea will be further explored with the use of DoPPLIGHT and via an optimisation process on the size and shape of this funnel.

3.4 Parametric study of the variation of the helical coil length

The second parametric study is on the impact of the coil length on the cut-off energy of the proton spectra at the exit of the HC. The idea was to observe an increase of the cut-off energy with the length of the coil as the longer time the protons spend in an accelerating field, the higher their energy will be.

3.4.1 Experimental study

For this study, 5 different targets are used, they all have the same pitch $p = 0.4$ mm and diameter $d = 1.2$ mm and the different lengths studied were 5 mm, 8 mm, 12 mm, 16 mm and 20 mm.

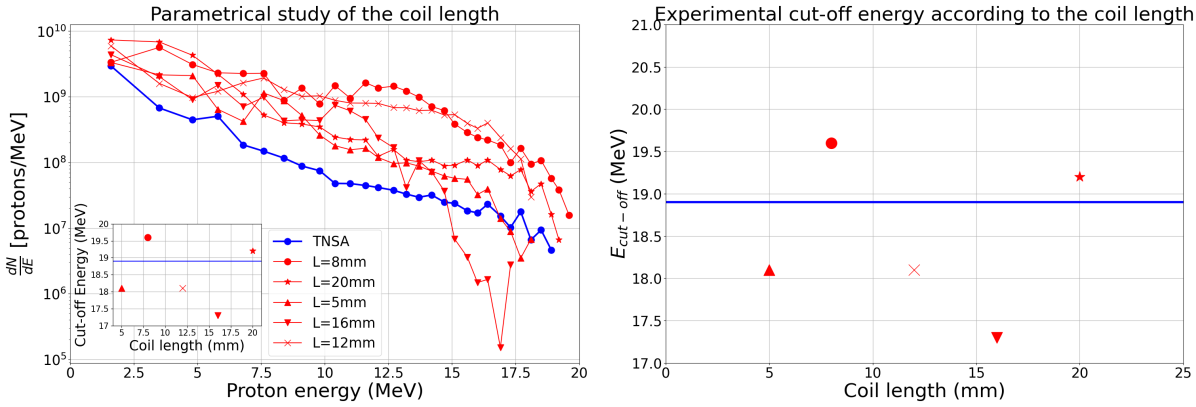

(a) (b)

Figure 3.16 – Experimental (a) proton energy spectra and (b) cut-off energy of a regular TNSA shots (blue line) and proton beam in a 2° opening angle for the parametrical study of the coil length for $p = 0.4$ mm and $d = 1.2$ mm (red dots).

We observe in Figure 3.16 that the cut-off energy seems to vary around the TNSA cut-off energy at 19 MeV, which implies an alternance of accelerating and decelerating fields seen by the proton population along the longitudinal axis reducing strongly the impact of the helical coil on the proton cut-off energy. As previously, the lack of experimental statistics lead us to a numerical study via DoPPLIGHT to confirm these results.

3.4.2 DOPPLIGHT and PIC study

To analyse these results, we studied the variation of cut-off energy of a TNSA beam defined by a cut-off energy of 19 MeV and a proton temperature of 3 MeV, i.e. equivalent to a Maxwellian fit of the experimental TNSA spectrum, through a coil of pitch p=0.4 mm and diameter d=1.2 mm via the theoretical model DOPPLIGHT.

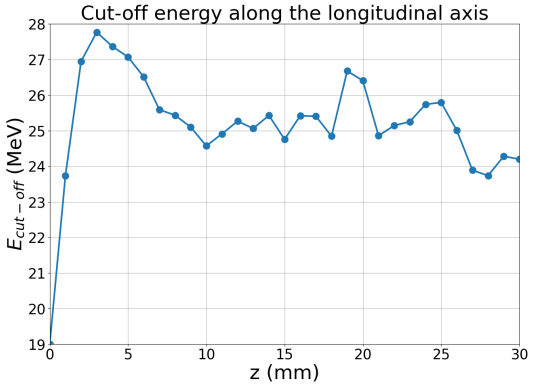

Figure 3.17 – Dependence of the cut-off energy on the length a coil of pitch p=0.4 mm and diameter d=1.2 mm, for a TNSA beam defined by $E_{cut-off} = 19$ MeV and $T_{protons} = 3$ MeV obtained using the DOPPLIGHT model.

We observe in this graph a variation of the cut-off energy of a few MeV along the longitudinal axis, consistent with the experimental results. The fact that the variation is above and not around the TNSA cut-off energy is due to the fact, contrary to the

experimental spectrum, that there is no limitation of the maximum cut-off energy observed as is the case with the RCF diagnostic.

This variation is due to the dispersion of the discharge current in the HC, which is the cause of regular sign inversion and spreading of the current. The helix has an impedance depending on the frequency, as shown in the works on conducting helices since the 1950s [80], [81]. The discharge current created by a TNSA shot is by nature short and spectrally very broad. By combining the dispersive nature of the HC and the broadband current, there is a strong current dispersion that we observe in DoPPLIGHT and PIC simulations shown in Figure 3.18, which limits the maximum energy gain unless we can find a new scheme controlling the current dispersion.

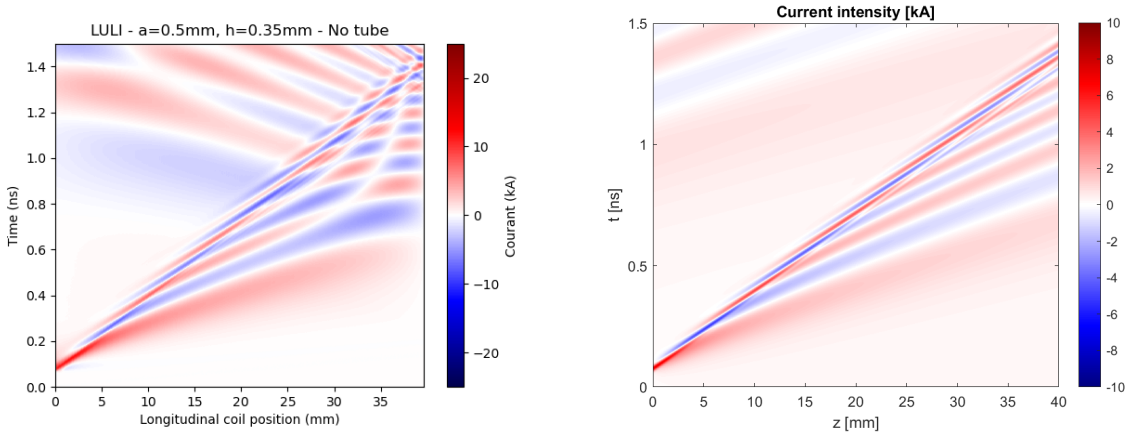

(a) (b)

Figure 3.18 – (a) PIC simulation (b) DoPPLIGHT calculation: of the current pulse intensity in kA as a function of time and along the HC axis. For a theoretical TNSA beam defined by $E_{cut-off} = 19$ MeV and $T_{protons} = 3$ MeV. The HC parameters are: length $L = 40$ mm, radius in the heart of the coil $a = 0.5$ mm, external radius=0.6 mm and pitch $h = 0.35$ mm.

The dispersion of the current pulse is characterised by an alternating positive and negative current pulse along the geometrical speed of the helical coil, which is consistent with the experimental results showing a variation of the cut-off energy around the TNSA cut-off energy. The differences between the two graphs are due to the fact that DoPPLIGHT does not take into account the current reflection at the end of the helix, contrary to SOPHIE.

These results are also consistent with the simulation study by Liu *et al.* [96], which show that the cut-off energy of protons accelerated by a single-stage HC varies around the TNSA cut-off energy as the coil length increases.

3.5 Parametric study of the variation of the helical coil pitch

We studied the impact of varying pitch on the cut-off energy. The motivation behind that study was to synchronise the current pulse with the accelerated protons. Indeed, once the proton are accelerated, they move faster than the current pulse and leave the accelerating fields. By increasing progressively the helical coil's pitch, the propagation speed

of the electromagnetic pulse increases, matching with the propagation of the accelerated protons.

3.5.1 Parametric study of progressively varying pitch helical coils

The first study was the observation of shots with coils with the pitch increasing from the origin to the end of the coil. The expectation for such a variation of the HCs was to observe a shift of the low energy bunches towards higher energies as the pulse accelerates along the propagation axis with the variation of the pitch.

3.5.1.1 Experimental study

The experimentally studied coils are all of the same length $L = 20$ mm, same diameter $d = 1.2$ mm and same pitch $p_0 = 0.35$ mm at $z = 0$ mm. Their pitch at $z = 20$ mm goes from $p_{\text{end}} = 0.5$ mm to $p_{\text{end}} = 0.75$ mm.

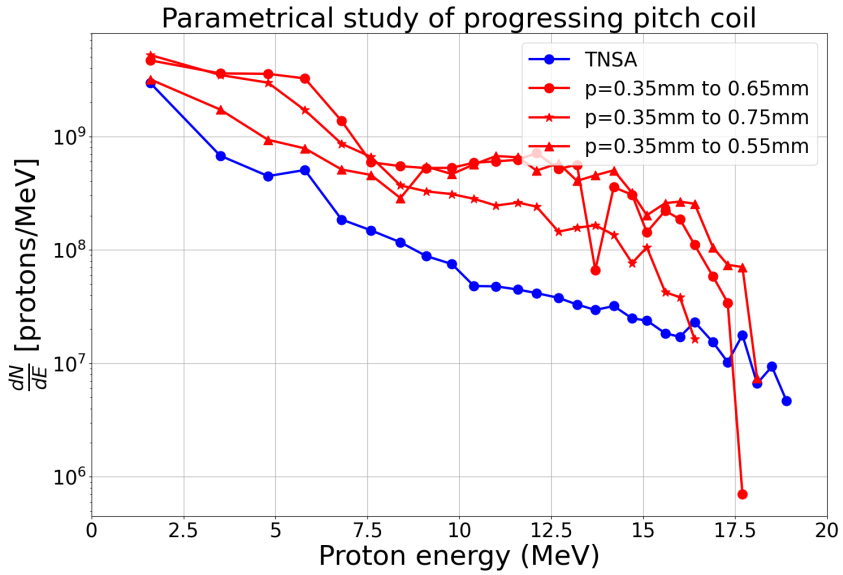

Figure 3.19 – Experimental proton energy spectra of the proton beam in a 2° opening angle for the parametrical study of helical coils with progressive pitch with $L = 20$ mm, $d = 1.2$ mm and $p_0 = 0.35$ mm.

In Figure 3.19, the effect of pitch variation on the low energy structures observed on PIC simulations is not visible on the experimental spectra due the lack of resolution of the first RCFs of the stack, corresponding to the lowest energies. The gap between the characteristic energies of two consecutive films under 10 MeV is at least 0.7 MeV and goes up to 2 MeV for the first two.

We did not observe in the experiment any effect of the helical coil with progressive pitch on the TNSA spectrum. A finer spectrum diagnostic, such as a Thompson parabola, would enable us to see the finer structures of the proton spectrum.

3.5.1.2 PIC simulation study

To see what physical effects we could expect with more precise and sensitive diagnostics for further campaigns, we simulated via SOPHIE the same helical coils with progressively

increasing pitch.

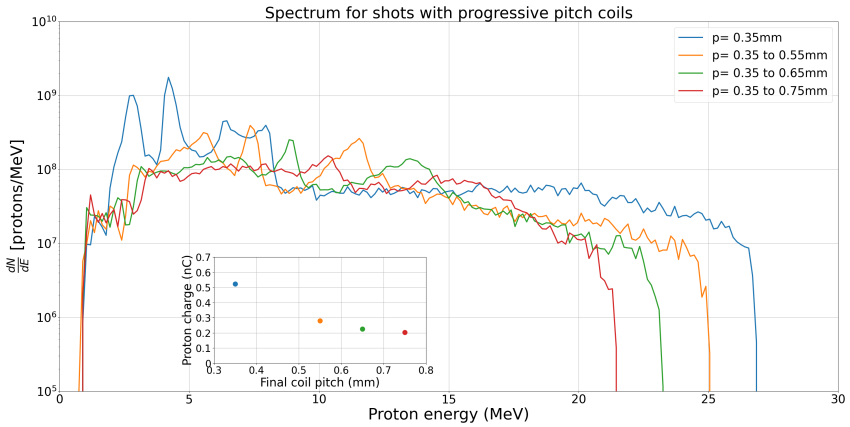

Figure 3.20 – PIC Simulated proton energy spectra of the proton beam in a 2° opening angle for the parametrical study of helical coils with progressive pitch with $L = 20$ mm, $d = 1.2$ mm and $p_0 = 0.35$ mm.

We observe in Figure 3.20 a reduction of the cut-off energy on increasing the final pitch and a shift of the low energy bunches towards higher energies. These bunches become less distinct as the final pitch increases. We notice a decrease of the charge inside the beam as the final pitch increases since the protons spend more time in the HC fields, where they see more defocusing and accelerating fields as they are matched for a longer time with the maximum intensity of the current, shifting the structures of the spectrum.

3.5.2 Parametric study of a two-step helical coil

With PACMAN 2 we studied coils with a constant pitch close to the TNSA foil and then a varying pitch towards the exit. The first part of the HC with a constant pitch forms the bunches as observed in the experiments presented in the previous sections. The expected impact of the varying pitch part of the HC is two-fold: first, a shift of low energy bunches towards higher energies and second, an increase of the gap between the bunches observed in PIC simulations.

3.5.2.1 Experimental study

The helical coils used have the same length $L = 20$ mm, the same diameter $d = 1.2$ mm and the same pitch $p = 0.35$ mm between $z = 0$ mm and $z = 12$ mm. Over the last 8 mm of the coil, the pitch increases linearly towards a final pitch of 0.55 mm to 0.95 mm, depending on the target.

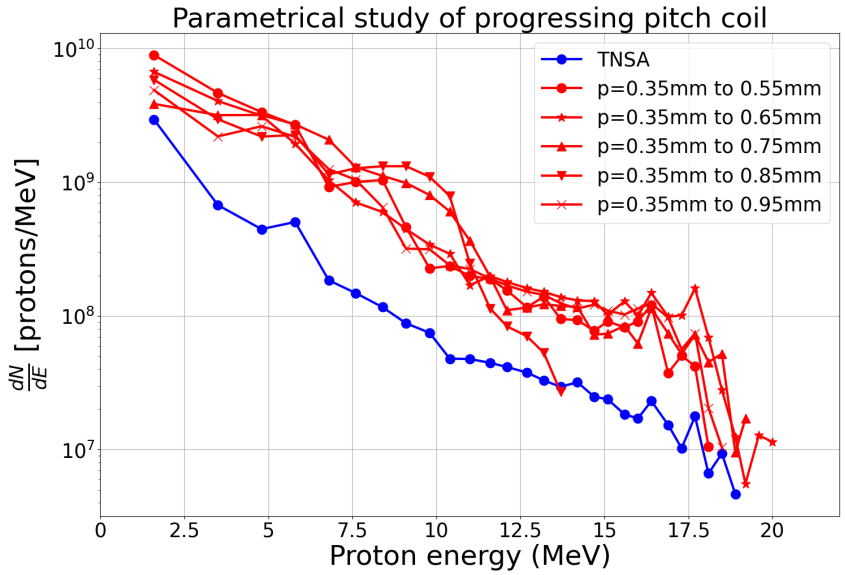

Figure 3.21 – Experimental proton energy spectra of the proton beam in a 2° opening angle for the parametrical study of helical coils with constant then progressive pitch with $L = 20$ mm, $d = 1.2$ mm and $p_0 = 0.35$ mm constant on the first 8 mm.

However, the low energy bunches are not visible on the experimental spectra due to the lack of resolution of the first few RCFs and we cannot see the effects of such coils on the TNSA experimental spectrum.

3.5.2.2 PIC simulation study

As in the previous case, we studied via PIC simulations the experimental targets to see whether a campaign with a finer diagnostic such as a Thompson parabola could be of interest.

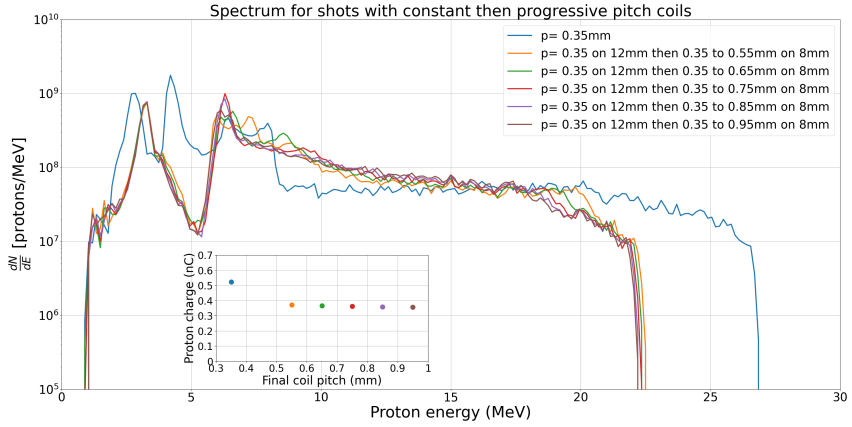

Figure 3.22 – PIC simulated proton energy spectra of the proton beam in a 2° opening angle for the parametrical study of helical coils with constant then progressive pitch with $L = 20$ mm, $d = 1.2$mm and $p_0 = 0.35$ mm constant on the first 8 mm.

As shown in Figure 3.22, the impact of such helical coils is mostly negative compared to helical coils with a constant pitch as we observe a drop in cut-off energy. While the final pitch does not have an impact on the bunches positions, the helical coils with constant

then progressive pitch show that the low energy bunches are more clearly defined than with basic coils.

3.6 Space charge impact on the TNSA beam

This experimental campaign also indicates the origin of the low yield of this acceleration scheme, where the maximum yield is of the order of 15% for a long coil. While experiments, PIC simulations and DoPPLIGHT show focusing effects stronger than the simple geometric filter of a cylinder the size of the helical coil, one needs to understand the reason of the loss of charge to be able to improve the yield of helical targets for applications requiring a high proton charge.

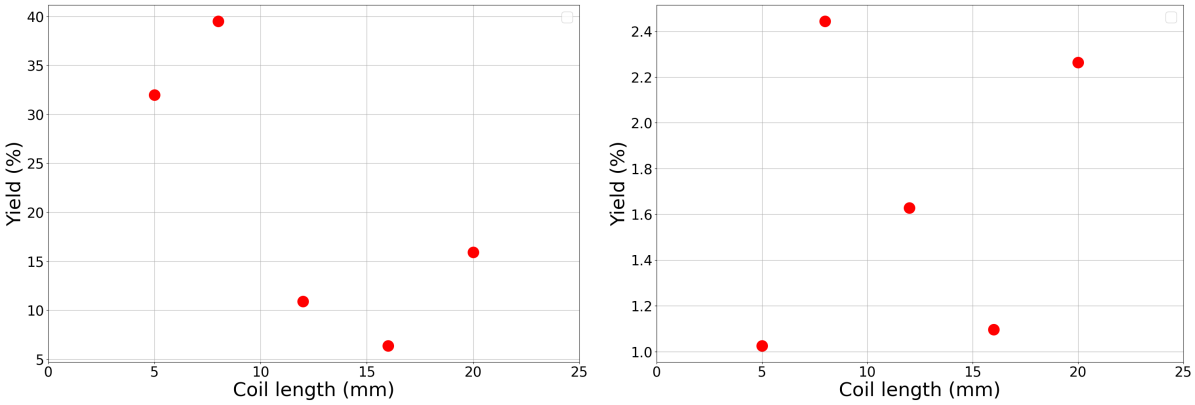

(a) (b)

Figure 3.23 – Experimental proton charge yield depending on the length for a helical coil of pitch $p = 0.4$ mm and diameter $d = 1.2$ mm for: (a) the full beam at the exit of the coil (b) the beam in a 2° opening angle.

We observe in Figure 3.23 the impact of the TNSA angular distribution on the total charge at the exit of the coil. Within a small opening angle of 2°, we observe the high energy protons, propagating perpendicularly to the target. They have a relatively low density and are less impacted by the space charge. The full spot at the exit of the coil shows a more significant drop in charge after propagating over a distance of 8-10 mm. This is explained by a Coulomb repulsion of the higher density low energy protons, which are emitted with larger divergence from the TNSA target.

To increase the yield, we tried to understand what is the main process of charge loss in the helical coil. For that, we ran PIC simulations where the biggest losses of charge occured in the first few millimeters, see Figure 3.24b. At times of around $t = 100$ ps, we observe a strong defocusing radial electric field E_r. Trying to understand its sources, we ran PIC simulations with and without protons and we obtained the radial field E_r at $t = 100$ ps shown in Figure 3.24a.

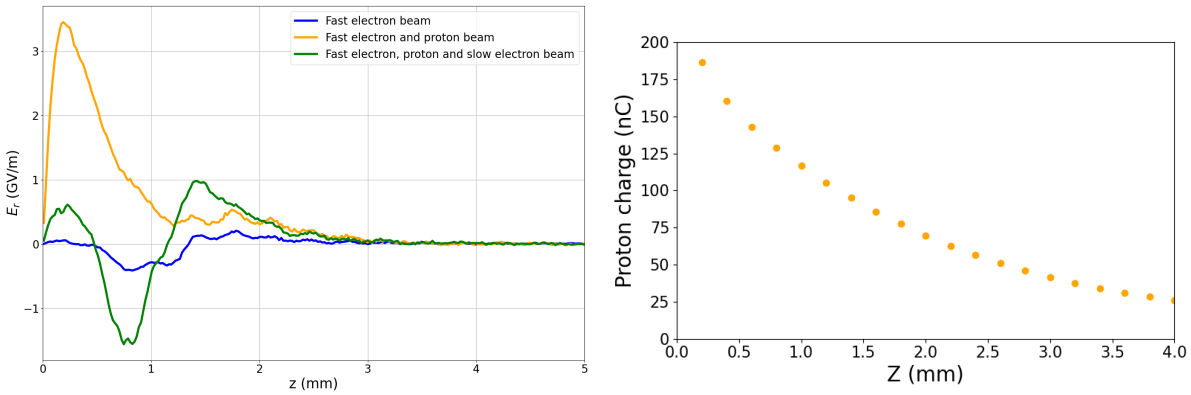

(a) (b)

Figure 3.24 – (a) PIC simulated radial field E_r as a function of the longitudinal axis at $r = 0.2$ mm and $t = 100$ ps for a spectrum of fast electrons only (blue), a spectrum of fast electrons and a deneutralised TNSA beam (orange) and a spectrum of fast electrons and neutralised TNSA beam (green). (b) PIC simulated charge in a 1mm radius at different longitudinal positions for a positively charged TNSA beam.

The difference between the three cases in Figure 3.24a allows us to conclude that space charge has a strong impact on the proton beam, with a field strongly defocusing protons at the front and the back of the beam and strongly defocusing slow electrons in the middle of the beam, thus positively charging the TNSA beam. Figure 3.24a shows that, at early times, the space charge field is the dominant radial field, compared to the helix field in blue, defocusing the back end of the proton beam where most of the proton charge is located.

3.7 Conclusion and perspectives

In this chapter, I showed the effects of the helical coil's geometry on the TNSA beam, in particular the existence of a fluence maximum at an optimal coil diameter, seen both experimentally and on large-scale PIC simulations.

I also showed the experimental limitations of the PACMAN2 campaign: the shot-to-shot variations observed on identical coils, due to the shot-to-shot variations of the TNSA process on LULI2000, as well as the lack of resolution of RCFs limiting the analysis.

Finally, the two main limitations observed during this study are: the presence of a strong defocusing space charge field at early times, limiting the yield of HCs and the dispersive nature of the helical coil creating an alternance of accelerating and decelerating fields, limiting the cut-off energy of the proton spectrum.

To study the helical coil targets and their impact on a TNSA proton beam, we developed and implemented a proton space charge model in DoPPLIGHT, based on the effects identified from the experimental results and our PIC simulation study. This is presented in the next chapter.

Chapter 4

Space charge modelling for a proton beam in a helical coil target

The objective of this chapter is to model space charge effects produced by the proton beam inside a helical coil target observed in chapter 3. The goal is to implement the effect of proton repulsion in the theoretical model DoPPLIGHT without increasing the model complexity, to keep the time gain compared to large-scale PIC simulations. I first characterised the shape of the TNSA proton beam, to adapt the model to the physical parameters of our beam. I then developed a 3D theory of the space charge of a non-relativistic Gaussian proton bunch. Finally, this theory was implemented in DoPPLIGHT, a time-resolved and non self-consistent theoretical model of the proton beam propagation through a helical coil.

In this chapter, I present the work made on the characterisation and EM modeling of the TNSA proton beam observed in the previous chapter. This space charge field is one of the reason for the low proton yield of helical coil targets, as presented in Chapter 3. The motivation behind this work was to have a space charge model in our theroretical code DoPPLIGHT giving results close to the large-scale PIC simulations to use this code for future designs of helical coil targets.

4.1 Predominance of the space charge fields

As explained in Section 3.6, we discovered the impact of space charge on the charge at the exit of the coil by observing the presence of strong defocusing fields at early times.

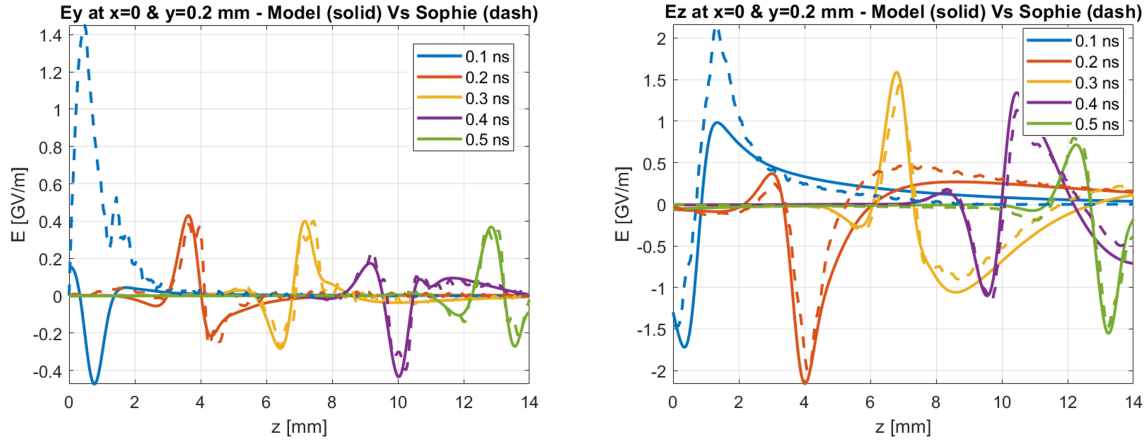

(a) (b)

Figure 4.1 – (a) Radial and (b) longitudinal electric fields at different times. The dashed lines correspond to full-scale SOPHIE simulations and the full line to the theoritical helical coils fields. The HC parameters are: length $L = 15$ mm, radius in the heart of the coil $a = 0.5$ mm, external radius=0.6 mm and step $h = 0.35$ mm. The particles features are defined in Table 2.2 for LULI.

As seen in Figure 4.1, there is a strong mismatch at early times between the helical coil fields calculated in DoPPLIGHT and the PIC simulated fields which include helical coil and beam generated fields. This difference is due to the space charge fields of the protons, predominant at early times, by a factor of around 5 for the radial fields compared to the regular helical coil fields.

A possibility to compensate these space charge fields would be to apply a strong constant magnetic field that enables us to focus the proton beam inside the helix. Let r_{L} be the Larmor radius, E the proton energy, m the proton mass and q the proton charge. If we suppose our protons to be non-relativistic and so $E = mv^2/2$, the magnetic field B necessary to compensate the space charge field is

$$B = \frac{\sqrt{2Em}}{qr_L}. \tag{4.1.1}$$

In the case of our protons, for $r_{\mathrm{L}} = 0.4$ mm the radius of the helical coil and $E = 20$ MeV the energy of the most energetic protons, we have

$$B \approx 1.2 \text{ kT}.$$

Such a strong field cannot be produced with our experimental set-up, therefore, we cannot use it to compensate the space charge fields. The strongest fields that can be created with the available current of a few kA are of the order of 20-50 T and would contain the protons in a radius of tens of cm, much larger than our coil radius.

Another common method in classical accelerators to compensate the space charge is the use of a residual gas that neutralises the beam as it is ionized by the protons traversing it [97], but that cannot be used in our setting either as the ionized gas would short-circuit the helical coil.

As we cannot compensate this divergent fields, we have to be able to model it, but before this, we need to characterize the distribution of our proton beam.

4.2 Characterization of the proton beam shape

In this section, we study the shape of the TNSA proton beam in order to calculate the theoretical space charge fields of the TNSA proton beam with our theoretical model DoPPLIGHT. To characterise the proton beam, we made a simulation of the TNSA beam emitted from a metal foil connected to a mass and propagating in the vacuum with particle diagnostic at several intervals of length and several radii. This enables us to observe the charge distribution as a function of r and z.

4.2.1 Shape of the beam in the radial direction

To model the beam in DoPPLIGHT, we study its radial and longitudinal distribution with a 2D axi-symmetric code.

We first studied the shape of the beam in the radial direction, at different longitudinal positions along the propagation axis at the time of the maximum of the charge flux. We approximated it with a Gaussian fit, characterised by the surfacic charge distribution

$$\rho_r(r) = \frac{Q_r}{2\pi\sigma_r^2} e^{-(r^2/(2\sigma_r^2))} \tag{4.2.1}$$

where Q_r is the surfacic charge of the beam and σ_r the characteristic size of the beam in the radial direction.

We fitted this distribution to the propagating TNSA beam and we obtained the comparison plotted in Figure 4.2.

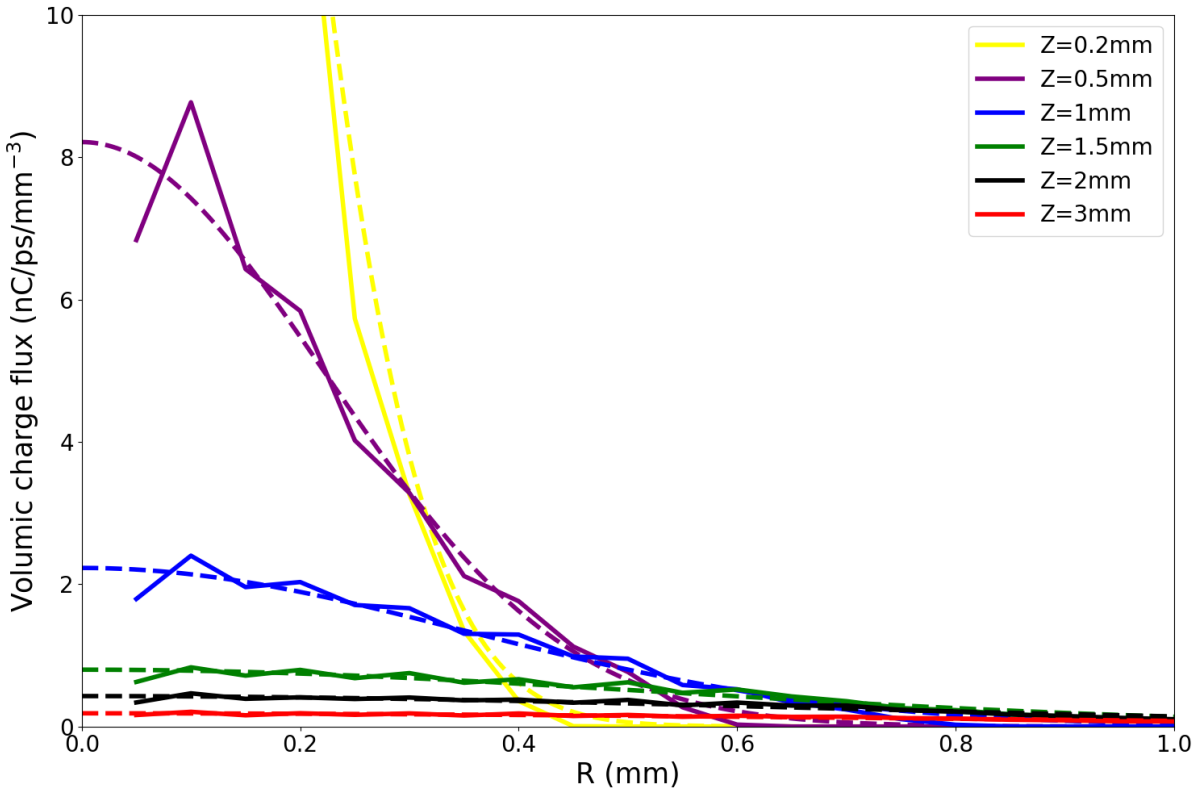

Figure 4.2 – Volumic charge flux of the TNSA beam as a function of r at different longitudinal positions. Each fit is made at the time of the maximum flux in the position z. PIC simulations results are in full lines and the Gaussian fit in dashed lines.

We observe a good agreement between the PIC simulation and the Gaussian fit, validating the Gaussian shape of the TNSA beam in the radial direction.

We also studied the evolution of the beam along the longitudinal axis by examining the evolution of σ_r along the longitudinal axis, i.e. the divergence:

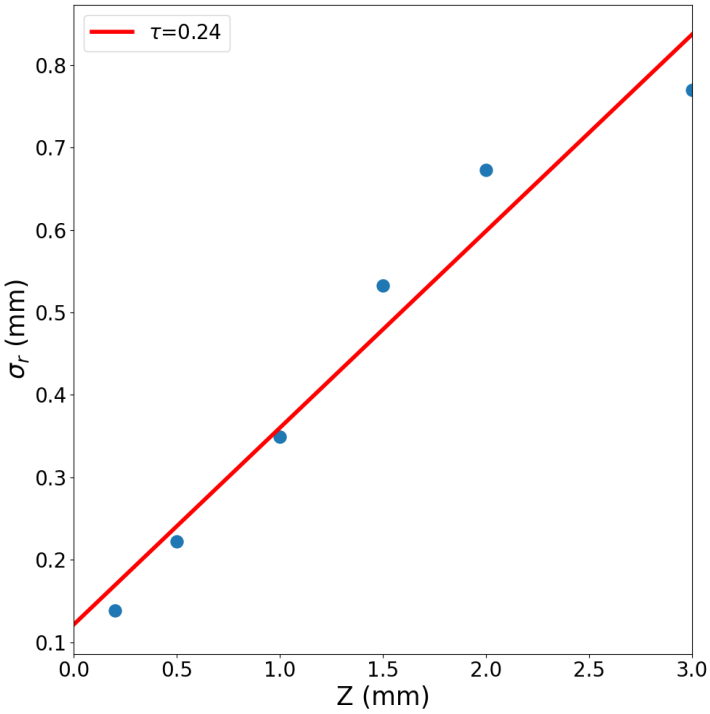

Figure 4.3 – Evolution of σ_r as a function of the longitudinal position and linear fit in red with a slope τ.

We observe that under the influence of its own space charge, the proton beam expands radially with an almost constant rate $d\sigma_r/dz = 0.24$.

4.2.2 Shape of the beam in the longitudinal direction

Now that we have the shape of the proton beam in r, we want to obtain the shape of the proton beam in the longitudinal direction.

4.2.2.1 Gaussian fit

We first tried to fit the proton beam in the longitudinal direction by a Gaussian fit too, following the following charge distribution:

$$\rho_z(z_{beam}) = \frac{Q_z}{(2\pi)^{1/2}\sigma_z} e^{-(z_{\text{beam}}^2/2\sigma_z^2)} \tag{4.2.2}$$

with σ_z the characteristic size of the beam in the longitudinal direction, $z_{\text{beam}} = z - \bar{z}$ and $\bar{z}$ the average position of the proton beam.

By fitting a Gaussian curve in time at different longitudinal positions, we obtain the fit of Figure 4.4 for $z = 3.0$ mm.

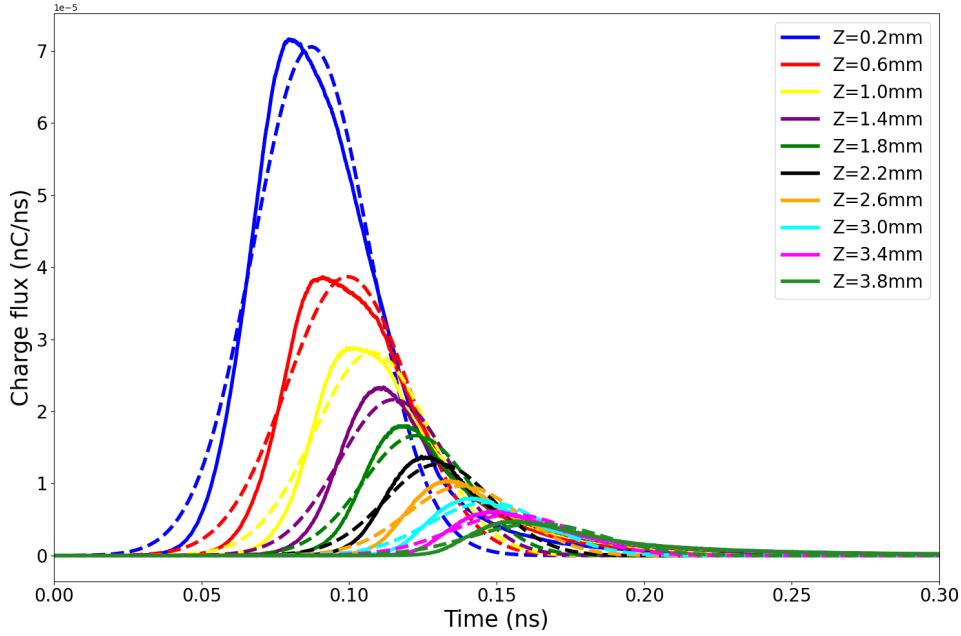

Figure 4.4 – Charge flux as a function of time in a radius $R = 1$ m at several positions z. PIC simulations results are in full lines and the Gaussian fit in dotted lines.

We observe in Figure 4.4 an agreement of the Gaussian fit to describe the proton beam as a function of time. We verify that the beam speed is constant so we can, via a change of variables, go from a beam Gaussian in time to a beam Gaussian in z.

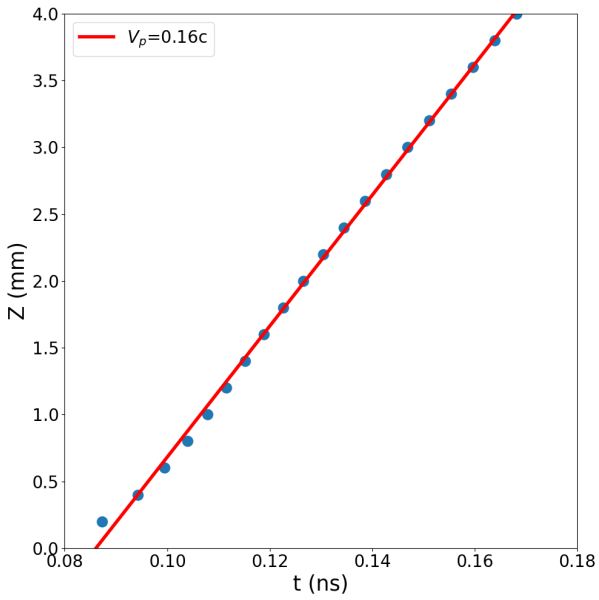

Figure 4.5 – Position of the TNSA beam Gaussian fit as a function of time and linear fit in red with a slope v_p.

We observe in Figure 4.5 that the beam is going at a constant speed of $v = 0.16c$ and we can, by an linear transformation $z = 0.16\ ct$ with c the speed of light, obtain the Gaussian distribution as a function of z and study the behaviour of the Gaussian in z:

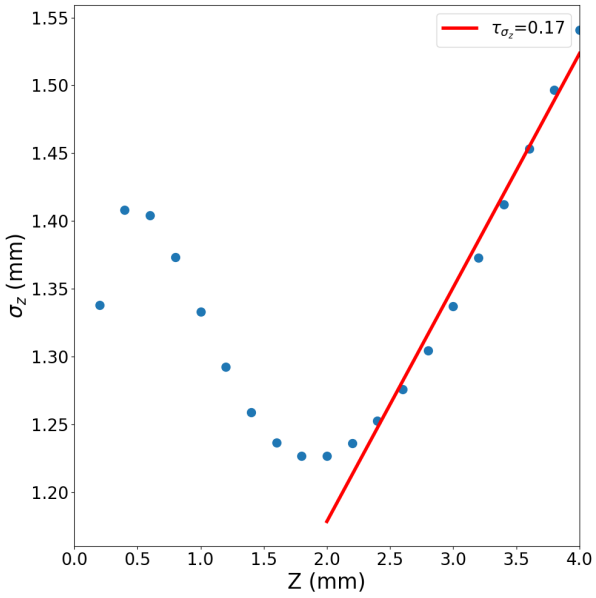

Figure 4.6 – Evolution of σ_z as a function of the longitudinal position and linear fit in red with a slope τ_{σ_z}.

We observe in Figure 4.6 that the Gaussian first narrows before $z = 2$ mm, this is due to the temporal distribution of the TNSA beam. Indeed, protons of all energies are emitted at every time, and there is a overlap between the most energetic protons and the least energetic protons which makes TNSA bunch narrow as the fast protons overtake the slow protons. Once the protons are sorted in energy, the beam linearly expands longitudinally under the influence of the space charge, at a speed close to the one observed in the radial case.

4.2.2.2 Modified Gaussian fit

The Gaussian fit presents a good agreement, but it is not a perfect fit. That is a reason why other fits have been explored, such as a modified Gaussian distribution, characterised by the formula

$$\rho_z(z_{beam}) = Q_z \frac{\lambda}{2} e^{\frac{\lambda}{2}(\lambda\sigma_z^2 - 2z_{beam})} \mathrm{erfc}\left(\frac{\lambda\sigma_z^2 - z_{beam}}{\sqrt{2}\sigma_z}\right) \tag{4.2.3}$$

with σ_z the characteristic size of the beam in the longitudinal direction, λ the damping factor, $z_{beam} = z - \bar{z}$ and $\bar{z}$ the average position of the proton beam.

We make the same time fit at different longitudinal positions as in the case of the Gaussian fit and we obtain the results plotted in Figure 4.7, for $z = 3.0$ mm.

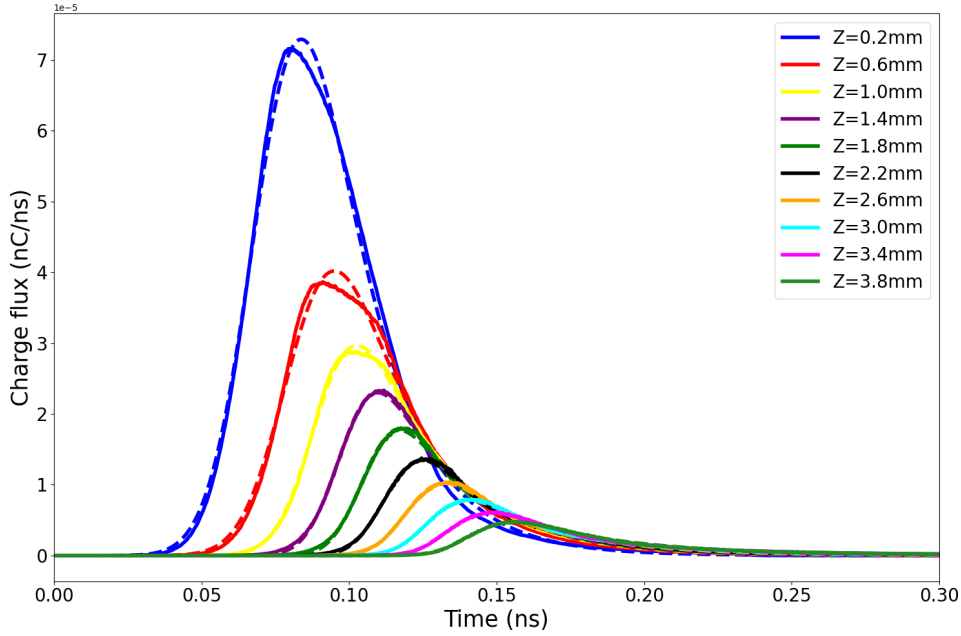

Figure 4.7 – Charge flux as a function of time in a radius $R = 1$ m at several positions z. PIC simulations results are in full lines and the exponentially modified Gaussian fit in dotted lines.

We observe a nearly perfect agreement of the exponentially modified Gaussian fit to describe the proton beam as a function of time. We now need to verify that the beam speed is constant so we can, via a change of variables, go from an exponentially modified Gaussian beam in time to an exponentially modified Gaussian beam in z.

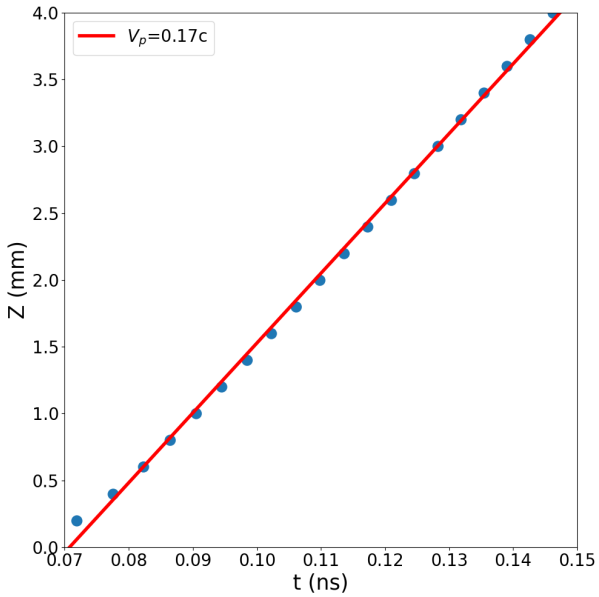

Figure 4.8 – Position of the TNSA beam exponentially modified Gaussian fit as a function of time.

As previously, we observe a beam going at a constant speed and we can, with an affine transformation, conclude that this is a nearly perfect fit in z of the beam shape.

Nevertheless, the formula is not trivial and the mathematical development of a space charge analytical model is impossible with this distribution function. That is the reason why I chose to describe the proton beam as a double Gaussian beam in r and in z for the theoretical modeling of space charge.

4.3 Theory of space charge of a Gaussian proton bunch

Now that we have an approximation of the proton beam shape, we can calculate the space charge fields of a non-relativistic Gaussian proton beam to implement it in the DoPPLIGHT theoretical model. The calculations are based on the space-charge model calculated by R. Wanzenberg at DESY for relativistic 3D-Gaussian electron bunches [98]. In all this section, we suppose we are in vacuum in regards to boundary conditions as a simplification to implement the space charge in DoPPLIGHT.

4.3.1 Resolution of the Poisson equation

First we need to solve the Poisson equation, which can be written as:

$$\Delta^2\Phi(\mathbf{r}) = \frac{-1}{\epsilon_0}\rho(\mathbf{r}) \tag{4.3.1}$$

with $\mathbf{r} = (x, y, z)$ and $\rho(\mathbf{r}$ the considered charge distribution of the bunch.

We can rewrite equation (4.3.1) as

$$\Delta^2\Phi(\mathbf{r}) = \frac{1}{\epsilon_0}\iiint_{\mathbb{R}^3} G(\mathbf{r},\mathbf{r}')\rho(\mathbf{r}')d^3\mathbf{r}' \tag{4.3.2}$$

with $G(\mathbf{r},\mathbf{r}')$ the corresponding Green function,

$$G(\mathbf{r},\mathbf{r}') = \frac{1}{4\pi|\mathbf{r}-\mathbf{r}'|} \tag{4.3.3}$$

and satisfying:

$$\Delta^2 G(\mathbf{r},\mathbf{r}') = -\delta(\mathbf{r}-\mathbf{r}') \tag{4.3.4}$$

Using the known formula $\int_0^\infty exp(-x^2\xi^2)d\xi = \sqrt{\pi}/2x$, we rewrite the Green function in integral form:

$$G(\mathbf{r},\mathbf{r}') = \frac{1}{2\pi^{3/2}}\int_0^\infty \exp(-|\mathbf{r}-\mathbf{r}'|^2\xi^2)d\xi \tag{4.3.5}$$

We then continue to the following change of variable $\xi = 1/\sqrt{(|q|)}$, and we reformulate equation (4.3.5) as

$$G(\mathbf{r},\mathbf{r}') = \frac{1}{4\pi^{3/2}}\int_0^\infty \frac{1}{q^{3/2}} exp(-|\mathbf{r}-\mathbf{r}'|^2/q)dq \tag{4.3.6}$$

Finally, we can express the electric potential $\Phi(\mathbf{r})$ as

$$\Phi(\mathbf{r}) = \frac{1}{4\pi\epsilon_0}\int_0^\infty \frac{1}{q^{3/2}\sqrt{\pi}}\iiint_{\mathbb{R}^3}\rho(\mathbf{r}')exp(-|\mathbf{r}-\mathbf{r}'|^2/q)dqd^3\mathbf{r}' \tag{4.3.7}$$

4.3.2 Case of a Gaussian bunch

We consider a Gaussian bunch defined by the following charge distribution

$$\rho(x,y,z) = \frac{Q}{(2\pi)^{3/2}\,\sigma_r^2\sigma_z} e^{-x^2/(2\sigma_r^2)-y^2/(2\sigma_r^2)-z^2/(2\sigma_z^2)}. \tag{4.3.8}$$

By inserting this charge distribution in Equation (4.3.7) we obtained for each variable r_i

$$\int_{-\infty}^{\infty} \frac{1}{\sqrt{2\pi}\sigma_i} \exp\left(\frac{-r_i'^2}{2\sigma_i^2}\right) \frac{1}{\sqrt{q}} \exp\left(\frac{-|r_i - r_i'|^2}{q}\right) dr_i' = \frac{\exp\left(\frac{r_i^2}{q+2\sigma_i^2}\right)}{\sqrt{q+2\sigma_i^2}}. \tag{4.3.9}$$

Applying this equation to x, y and z and adding them, we get:

$$\Phi(r,z) = \frac{Q}{4\pi\epsilon_0}\frac{1}{\sqrt{\pi}} \int_0^{\infty} \frac{\exp\left(-\frac{r^2}{q_r} - \frac{z^2}{q_z}\right)}{q_r\sqrt{q_z}} dq \tag{4.3.10}$$

with $q_i = q + 2\sigma_i^2$.

4.3.3 Electric field calculation

A calculation gives the following electric field components

$$\begin{aligned} E_r(r,z) &= \frac{-\partial}{\partial r}\Phi(r,z) \\ &= \frac{Q}{2\pi\epsilon_0}\frac{r}{\sqrt{\pi}} \int_0^{\infty} \frac{\exp\left(-\frac{r^2}{q_r} - \frac{(z-\bar{z})^2}{q_z}\right)}{q_r^2\sqrt{q_z}} dq, \end{aligned} \tag{4.3.11}$$

$$\begin{aligned} E_z(r,z) &= \frac{-\partial}{\partial z}\Phi(r,z) \\ &= \frac{Q}{2\pi\epsilon_0}\frac{z}{\sqrt{\pi}} \int_0^{\infty} \frac{\exp\left(-\frac{r^2}{q_r} - \frac{(z-\bar{z})^2}{q_z}\right)}{q_r q_z^{3/2}} dq. \end{aligned} \tag{4.3.12}$$

In the case of a beam of relativistic electrons, a Lorentz transform provides expressions for the electric and magnetic fields of a moving beam in the laboratory reference frame. The TNSA protons, with an energy of a few MeV, are not relativistic and the electrostatic expressions above are sufficient for the representation of the electric fields in DoPPLIGHT.

4.3.4 Mirror effect

We have to take into account the reflection of the electric fields due to the space charge of the proton beam on the foil target: indeed, as the space charge fields are the strongest when the proton bunch is close to the foil, the reflection of the electric field on the metallic surface has to be considered.

We consider an electromagnetic wave of frequency ω along the wave vector $\mathbf{k}$ written under the form

$$\begin{cases} \mathbf{E}(\mathbf{r},t) = \mathbf{E_0}\exp(\mathbf{k}\cdot\mathbf{r} - \omega t) \\ \mathbf{B}(\mathbf{r},t) = \mathbf{B_0}\exp(\mathbf{k}\cdot\mathbf{r} - \omega t) \end{cases} \tag{4.3.13}$$

with $k = \omega/v$ and $\mathbf{v}$ the velocity of the electromagnetic wave.

We have a transverse wave, so $\mathbf{E_0}\cdot\mathbf{k} = \mathbf{B_0}\cdot\mathbf{k} = 0$. We also have the Maxwell equation

$$\nabla \wedge \mathbf{E} = -\frac{\partial \mathbf{B}}{\partial t}. \tag{4.3.14}$$

And we get the relation between $\mathbf{E_0}$ and $\mathbf{B_0}$,

$$\mathbf{B_0} = \frac{\hat{\mathbf{k}} \wedge \mathbf{E_0}}{v} \tag{4.3.15}$$

with $\hat{\mathbf{k}} = \mathbf{k}/k$ the unit vector in the direction of the wave propagation

We suppose that the plane $z = 0$ is a boundary between two dielectrics of refractive index n_1 on the side of the incident wave and n_2 on the other side, see Figure 4.9.

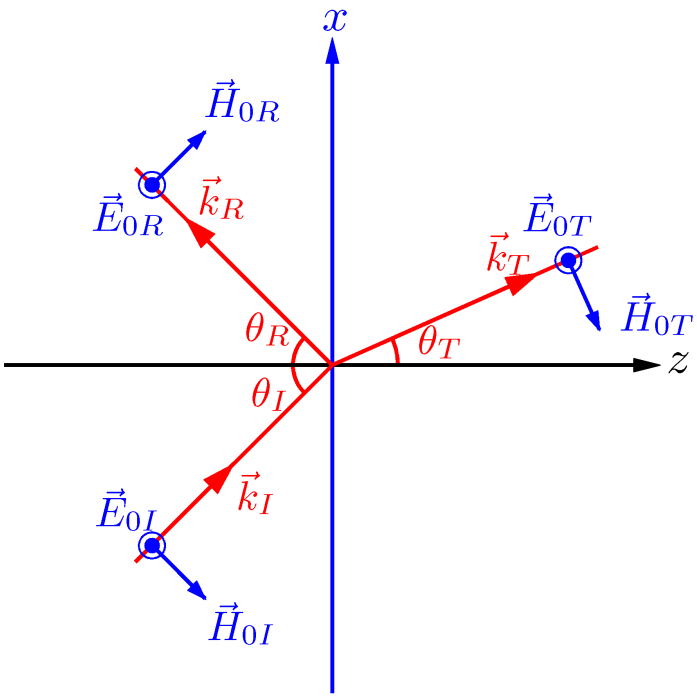

Figure 4.9 – Scheme of the reflection and transmission of an electromagnetic wave at a dielectric interface.

Our proton beam being on the axis, we suppose a normal incidence of the incident electromagnetic field that we can rewrite under the form

$$\begin{cases} \mathbf{E_i}(z,t) = \mathbf{E_i}\exp(k_1 z - \omega t) \\ \mathbf{B_i}(z,t) = \frac{E_i}{v_1}\exp(k_1 z - \omega t)\mathbf{e}_{\mathrm{Bi}} \end{cases} \tag{4.3.16}$$

with $k_1 = \omega/v_1$, $v_1 = c/n_1$ and $\mathbf{e}_{\mathrm{Bi}}$ the unit vector of the incident magnetic field.

The reflected and transmitted waves take the form

$$\begin{cases} \mathbf{E_r}(z,t) = \mathbf{E_r}\exp(-k_1 z - \omega t) \\ \mathbf{B_r}(z,t) = -\frac{E_r}{v_1}\exp(-k_1 z - \omega t)\mathbf{e}_{\mathrm{Br}} \end{cases} \tag{4.3.17}$$

$$\begin{cases} \mathbf{E_t}(z,t) = \mathbf{E_t}\exp(k_2 z - \omega t) \\ \mathbf{B_t}(z,t) = \frac{E_t}{v_2}\exp(k_2 z - \omega t)\mathbf{e}_{\mathrm{Bt}} \end{cases} \tag{4.3.18}$$

with $k_2 = \omega/v_2$ and $v_2 = c/n_2$.

In the case of a normal incidence, the boundary condition between two dielectric media is:

$$\begin{cases} E_{\parallel 1} = E_{\parallel 2}, \\ B_{\parallel 1} = B_{\parallel 2}, \end{cases} \tag{4.3.19}$$

which gives

$$\begin{cases} E_i + E_r = E_t, \\ \frac{E_i - E_r}{v1} = \frac{E_t}{v_2}. \end{cases} \tag{4.3.20}$$

As we have $v_1/v_2 = n_2/n_1$, we can rewrite the previous system of equations as

$$\begin{cases} E_r = \frac{n_1 - n_2}{n_1 + n_2} E_i \\ E_t = \frac{2n_1}{n_1 + n_2} E_i \end{cases} \tag{4.3.21}$$

In the case of an interface between vacuum and a perfect conductor, we have $n_1 = 0$ and $n_2 = 1$, which means:

$$\begin{cases} E_r = -E_i, \\ E_t = 0. \end{cases} \tag{4.3.22}$$

which corresponds, in the case of the space charge field of a proton bunch located at a position $\bar{z}$ to a reflected field equal to the space charge field of a bunch of protons of equal charge at $\bar{z}$ propagating in the opposite direction, i.e.:

$$\mathbf{E_r}(z - \bar{z}) = -\mathbf{E_i}(-(z + \bar{z})) \tag{4.3.23}$$

4.4 Integration of the space charge field in DoPPLIGHT

Now that we know the theoretical expression of the space charge of our Gaussian proton beam, we need to implement it in our theoretical model DoPPLIGHT.

We want to keep the calculation complexity at the same level and not to slow down the code. In order to do that, we reworked the fields equations on a grid $\left(\frac{r}{\sigma_r}, \frac{z}{\sigma_z}, \frac{\sigma_r}{\sigma_z}\right)$:

$$E_{r,SC}(\alpha_r, \alpha_z, \alpha) = E_{r0} \int_0^\infty \frac{1}{\sqrt{2+q}} \left(\frac{2+q}{\alpha^2}\right)^2 \exp\left(\frac{-\alpha_z^2}{2q} - \frac{\alpha_r^2}{2 + q/\alpha^2}\right) dq \tag{4.4.1}$$

$$E_{z,SC}(\alpha_r, \alpha_z, \alpha) = E_{z0} \int_0^\infty \frac{1}{(q+2\alpha^2)(2+q)^{3/2}} \exp\left(\frac{-\alpha_z^2}{2q} - \frac{\alpha_r^2}{2 + q/\alpha^2}\right) dq \tag{4.4.2}$$

with $\alpha_r = \frac{r}{\sigma_r}$, $\alpha_z = \frac{z - \bar{z}}{\sigma_z}$, $\alpha = \frac{\sigma_r}{\sigma_z}$ and q the integration reduced variable.

At every time step, we calculate $\bar{z}$ the average longitudinal position of the protons, Q the charge of the protons inside the coil, σ_r and σ_z. We also calculate E_{r0} and E_{z0} as follows:

$$E_{r0} = \frac{Qr\sigma_z}{2\pi^{3/2}\epsilon_0\sigma_r^4} \tag{4.4.3}$$

$$E_{z0} = \frac{Q}{2\pi^{3/2}\epsilon_0\sigma_z^3} \tag{4.4.4}$$

Once these quantities are calculated, we interpolate both the space charge electric fields on every particle at every time step as we do with the helical coil field. The calculation complexity is $O(n)$, with n the number of particles, which is of the same order as the helical coil interpolation. This module is then time-resolved as are the coil fields and, contrary to a PIC code, not self-consistent.

We also take into account the reflected field on the metal foil, for that we do

$$E_{SC,total} = E(z - \bar{z}) - E(-(z + \bar{z})). \tag{4.4.5}$$

But this method leads to an overestimation of the space charge fields inside the coil. The reason for overestiming of the field is that we did not take into account the progressive charging of the TNSA beam by the helical coil fields. Indeed, as the beam is expelled from the metallic foil, it is composed of fast electrons, protons and an equal amount of slow electrons. As all particles see the same the helical coil fields, the protons are focused and the electrons are defocused by the GV/m radial fields generated by the helical coil. The electrons being 3 orders of magnitude lighter, they are quickly expelled from the helical coil. As they leave the beam, the beam is getting progressively positively charged, increasing the space charge as the electrons leave the coil.

To model this effect, we created a module in DoPPLIGHT taking into account the possibility to inject several species into the helical coil. We then calculate $\bar{z}$ the average longitudinal position of the protons, σ_r and σ_z as previously, but we now calculate the net charge inside 3σ by taking into account the charge of the different species. This method takes into account the faster electron loss.

4.4.1 Validation of the space charge model

In order to validate our space charge model, we first compare the space charge of a proton beam characteristic of the LULI TNSA emission in vacuum using both our large-scale PIC simulations and our theoretical model.

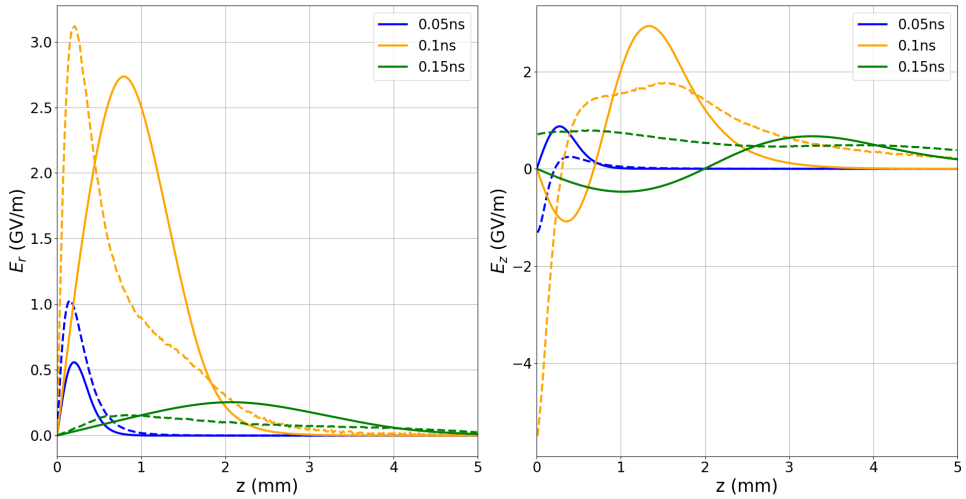

Figure 4.10 – PIC simulated (dashed line) and DoPPLIGHT calculated (a) radial and (b) longitudinal electric fields as a function of the longitudinal position and at different times in the case of a TNSA beam and no HC. The particles features are defined in Table 2.2 for LULI. The current is defined analytically by a Gaussian with FWHM $\tau_{\mathrm{FWHM}} = 8.5$ ps and amplitude $I_0 = 30$ kA at $z = 0$ mm , delayed with respect to the particle emission by 6 ps.

The first step to validate our space charge model was to compare the propagation of a TNSA beam in vacuum under its own space charge fields only. In Figure 4.10, we see a better agreement between DoPPLIGHT and SOPHIE when they both only calculate the space charge fields, especially on the radial field E_r. The amplitude of the space charge fields, is correctly reproduced with a slight position shift. The agreement is also better for the longitudinal field E_r after 300 μm. The difference of fields near the emission spot is due to the TNSA charge separation field, the electric field generated at the surface of the foil by the charging of the foil, which is not modelled in DoPPLIGHT but taken into account in SOPHIE.

4.4.2 Impact on the field propagation

Then we compare the fields propagation in SOPHIE and DoPPLIGHT in the case of a proton beam going through a HC and their match throughout propagation.

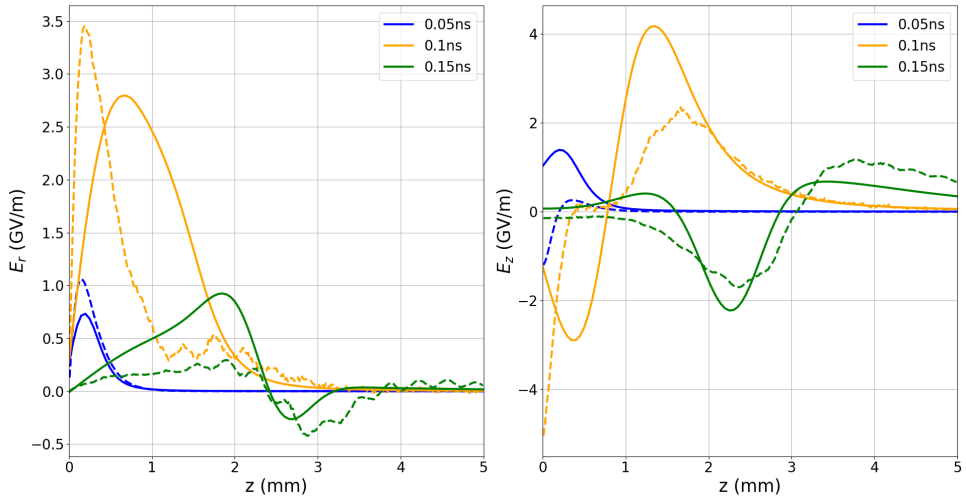

Figure 4.11 – PIC simulated (dashed line) and DoPPLIGHT calculated (a) radial and (b) longitudinal electric fields as a function of the longitudinal position and at different times. The HC parameters are: length $L = 5$ mm, radius in the heart of the coil $a = 0.5$ mm, external radius 0.6 mm and step $h = 0.35$ mm. The particles features are defined in Table 2.2 for LULI. The current is defined analytically by a Gaussian with FWHM $\tau_{\text{FWHM}} = 8.5$ps and amplitude $I_0 = 30$ kA at $z = 0$ mm , delayed with respect to the particle emission by 6 ps.

We see in Figure 4.11 a fairly good agreement between the PIC simulated and model calculated fields. While there is some difference in amplitude and positioning of the fields, we obtain the correct order of magnitude and of the appropriate sign, which was not the case in Figure 4.1. The main difference we can observe between PIC simulations and DoPPLIGHT calculations is the strong decelerating fields at the edge of the target foil observed without the HC.

In conclusion, we have a good enough qualitative agreement between the PIC simulations and DoPPLIGHT so we can implement this new space charge module with multi-species emission in our study of the HC physics.

4.4.3 Impact on the proton spectrum

Now that our model has been validated for the propagation of the fields, I present the impact of space charge fields on the proton spectrum at the exit of the HC.

First, we see our starting point of DoPPLIGHT without the space charge module.

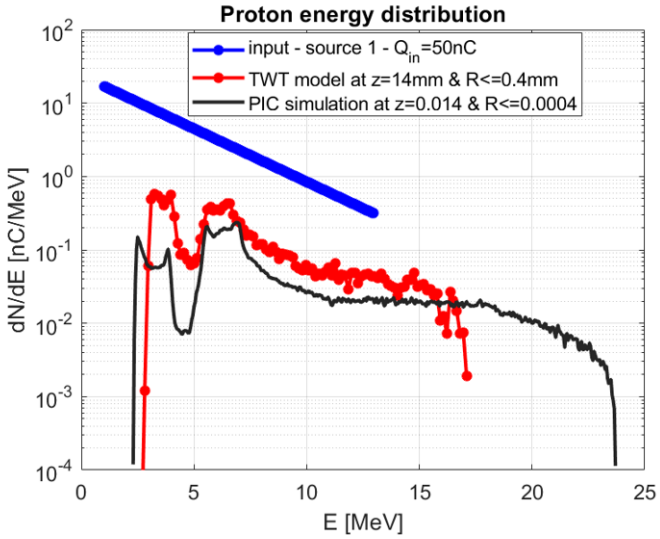

Figure 4.12 – Input proton energy spectrum (in blue), PIC simulated spectrum at the exit of the helical coil (in black) and DoPPLIGHT calculated spectrum at the exit of the coil without space charge fields (in red). The HC parameters are: length $L = 15$ mm, radius in the heart of the coil $a = 0.5$ mm, external radius 0.6 mm and step $h = 0.35$ mm. The particles features are defined in Table 2.2 for LULI. The current is defined analytically by a Gaussian with FWHM $\tau_{\text{FWHM}} = 8.5$ ps and amplitude $I_0 = 30$ kA at $z = 0$ mm, delayed with respect to the particle emission by 6 ps.

In Figure 4.12, we observe that DoPPLIGHT without a space charge module overestimates the spectrum charge at the exit of the helical coil by a factor of 2 for high energy protons up to 6 for low energy protons. The agreement is already good, especially in terms of the position and shape of the bunches, but DoPPLIGHT overstimates the number of protons and, by extension, the total charge at the exit of the HC. There is a clear need to take into account the space charge fields to have a model consistent with the large-scale PIC simulations.

By implementing the space charge and multi-species modules presented in this chapter, we obtain the spectrum of Figure 4.13 at the exit of the coil:

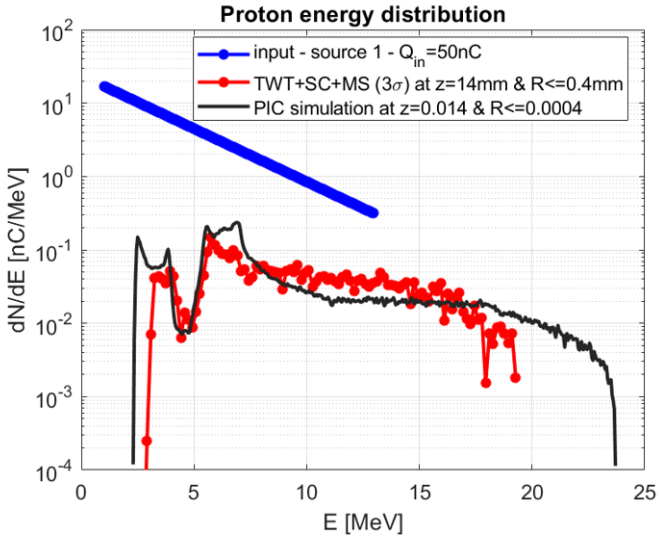

Figure 4.13 – Input proton energy spectrum (in blue), PIC simulated spectrum at the exit of the helical coil (in black) and DoPPLIGHT calculated spectrum at the exit of the coil with the helical coil and space charge fields and the multi-species module (in red). The HC parameters are: length $L = 15$ mm, radius in the heart of the coil $a = 0.5$ mm, external radius 0.6 mm and step $h = 0.35$ mm. The particles features are defined in Table 2.2 for LULI. The current is defined analytically by a Gaussian with FWHM $\tau_{\mathrm{FWHM}} = 8.5$ ps and amplitude $I_0 = 30$ kA at $z = 0$ mm, delayed with respect to the particle emission by 6 ps.

With the new module, we obtain a close agreement between the PIC simulation and the DoPPLIGHT calculation, on the low energy structures and on the level of the plateau at mid and high energies. We have then validated the space charge model in DoPPLIGHT. The next physical module to be added should be the model of the TNSA charge separation in order to match the cut-off energy between SOPHIE and DoPPLIGHT, which is not modelised at this time.

4.5 Conclusion and perspectives

In this chapter, using large-scale PIC simulations, I first characterised the shape of a TNSA proton beam in the axial and radial directions. We observed that a Gaussian charge density is a reasonable approximation for the shape of our TNSA proton beam.

This enabled the calculation of the space charge fields of a non-relativistic Gaussian proton beam, equivalent to our TNSA beam propagating in vacuum during the first moment of propagation through the helical coil.

We were able to integrate the physics of the proton beam space charge inside the helical coil in DoPPLIGHT without increasing the complexity of our theoretical model. It also takes into account the effects of the foil on the electric fields as well as the progressive charging of the TNSA proton beam during its progression through the coil.

With this new module implemented in DoPPLIGHT, we now have a fast, efficient and accurate model to simulate the protons dynamics inside HCs, enabling us to optimise the HC's performances in terms of focusing, post-acceleration, bunching and yield.

Chapter 5

Design of a new helical coil with controlled dispersion

The objective of this chapter is to develop a new helical coil design with controlled dispersion to overcome the limiting effect of dispersion on the cut-off energy and bunching observed in Chapter 3. For this, I first developed a new helical coil scheme with a tube to reduce the current dispersion through the helical coil. I then developed a theory of the current and electro-magnetic fields propagation so we could update our theoretical model DoPPLIGHT. We then implemented it in DoPPLIGHT in order to study the impact of this new scheme on a TNSA beam.

5.1 Description of the helical coil with tube scheme

5.1.1 Motivation

As shown in previous chapters of this manuscript, the helical coil target scheme for post-acceleration of TNSA protons has proven to be efficient experimentally in terms of focusing and spectral shaping of the TNSA proton beam [37], [39], [99]–[102] but has also shown limitations in terms of proton cut-off energy, yield and bunching. The first and third limitations are due to the dispersive nature of HCs, where the current changes sign along the longitudinal axis, inducing alternating accelerating and decelerating fields seen by the protons, leading to a reduction in the cut-off energy and limited bunching.

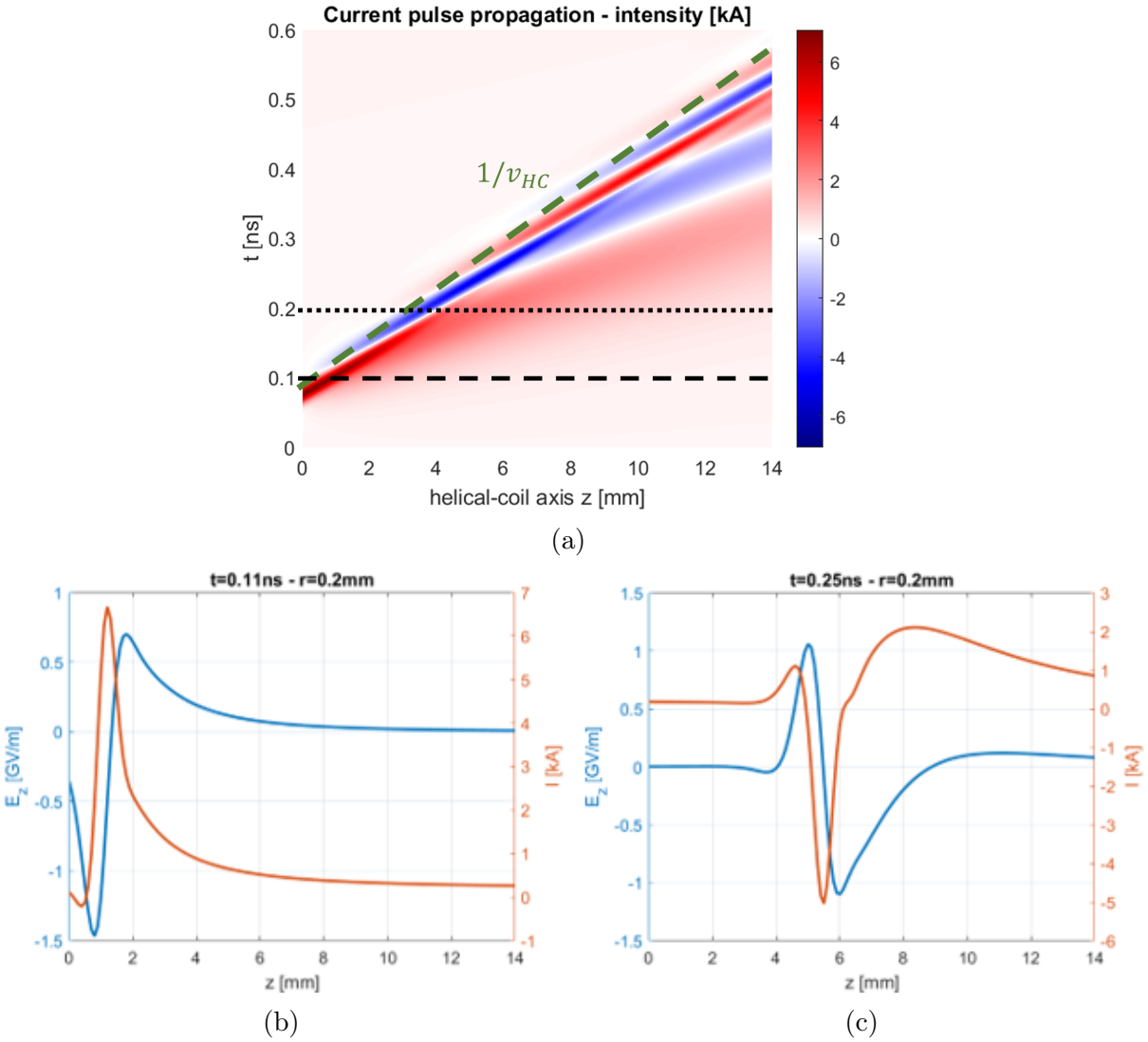

(a)

(b)

(c)

Figure 5.1 – PIC simulation of (a) the current pulse intensity in kA for a helical coil without tube as a function of time and along the HC axis, (b) current (in red) and longitudinal electric field (in blue) along the HC axis at t=0.11ns, (c) current (in red) and longitudinal electric field (in blue) along the HC axis at t=0.2ns. The HC parameters are: length $L = 15$ mm, radius in the heart of the coil $a = 0.5$ mm, external radius 0.6 mm and step $h = 0.35$ mm.

As shown in Figure 5.1, we observe a strong dispersion of the current along the helical coil, characterised by a regular sign change of the current and a temporal spread inducing a drop in intensity of the current as it propagates. The sign shifts create two different regimes of longitudinal electric fields: the first one, corresponding to a positive current pulse, is shown in Figure 5.1b and is characterised by an accelerating field followed by a decelerating field which splits the proton beam in two. The second regime, corresponding to a negative current pulse and shown in Figure 5.1c, is characterised by a decelerating field followed by an accelerating field which creates a proton bunch.

To overcome this limitation, several schemes have been introduced: Kar *et al.* use short helical coils where the current does not have time to change sign [37], Robertson *et al.* use two stages of short helical coils in a row powered by two laser beams [103] and Liu *et al.* proposed a new scheme with two sections of HC to skip phase reversal [96].

I instead propose a new scheme of HC with a tube, inspired by broadband high-power TWT [104], [105] discussed in the context of our collaboration with PIIM and Thalès.

5.1.2 Scheme of a HC with tube

In this proposed scheme, shown in figure 5.2a, the HC is inserted inside a metallic tube. The HC and the tube are both connected to the ground but only the helix is connected to the TNSA target, making the HC system similar to a coaxial line with a helical conductor inside. This is inspired by broadband high-power Traveling Wave Tubes (TWT), see figure 5.2b. The idea of this scheme is to create a hybrid mode between the dispersive helical coil and the dispersion-free conducting tube. The dielectric rod used in broadband high-power TWTs is suppressed due to the risk of short-circuit with the intense kA current going through the coil.

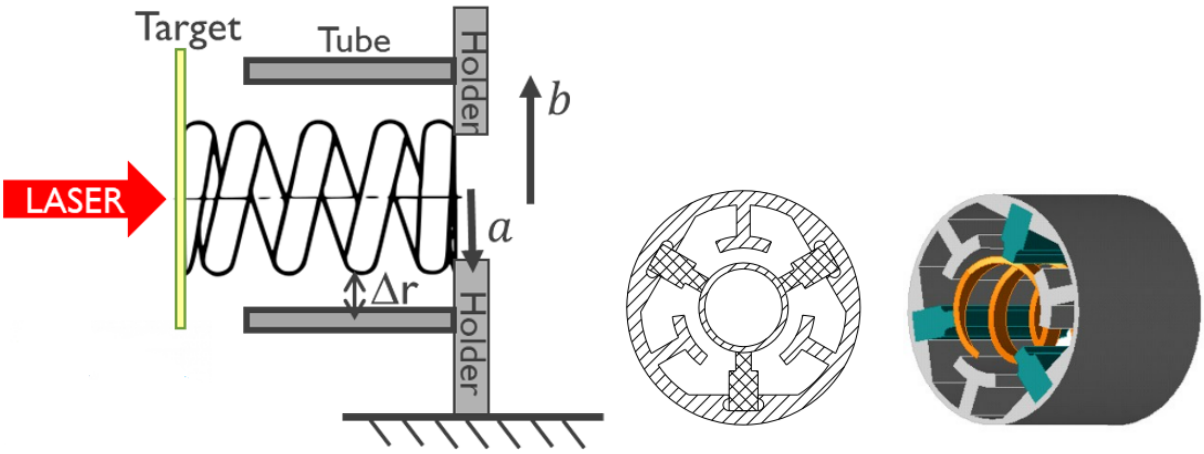

(a) (b)

Figure 5.2 – Scheme of : (a) a helical coil with tube, (b) a broadband high-power TWT [105].

To see the effect of the tube on the current dispersion in the helical coil, a first PIC simulation with SOPHIE was performed to observe the current propagation along the helical coil. The first results, presented in Figure 5.3, show a drastic reduction of the current dispersion and the emergence of a positive current pulse that propagates at a constant speed along the helical coil axis $V = 1.2\ V_{\mathrm{HC}}$, with $V_{\mathrm{HC}} = c/\sqrt{1 + (2\pi a/h)^2}$ the characteristic velocity of the helix, corresponding to the longitudinal speed of a current pulse going at the speed c along the helical coil.

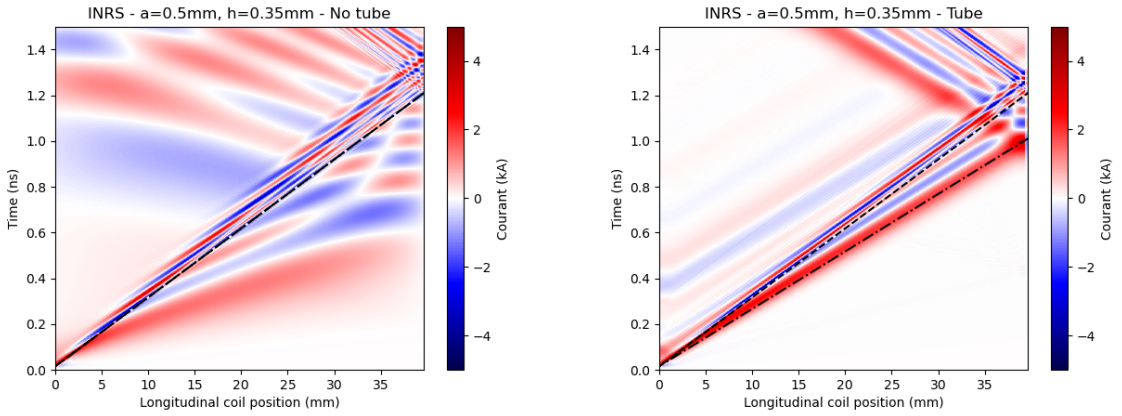

(a) (b)

Figure 5.3 – PIC simulation of the current pulse intensity in kA for a helical coil (a) without tube and (b) with tube as a function of time and along the HC axis. The HC parameters are: length $L = 40$ mm, radius in the heart of the coil $a = 0.5$ mm, external radius 0.6 mm and step $h = 0.35$ mm with a tube of radius $b = 0.9$ mm. The dashed line corresponds to V_{HC}, the geometrical speed of the HC, the dash-dotted line corresponds to $V = 1.2\ V_{\mathrm{HC}}$.

These promising results lead us to study the theoretical equations behind this new scheme in order to implement the helical coils with tube into our model DoPPLIGHT.

5.2 Theory of the current and electromagnetic fields propagation in a helical coil with tube

To understand the effect of the tube in new HC targets, we first present the theory describing the effect of the tube on the current and electromagnetic fields in the HC.

5.2.1 Dispersion relation in a HC with and without tube

From the model presented in Section 1.4, we get the following dispersion relation for a regular HC:

$$\omega = \frac{kc}{\sqrt{1 + \cot^2(\Psi)\frac{I_1(\alpha)K_1(\alpha)}{I_0(\alpha)K_0(\alpha)}}} \tag{5.2.1}$$

where I_i and K_i are the modified Bessel functions of order i, $\alpha(\omega) = a\sqrt{k^2 - \omega^2/c^2}$, $\Psi = \arctan(\frac{h}{2\pi a})$ is the helix angle, a is the radius of the helix and h is the pitch of the helix.

In particular, in the low frequency limit, $(a\omega/c)\cot\Psi \ll 1$, one has $\alpha \ll 1$, so $I_1(\alpha) \sim \frac{\alpha}{2}$, $I_0(\alpha) \sim 1$, $K_0(\alpha) \sim -ln(\alpha)$, $K_1(\alpha) \sim \frac{1}{\alpha}$, and finally $k \sim \omega/c$.

So, at low frequency, the phase velocity is close to the light velocity.

On the other hand, for $(a\omega/c)\cot\Psi \gg 1$, we have $\alpha \gg 1$, $I_0(\alpha), I_1(\alpha) \sim \frac{1}{\sqrt{2\pi\alpha}}e^{\alpha}$, $K_0(\alpha), K_1(\alpha) \sim \sqrt{\frac{\pi}{2\alpha}}e^{-\alpha}$, and finally:

$$\omega \sim \frac{kc}{\sqrt{1+\cot^2(\Psi)}} \tag{5.2.2}$$

So, at high frequency, the phase velocity is reduced to $\frac{c}{\sqrt{1+cot^2(\Psi)}}$, which is smaller than c and depends only on the helix pitch and radius.

Thanks to these asymptotic estimates, we deduce that the low frequency mode propagates into the coil faster than the high frequency mode, due to the dispersion of the current pulse propagation.

In an attempt to reduce the dispersion, in the 1990s, Freund *et al.* proposed a new element for an existing TWT scheme adding a loss-free conducting wall (tube) of radius b to enclose the HC [106]. The theoretical model proposed is based on the same assumption of an infinitesimally thin helix, with the current propagating in the helical direction, in the Fourier domain. The authors obtain the dispersion relation [106]

$$\omega = kc \Bigg/ \left(\sqrt{1+\cot^2(\Psi)\frac{I_1(\alpha)I_0(\alpha b/a)[K_1(\alpha b/a)I_1(\alpha)-I_1(\alpha b/a)K_1(\alpha)]}{I_0(\alpha)I_1(\alpha b/a)[K_0(\alpha b/a)I_0(\alpha)-I_0(\alpha b/a)K_0(\alpha)]}} \right) \tag{5.2.3}$$

In particular, one returns to the dispersion relation (5.2.1) in the limit where $b \to \infty$: then $I_1(\alpha b/a), I_0(\alpha b/a) \sim \exp(\alpha b/a)$, $K_1(\alpha b), K_0(\alpha b) \sim \sqrt{\pi a/(2\alpha b)}\exp(\alpha b/a)$. Conversely, in the limit $b = a$, the helix current is short circuited by the axial current in the tube, so $\omega/k = 1/\sqrt{1+\cot^2(\Psi)}$. Indeed, if $b \to \infty$, we have only the HC and if $b \to a$ we get a perfectly conducting tube without dispersion.

We conclude that the tube mitigates the current dispersion. This mitigation is presented in Figure 5.4 where the dispersion relation and the phase velocity $v_{ph} = \omega/k$ are plotted as a function of the wave vector for different values of b/a.

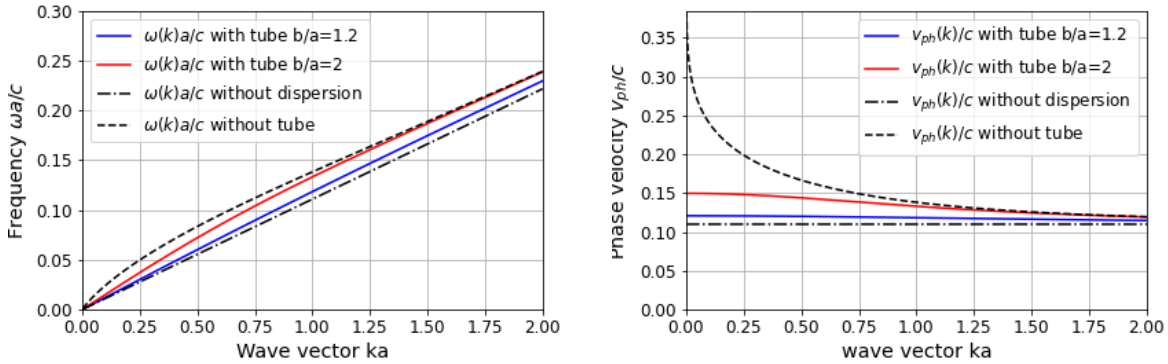

(a) (b)

Figure 5.4 – Comparison for a HC of radius $a = 0.5$ mm, pitch $h = 0.35$ mm, with tubes of different radii and without tube of the (A) normalized angular frequency and the (B) normalized phase velocity. Both as a function of the normalized wave vector.

Therefore, a hybrid model combining a regular coil and a non-dispersive tube enables one to control the mode phase velocity and to reduce the dispersion. On the other hand, with our tube geometry (b/a=1.2), the electric field available to accelerate the protons is

reduced by a factor of about 1.5 compared to the free helix. Therefore, the choice of the tube diameter b is the result of a compromise, where one must mitigate the dispersion without too much reducing the field amplitude.

5.2.2 Electromagnetic fields in a HC with tube

From this dispersion relation and doing the same calculation as in Section 1.4, we obtain the electric and magnetic fields inside the helix that we implement in the DoPP-LIGHT model.

In the case of the tube, the boundary counditions leading equation (1.4.11) are changed. With the tube, we know have, at $r = b$, $E_z = 0$ and $B_r = 0$, hich gives us the following relationships

$$\begin{cases} B_4^+ = -B_3^+ \frac{I_0(\alpha b)}{K_0(\alpha b)}, \\ B_2^+ = B_1^+ \frac{I_1(\alpha b)}{K_1(\alpha b)}. \end{cases} \tag{5.2.4}$$

By expanding the calculations, we obtain for a helix of radius a, pitch h, angle Ψ and surrounded by a conductive tube of radius b, the following electromagnetic fiels in the coordinate system (r, z, t):

$$\begin{cases} E_r(r,z,t) = \frac{\mu_0}{2\pi^2 a} \int_0^{+\infty} \frac{i_0(\omega)\omega k(\omega)}{\alpha^2} \frac{I_1(\alpha a)[K_1(\alpha b)I_1(\alpha a) - I_1(\alpha b)K_1(\alpha a)]}{I_0(\alpha a)[I_1(\alpha a)I_1(\alpha b)K_0(\alpha a) + I_0(\alpha a)I_1(\alpha b)K_1(\alpha a)]} \\ \qquad \times \cot^3(\Psi)\cos(\Psi) I_1(\alpha r)\cos(k(\omega)z - \omega t)d\omega \\ E_\theta(r,z,t) = \frac{\mu_0}{2\pi^2 a} \int_0^{+\infty} \frac{i_0(\omega)\omega}{\alpha} \frac{K_1(\alpha b)I_1(\alpha a) - I_1(\alpha b)K_1(\alpha a)}{I_1(\alpha a)I_1(\alpha b)K_0(\alpha a) + I_0(\alpha a)I_1(\alpha b)K_1(\alpha a)} \\ \qquad \times \cot^2(\Psi)\cos(\Psi) I_1(\alpha r)\sin(k(\omega)z - \omega t)d\omega \\ E_z(r,z,t) = \frac{\mu_0}{2\pi^2 a} \int_0^{+\infty} \frac{i_0(\omega)\omega}{\alpha} \frac{I_1(\alpha a)[K_1(\alpha b)I_1(\alpha a) - I_1(\alpha b)K_1(\alpha a)]}{I_0(\alpha a)[I_1(\alpha a)I_1(\alpha b)K_0(\alpha a) + I_0(\alpha a)I_1(\alpha b)K_1(\alpha a)]} \\ \qquad \times \cot^3(\Psi)\cos(\Psi) I_0(\alpha r)\sin(k(\omega)z - \omega t)d\omega \end{cases} \tag{5.2.5}$$

$$\begin{cases} B_r(r,z,t) = -\frac{\mu_0}{2\pi^2 a} \int_0^{+\infty} \frac{i_0(\omega)k(\omega)}{\alpha} \frac{K_1(\alpha b)I_1(\alpha a) - I_1(\alpha b)K_1(\alpha a)}{I_1(\alpha a)I_1(\alpha b)K_0(\alpha a) + I_0(\alpha a)I_1(\alpha b)K_1(\alpha a)} \\ \qquad \times \cot^2(\Psi)\cos(\Psi) I_1(\alpha r)\sin(k(\omega)z - \omega t)d\omega \\ B_\theta(r,z,t) = \frac{\mu_0}{2\pi^2 a c^2} \int_0^{+\infty} \frac{i_0(\omega)\omega^2}{\alpha^2} \frac{I_1(\alpha a)[K_1(\alpha b)I_1(\alpha a) - I_1(\alpha b)K_1(\alpha a)]}{I_0(\alpha a)[I_1(\alpha a)I_1(\alpha b)K_0(\alpha a) + I_0(\alpha a)I_1(\alpha b)K_1(\alpha a)]} \\ \qquad \times \cot^3(\Psi)\cos(\Psi) I_1(\alpha r)\cos(k(\omega)z - \omega t)d\omega \\ B_z(r,z,t) = -\frac{\mu_0}{2\pi^2 a} \int_0^{+\infty} i_0(\omega) \frac{K_1(\alpha b)I_1(\alpha a) - I_1(\alpha b)K_1(\alpha a)}{I_1(\alpha a)I_1(\alpha b)K_0(\alpha a) + I_0(\alpha a)I_1(\alpha b)K_1(\alpha a)} \\ \qquad \times \cot^2(\Psi)\cos(\Psi) I_0(\alpha r)\cos(k(\omega)z - \omega t)d\omega \end{cases} \tag{5.2.6}$$

These calculations have been made by Clément Lacoste within his PhD work.

5.3 Particle-In-Cell simulations and reduced model results for the current propagation in a HC with tube

In order to validate the theoretical model, we first performed full-scale PIC simulations of TNSA protons with a HC surrounded by a metallic tube using SOPHIE [86], already presented in Subsection 2.2.1. All the figures in this Section 5.3 correspond to a coil of parameters: length $L = 40$ mm, radius in the heart of the coil $a = 0.5$ mm, external radius=0.6 mm and step $h = 0.35$ mm with a tube of radius $b = 0.9$ mm when the tube is present. But the simulations and calculations have been performed for more geometries and the figures for other geometries are presented in Apendix A.

5.3.1 PIC simulations

The results of the SOPHIE simulations are presented in Figure 5.5 which represents the current pulse propagation along the HC axis as a function of time. The impact of the metallic tube around the HC leading to a drastic reduction of the current dispersion can be seen from comparison of the left and right panels.

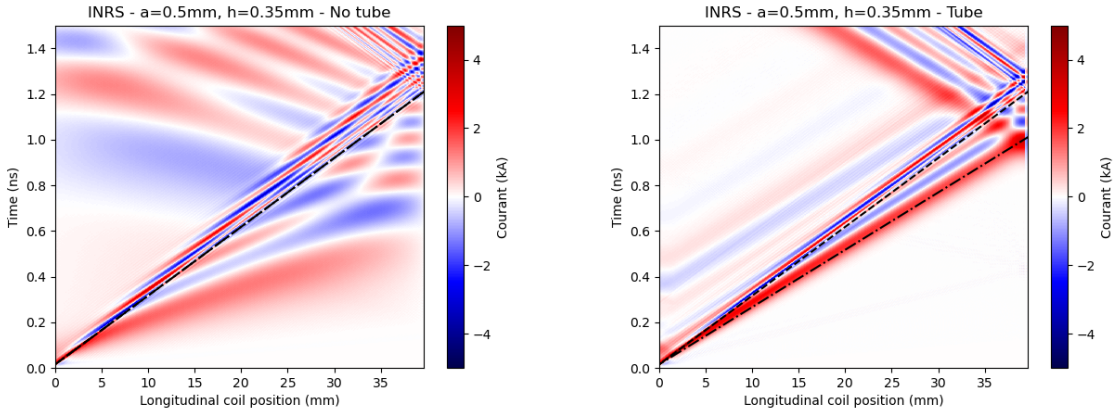

(a) (b)

Figure 5.5 – PIC simulation of the current pulse intensity in kA for a helical coil (a) without tube and (b) with tube as a function of time and along the HC axis. The particles features are defined in Table 2.2 for ALLS. The HC parameters are: length $L = 40$ mm, radius in the heart of the coil $a = 0.5$ mm, external radius 0.6 mm and step $h = 0.35$ mm with a tube of radius $b = 0.9$ mm. The dashed line corresponds to V_{HC}, the geometrical speed of the HC, the dash-dotted line corresponds to $V = 1.2\ V_{\mathrm{HC}}$.

With a single HC, as seen in Figure 5.5a, we observe many sign alternations of the current pulse propagating along the axis with the phase speed V_{HC}. One can see accelerated parts of the pulse propagating faster than V_{HC}, larger in time and lower in amplitude. All these features are clear signs of the coil dispersive nature.

In the case of a HC with tube, one clearly sees a pulse of positive current propagating at a constant speed $V = 1.2\ V_{\mathrm{HC}}$ and spreading temporally by a factor between 2 and 3 depending on the geometry, along with a reduction of amplitude by the same factor. This is due to the fact that, while the dispersion is reduced, it is not suppressed.

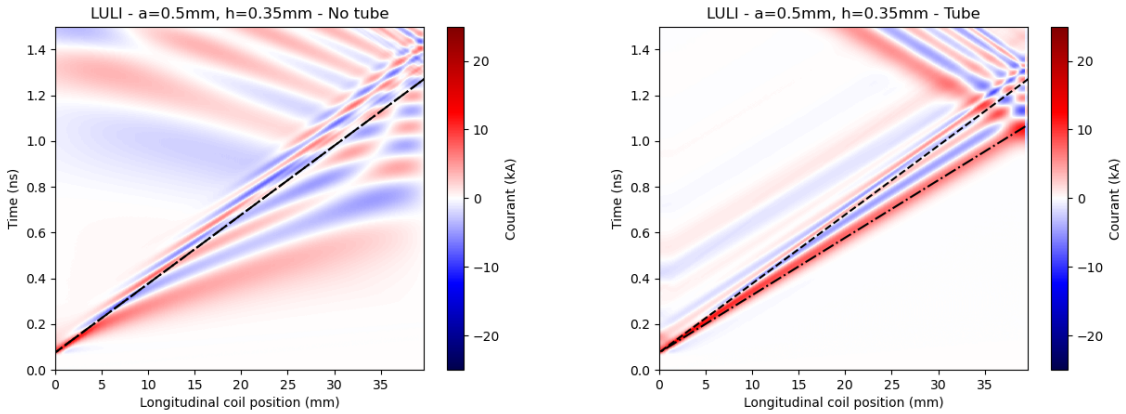

(a) (b)

Figure 5.6 – PIC simulation of the current pulse intensity in kA for a helical coil (a) without tube and (b) with tube as a function of time and along the HC axis. The particles features are defined in Table 2.2 for LULI2000. The HC parameters are: length $L = 40$ mm, radius in the heart of the coil $a = 0.5$ mm, external radius=0.6 mm and step $h = 0.35$ mm with a tube of radius $b = 0.9$ mm. The dashed line corresponds to V_{HC}, the geometrical speed of the HC, the dash-dotted line corresponds to $V = 1.2\ V_{\mathrm{HC}}$.

As one can see in Figure 5.6, these results are very similar in the case of a higher laser energy facility, similar to LULI2000. In the case of a HC with tube, the positive current pulse propagates at a constant speed $V = 1.2\ V_{\mathrm{HC}}$ and presents the same temporal spread and amplitude reduction as in the case of the ALLS laser facility.

5.3.2 Reduced model results: the DoPPLIGHT code

PIC simulations are time consuming, but they can be used to validate the reduced numerical model of current propagation in the coil based on the dispersion equation described in Section 5.2. The code DOPPLIGHT [93] is developed specifically to describe the electric and magnetic fields produced in the helical coils. In the example presented below, we consider a coil of length $L = 40$ mm, radius $a = 0.5$ mm and pitch $h = 0.35$ mm, surrounded or not by a perfectly conducting tube of internal radius $b = 0.8$ mm (i.e. $\Delta = 0.3$ mm between the HC and the conducting tube).

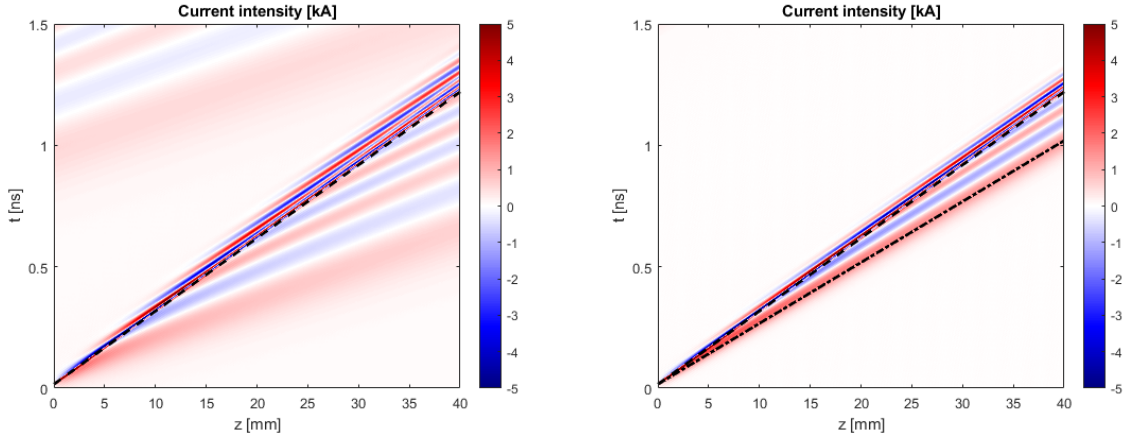

(a) (b)

Figure 5.7 – DoPPLIGHT calculation of the current pulse intensity in kA for a helical coil (a) without tube and (b) with tube as a function of time and along the HC axis. The particles features are defined in Table 2.2 for ALLS. The current is defined analytically by a Gaussian with FWHM $\tau_{FWHM} = 3$ ps and amplitude $I_0 = 7$ kA at $z = 0$ mm, delayed with respect to the particle emission by 6 ps. The HC parameters are: length $L = 40$ mm, radius of the thin cylinder $a = 0.5$ mm and step $h = 0.35$ mm with a tube of radius $b = 0.8$ mm. The dashed line corresponds to V_{HC}, the dash-dotted line corresponds to $V = 1.2\ V_{\mathrm{HC}}$.

The results of the model are shown in figures 5.7 and 5.8b. They are very similar to the PIC simulation results: we observe a similar behaviour, with a positive pulse propagating at the same constant speed $V = 1.2\ V_{\mathrm{HC}}$ with the same temporal spread by a factor of 2 and an associated amplitude reduction by the same factor as in the PIC simulations. The differences observed between DoPPLIGHT and SOPHIE are mainly due to the lack of modeling of the current reflection at the end of the coil in DoPPLIGHT. This has a negligeable impact on the proton spectrum as it is only seen by very low energy protons.

These calculations are performed for several geometries and several laser source terms and we obtain in all cases good agreement between PIC simulations and DoPPLIGHT calculations as can be seen in Appendix A. We conclude that the model is valid for this new scheme of HC with constant pitch and radius surrounded by a conducting tube.

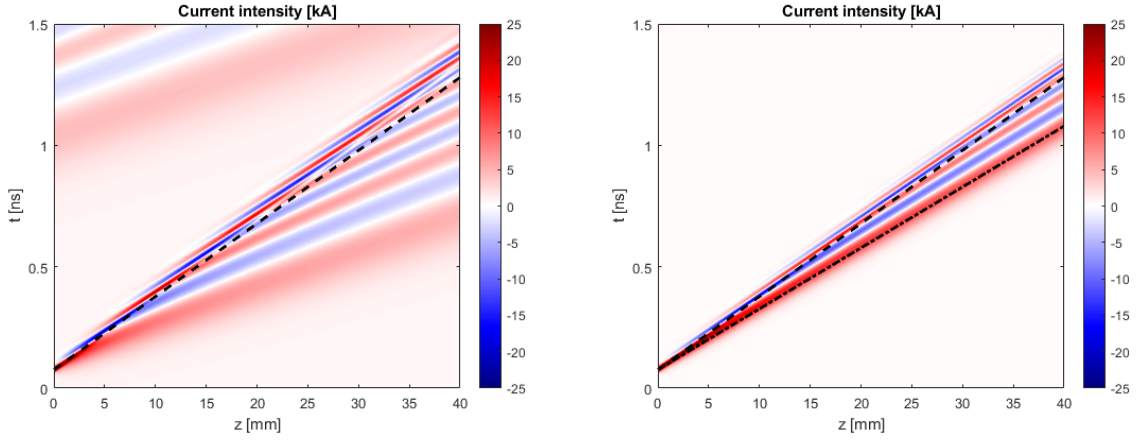

(a) (b)

Figure 5.8 – DoPPLIGHT calculation of the current pulse intensity in kA for a helical coil (a) without tube and (b) with tube as a function of time and along the HC axis. The particles features are defined in Table 2.2 for LULI2000. The current is defined analytically by a Gaussian with FWHM $\tau_{FWHM} = 8.5$ ps and amplitude $I_0 = 30$ kA at $z = 0$ mm, delayed with respect to the particule emission by 6 ps. The HC parameters are: length $L = 40$ mm, radius of the thin cylinder $a = 0.5$ mm and step $h = 0.35$ mm with a tube of radius $b = 0.8$ mm. The dashed line corresponds to V_{HC}, the dash-dotted line corresponds to $V = 1.2\ V_{\mathrm{HC}}$.

We see in Figure 5.8 that these results are also valid when the source term is changed for the one of a higher laser energy facility, similar to LULI200.

5.4 Effects of the HC with tube on the proton spectrum at the exit of the coil

Now that we observed the drastic impact of the tube on the current propagation through the helical coil, we want to see the impact of these new targets on the spectrum at the coil exit.

5.4.1 Bunching effect

We first studied the effects of the electro-magnetic fields generated by the dispersion-reduced current pulse on the particle acceleration in the HC. Figure 5.9 presents the longitudinal field along the coil axis obtained in the simulations with the PIC simulation code SOPHIE at different times. We observe, for the HC with tube, a first positive longitudinal field followed by a second negative longitudinal field. The amplitude of these fields decreases with time (by a factor 3 for the positive field), and their temporal spread increases (by a factor 1.5 for the positive field and by a factor 2 for the negative field). A modulation appears in the tail of the pulse, but there are no sign changes and no acceleration of the pulse at the front, like in the case of the HC without tube.

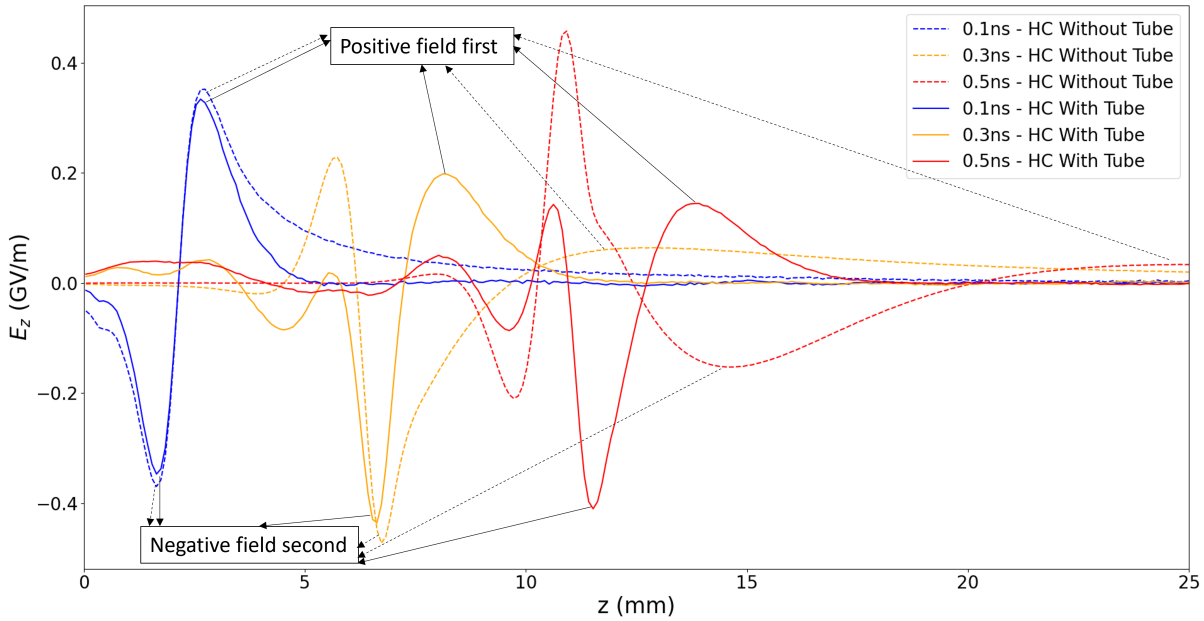

Figure 5.9 – Longitudinal electric field on the HC axis at different times, dashed lines correspond to an HC without tube, full lines to an HC with tube. The particles features set are defined in Table 2.2 for ALLS. The HC parameters are: length $L = 40$ mm, radius in the heart of the coil $a = 0.6$ mm, external radius=0.7 mm and step $h = 0.3$ mm with a tube of radius $b = 1$ mm.

This structure of fields produces two bunches of protons around the characteristic energy of the HC $E_{HC} = \frac{1}{2} m_i V_{\mathrm{HC}}^2$: one is more energetic, composed of the protons seeing the accelerating part of the field, another one is less energetic, composed of the protons under the influence of the decelerating field. It also produces a characteristic depletion zone between these two bunches, at an energy corresponding to the propagation speed of the current pulse. This feature is observed both in PIC simulations and in the reduced model DoPPLIGHT for several coil geometries with constant pitch and diameter, as can be seen in Figure 5.10.

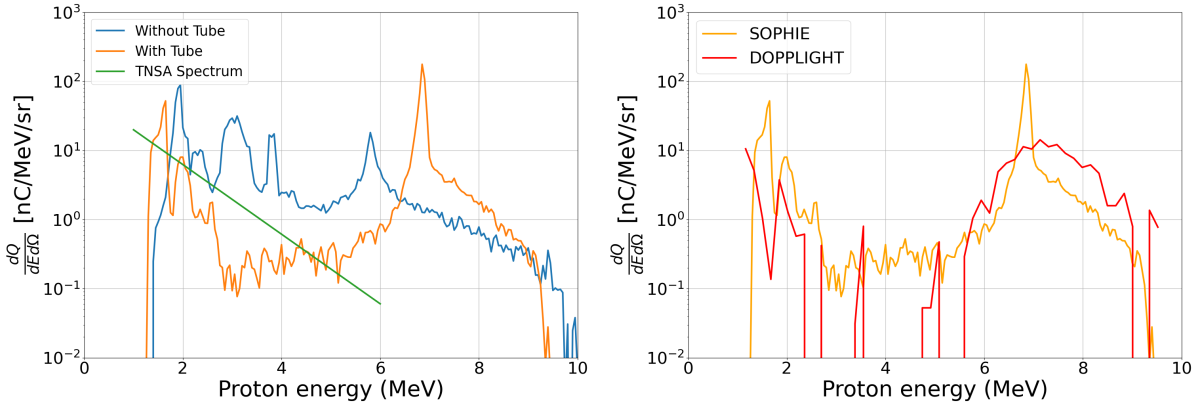

(a) (b)

Figure 5.10 – Energy spectra of accelerated protons: (A) TNSA spectrum (green line), spectrum at the exit of an HC without tube (blue line) and spectrum at the exit of an HC with tube (orange line) in PIC simulations, (B) spectrum at the exit of an HC with tube in PIC simulations (orange line) and in the numerical model DoPPLIGHT (red line). The particles features are in Table 2.2 for ALLS. The HC parameters are: length $L = 40$ mm, radius in the heart of the coil $a = 0.6$ mm, external radius=0.7 mm and step $h = 0.3$ mm with a tube of radius $b = 0.9$ mm, the HC characteristic energy is 2.9 MeV.

This shape of the spectrum of accelerated protons is significant as it shows a potential for consistent and predictable bunching of TNSA protons, possibly at high energies on facilities such as PETAL or VULCAN, already producing protons at energies of tens of MeV.

We notice that this particular scheme of HC with tube keeps the focusing effect of the HC without tube, as we observe a stronger focusing of the proton bunch in the high energy population, by a factor between 10 and 100 depending on the geometry. The focusing is in agreement with experiments [39] and with numerical simulations [39] reported in previous works.

5.4.2 Scaling of the bunching

It would be interesting to design helical coils that produce bunches at predicted energies. That is the reason why we studied the correlation of bunch energy with the HC characteristic energy that depends only on the helix geometric parameters. For that, we performed several calculations using DoPPLIGHT for different laser source terms, corresponding to ALLS and LULI2000, with radii going from $a = 0.5$ mm to $a = 0.8$ mm and pitches going from $h = 0.3$ mm to $h = 0.8$ mm, i.e. geometries that we can manufacture. In all calculations, the radius of the tube was $b = a + 0.3$ mm. We then normalised the characteristic energies of the bunches and of the depletion zone as well as the HC characteristic energy E_{HC} by the input proton spectrum cut-off energy in order to get energy scalings independent of the laser facility.

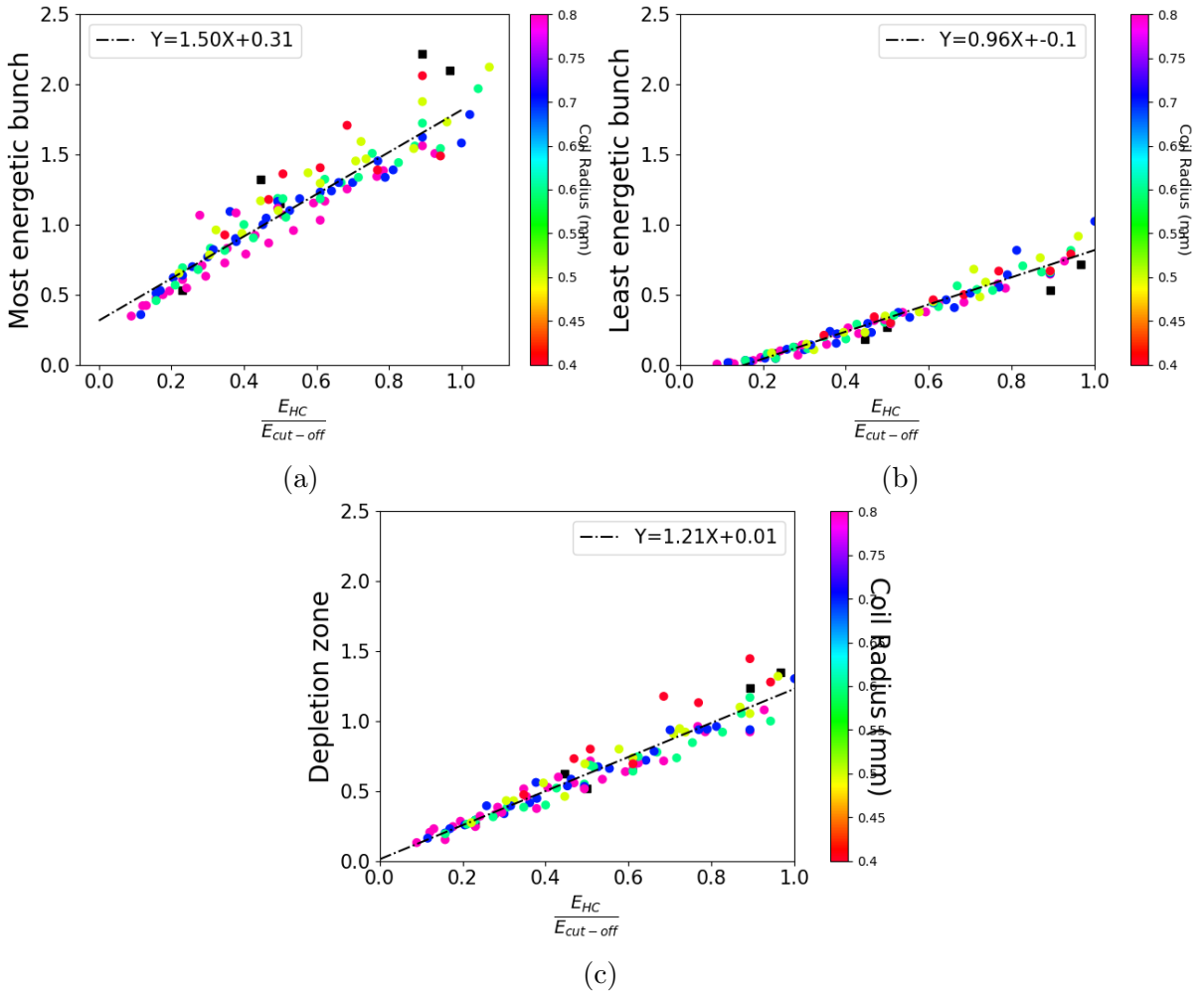

Figure 5.11 – Scaling of the energy of the bunches with respect to the HC characteristic energy normalized by the TNSA cut-off energy: (A) normalised energy of the most energetic bunch, (B) normalised energy of the least energetic bunch, (C) normalised energy of the depletion zone. Colored dots correspond to DoPPLIGHT calculations, black squares to PIC simulations. Color code shows dependence on the coil radius.

We notice that all these scalings are independent of the coil radius and only depend on the normalised HC's characteristic energy, making it the discriminatory parameter.

As shown in Figure 5.11, the normalised energy of the bunches and of the depletion zone characteristic energy depend linearly on the normalised HC characteristic energy.

The depletion zone energy corresponds to the velocity $V = 1.2\ V_{\mathrm{HC}}$, i.e. the velocity of the positive current pulse observed in previous figures, the least energetic bunch energy corresponds to $V = 1\ V_{\mathrm{HC}}$ and the most energetic bunch corresponds to $V = 1.5\ V_{\mathrm{HC}}$. These respective deceleration and acceleration are consistent with the two longitudinal fields: the one created by the positive pulse shown in Figure 5.9 and the proton space charge field, which accelerates the most energetic protons at the front and decelerates the less energetic protons at the rear.

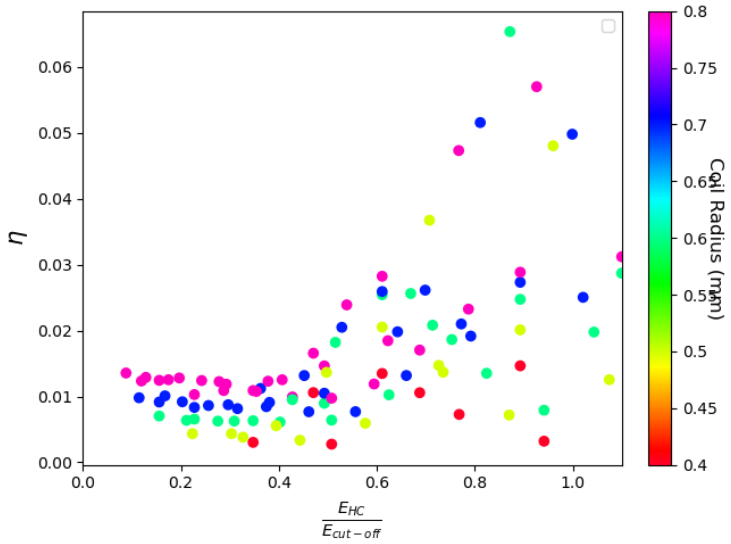

Figure 5.12 – Yield at the exit of the HC as a function of the HC characteristic energy divided by the input cut-off energy; color code shows dependence on the coil radius.

We analyzed the yield of HC with tube, that is, the ratio of the charge at the exit of HC and the charge of the input proton distribution, as a function of the HC characteristic energy normalized by the input cut-off energy and as a function of the coil radius. For $E_{\mathrm{HC}}/E_{\mathrm{cut-off}} < 0.5$ the yield is constant and only depends on the coil radius, a larger radius corresponds to a higher yield. We then see an increase to an optimal yield value for $E_{\mathrm{HC}}/E_{\mathrm{cut-off}} \approx 0.8$ before decreasing to the previous level when the pulse becomes faster than the most energetic proton and does not impact the proton population anymore.

This yield enhancement is due to the dominant space charge radial field at early times. Indeed the space charge is stronger where the proton density is higher and the unmodified TNSA proton distribution is composed mostly of low energy protons. As the HC fields are defocusing electrons from the beam and protons are spatially spread according to their energy, the radial space charge fields become dominant and proportional to the proton density. At the position of denser low energy protons, the HC field cannot compensate it even if its geometric speed is synchronised with these protons, and this leads to the loss of a large number of low energy protons at the entrance of the HC. This can be understood with Figure 5.13, where the spectrum at the exit of an HC is shown with only the space charge fields acting on the input spectrum. We see that the space charge effects strongly defocus the low energy protons, leaving only the protons of higher energy $E > 0.5E_{\mathrm{cut-off}}$ for the HC with tube to focus as the defocusing space charge they see is way lower, as seen in Figure 5.12. Therefore, to get an optimised yield, the HC characteristic energy must match with these protons of higher energy.

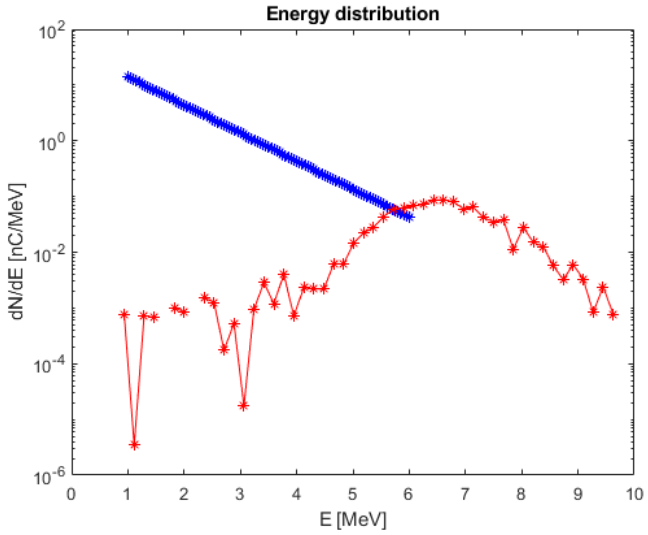

Figure 5.13 – Proton energy spectrum at $z = 40$ mm in a radius $a = 0.5$ mm calculated with DoPPLIGHT with only space charge fields (in red), for an ALLS-based input spectrum (in blue).

5.5 Conclusion and perspectives

In this chapter, I introduce a new scheme of HC targets that enables to drastically reduce the current dispersion in the coil. This scheme is simple and easy to implement experimentally as it consists of surrounding the HC by a metallic cylinder.

The reduced model DoPPLIGHT is revised in order to take into account the metallic cylinder effects. The model results are in agreement with the large-scale PIC simulations performed with the SOPHIE code.

The numerical study, on both SOPHIE and DoPPLIGHT, shows a strong effect in terms of bunching of the protons above and below the characteristic energy of the helical coil, while keeping the focusing effect on the proton beam, which was observed in previous works on regular HC targets.

Furthermore, we obtain a scaling law of the bunches energy with the HC characteristic energy, which is independent of the energy distribution of injected protons and can be used to design targets for specific energy bunches. Bunching is a feature that is interesting for applications such as isochoric proton heating, in order to heat material at specific depth, or radio-isotope production, which necessitates proton bunches at specific energies for the production of specific reactions.

In the future, HC with tube targets can be modified by introducing progressive pitches in order to increase the energy of the higher energy bunch by accelerating the longitudinal fields in synchronisation with the proton velocity.

Conclusion and perspectives

The research question I tried to answer to during the last three years of work was the following:

> Is it possible to design helical coil targets that produce proton beams with optimal features for specific applications?

Analysis of the PACMAN 2 campaign

To answer this question, my first step was to analyse the experimental campaign PACMAN 2 in Chapter 3, the first campaign to ever observe the impact of the HC geometry on the proton beam. This campaign validated the results of previous experiments, in particular in terms of focusing and spectral shaping of the proton beam. An interesting result was the experimental observation of an optimal helix diameter for the proton yield at the exit of the coil. This optimum was also confirmed by the PIC simulations performed with the code SOPHIE. The analysis of this campaign also gave evidence of the robustness of our experimental set-up to many different sources of error during the target mounting.

The analysis also shed light on the issue of the proton spectra reproducibility with the same helix geometry, which was mainly due to the shot-to-shot variation of the TNSA proton spectra on this facility. This parameter as well as the lack of resolution of the RCFs, rendered the analysis of many of the parametric variations inconclusive.

Finally, the consequent result of this chapter is the identification of two limiting factors of the yield and acceleration efficiency of the HC targets respectively: the space charge of the proton beam and the dispersion of the discharge current inside the helix. These two phenomena have been analysed in depth in the following chapters.

In order to get better experimental results, several steps shall be taken in the design of future experiments on helical coil targets. Works have to be done on the diagnostics side, with the use of a Thomson parabola [107], which would give us a proton spectrum orders of magnitude more precise as it is a continuous diagnostic. This diagnostic, only needs a very small part of the beam, and can be used simultaneously with our previous diagnostic in order to observe the transverse distribution of our proton beam with the RCF diagnostic. A second way to obtain better experimental results is to increase the statistics of our parametric study. Indeed, the PACMAN 2 campaign had very few repeated shots and its results were very sensitive to the TNSA shot-to-shot variations. By using a more stable regime of laser and by going to a facility offering possibilities for a higher shot rate coupled with an active Thomson parabola, we would be able to get statistically usable results.

Space charge of a proton beam

The ability to design new helical coil targets suited to specific applications is tied to our capacity to model correctly the physics of the post-acceleration of a proton beam inside an HC. In Chapter 4, I took the necessary steps to model the space charge forces of the proton beam inside our helix, a phenomenon we highlighted during the analysis of the PACMAN 2 campaign and which is the limiting factor of the charge yield of our post-acceleration scheme.

This work addresses the characterisation of the proton beam shape as it propagates in vacuum, both in the radial and longitudinal directions, as the space charge is dominant only in the first few tens of ps and the beam is not deformed by the helical coil field. The characterization of the beam showed a very good fit of the proton beam in the radial direction with a Gaussian distribution and two fits in the longitudinal direction. The first one is a Gaussian fit, matching well but not perfectly with the observed beam. The second fit, matching nearly perfectly, is an exponentially modified Gaussian fit. Due to time constraints and the complexity of the second fit, the modelling of the space charge field was made for a fully Gaussian beam, both in the radial and longitudinal dimension. But the modelling of the second fit will be interesting to develop to improve the model accuracy.

I then developed the space charge model for a non-relativistic proton Gaussian beam and implemented the resulting fields in our theoretical model DoPPLIGHT as a module that can be switched on and off. This space charge field is resolved in time and it is not self-consistent as to not increase the complexity of this fast calculating algorithm. It also takes into account the charge of the electrons propagating through the proton beam. We then validated this module by comparing the electromagnetic fields and the proton spectrum at the exit of the coil with the PIC code SOPHIE.

As a next step, a more accurate modeling of the space charge fields could be developed in order to calculate the space charge fields with an exponentially modified Gaussian longitudinal distribution of the proton beam.

Design of a new helical coil with controlled dispersion

The final part of my work was the design of a new scheme of helical coil targets with controlled dispersion in order to improve the acceleration and bunching efficiency of HC targets. In Chapter 5, I introduced this new scheme using a conductive tube surrounding the helix, creating a hybrid mode between a dispersive HC and a dispersionless tube. This was inspired by works done on Traveling Wave Tubes, operating as an RF amplifier.

Once the design made, I studied it with PIC simulations and the DoPPLIGHT reduced code was updated to take into account this new geometry. This study showed a strong effect on the current propagation in the helix with a reduction of the current dispersion and the appearance of a single positive pulse propagating at constant speed through the helix. This has been observed on several geometries of helix and for different source terms of discharge current, corresponding to different classes of laser pulses.

This pulse creates a characteristic longitudinal electric field in the case of an HC with a constant pitch and diameter. This longitudinal field accelerates the proton population in front of the current pulse and decelerates the proton population behind it, creating two proton bunches around the energy equivalent to the pulse propagation speed. As for the reduction of the dispersion, these bunches have been observed for several coil geometries

and different laser source terms.

I then proceeded to obtain a scaling of these bunches, using mainly our theoretical model for the bulk of the data with some large-scale PIC simulations for verification of the validity of DoPPLIGHT results. Made on a large number of geometries and for several laser source terms, we obtained scaling laws of the bunches's energy as a function of the helix characteristic energy normalised by the cut-off energy of the input TNSA spectra. These laws enable to predict the characteristics of the expected bunches on a given laser source, permitting to tune our helical coil to produce a bunch at a specific energy, which would be of interest for many applications, such as the radio-isotopes production, requiring specific energies of the proton beam in order to have the right nuclear reaction.

Further work is needed to validate this new design. Indeed, the experimental validation of the HC with tube is still to be obtained and will be the object of a 2-week experimental campaigns at INRS where we expect to observe the predicted bunches with the use of a Thomson parabola and a higher repetition rate than in our previous experiments.

General perspectives

We now know how to focus and bunch the TNSA proton beam with the use of an HC with tube, the next step will be to increase the cut-off energy and the proton yield at the exit of the HC. To go further in the study of helical coils, several approaches can be taken, some being already studied as I write these lines.

The first and most urgent perspective on the HC is the theoretical modelling of HC with varying pitch and/or diameter. It would allow the use of DoPPLIGHT to study coils where we could match the speed of the current pulse with the speed of accelerated protons, so the protons always see accelerating fields. This upgrade would enable us to design HC targets for applications needing protons of higher energies but still with a limited proton charge, such as neutron production as the cross section of spallation reactions do not evolve linearly with proton energy. Another use of varying coils to be explored would be the implementation of coils with constant characteristic velocity but varying diameter in order to maximize the proton yield at the exit of the HC. This would enable to counteract the space charge fields by giving time to the proton beam to spread and the space charge fields to become less intense than the HC fields before focusing the proton beam.

A collaboration is also being put in place at CELIA on the use of Artificial Neural Network (ANN) [108] for the design and optimisation of future HC targets. By using DoPPLIGHT to get a sufficient amount of data on numerous helix geometries then running an ANN based on variable auto-encoder (VAE) [109], [110], we should be able to have a predictive tool that can be used to optimize a helix geometry with variable pitch and diameter along its axis. The goal of this optimization will be to increase the proton post-acceleration and yield. Of course, this work depends on the previous development on the extension of DoPPLIGHT to varying geometry coils.

This work would be used to design targets for facilities with a high repetition rate where we could use a two laser set-up, one for the TNSA process and the second for the current generation inside the HC. In another direction, preliminary studies are being made on the use of gas-jet targets coupled to an HC, in order to create a high repetition rate HC target. This study is being led after the observation of discharge currents during the use of gas jet targets [111]–[113].

Furthermore, the study of the adaptability of the HC targets to other particle sources is of interest as any source combining an electric current and an ion source could be

used in cooperation with HC targets. Other laser-solid acceleration processes, such as the Radiation Pressure Acceleration (RPA) [114], are also interesting candidates for a coupling with a HC. As the RPA creates a proton beam whose divergence is very dependent on the energy [115], coupling HCs would enable a more focused and controlled RPA proton beam.

Finally, we are now at a place where we can design coils for specific experiments and not only for the study of their effect on the TNSA spectrum. A work is being done in collaboration with other teams at CELIA to create proton beams with an HC to use them in the field of proton-boron fusion reactions. In this collaboration is also studied the idea of using the HC fields to accelerate α-particles generated by laser-plasma interaction instead of protons with promising first results.

Conclusion et perspectives

La question à laquelle j'ai tenté de répondre au cours des trois dernières années de travail est la suivante :

> Est-il possible de concevoir des cibles hélicoïdales produisant des faisceaux de protons aux caractéristiques optimales pour des applications spécifiques ?

Analyse de la campagne PACMAN 2

Pour répondre à cette question, ma première étape a été d'analyser la campagne expérimentale PACMAN 2 dans le Chapitre 3, la première campagne à observer l'impact de la géométrie des HC sur le faisceau de protons. Cette campagne a validé les résultats des campagnes précédentes, en particulier en termes de focalisation et de mise en forme spectrale du faisceau de protons. Un résultat intéressant de cette expérience fut l'identification d'un diamètre optimal pour le rendement en protons à la sortie de la cible hélicoïdale. Cet optimum a aussi été confirmé par les simulations PIC effectuées avec le code SOPHIE. L'analyse de cette campagne a également mis en évidence la robustesse de notre dispositif expérimental face à de nombreuses sources d'erreur lors du montage de la cible.

L'analyse a également révélé des variations tir à tir lors de tirs sur des cibles de géométries identiques, dues à la variation tir à tir de l'installation sur les faisceaux d'ions TNSA produits. Ces variations et le manque de résolution des empilements de films radiochromiques (RCF) ont rendu l'analyse de nombreuses études paramétriques inconclusive.

Enfin, le résultat le plus important de ce chapitre est l'identification de deux facteurs limitants du rendement et de l'efficacité d'accélération et de bunching des cibles hélicoïdales, à savoir la charge d'espace du faisceau de protons et la dispersion du courant de décharge lors de sa propagation le long de l'hélice. Ces deux phénomènes ont été analysés en profondeur dans les chapitres suivants.

Afin d'obtenir de meilleurs résultats expérimentaux, plusieurs mesures doivent être prises dans la conception de futures expériences sur les cibles hélicoïdales. Des travaux doivent être réalisés du côté des diagnostics, avec l'utilisation d'une parabole de Thomson [107], qui nous donnerait un spectre de protons avec une précision supérieure d'un ordre de grandeur, car il s'agit d'un diagnostic continu. Ce diagnostic, ne nécessitant qu'une très petite partie du faisceau, peut être utilisé simultanément avec notre diagnostic précédent pour observer la distribution transverse de notre faisceau de protons à l'aide d'un diagnostic RCF. Un deuxième moyen d'obtenir de meilleurs résultats expérimentaux serait d'augmenter la statistique de notre étude paramétrique. En effet, les campagnes PACMAN 2 ont eu très peu de tirs répétés et étaient très sensibles aux variations tir à tir des faisceaux d'ions TNSA produits. En utilisant un régime laser plus stable et en se

tournant vers une installation offrant des possibilités d'un rythme de tir plus élevé couplée avec une parabole de Thomson active, nous serons en mesure d'obtenir des résultats statistiquement exploitables.

Charge d'espace d'un faisceau de protons

La capacité à concevoir de nouvelles cibles hélicoïdales adaptées à des applications spécifiques dépend de notre capacité à modéliser correctement la physique de la post-accelération d'un faisceau de protons à l'intérieur d'une HC. Dans le Chapitre 4, j'ai pris les mesures nécessaires pour modéliser la charge d'espace du faisceau de protons à l'intérieur de notre hélice, un phénomène que nous avons observé lors de l'analyse de la campagne PACMAN 2, et qui constitue le facteur limitant du rendement de notre schéma de post-accelération.

Ce travail commence par la caractérisation de la forme du faisceau de protons lorsqu'il se propage dans le vide, à la fois dans sa direction radiale et longitudinale, car la charge d'espace est dominante seulement dans les premières dizaines de ps et le faisceau n'est pas encore déformé par le champ de la cible hélicoïdale. La caractérisation du faisceau de protons a montré une très bonne adéquation entre le faisceau de protons dans la direction radiale et une distribution de charge gaussienne et deux potentielles distributions de charge dans la direction longitudinale. La première est une distribution gaussienne, qui correspond seulement de manière correcte au faisceau observé. La deuxième distribution, correspondant presque parfaitement, est une distribution gaussienne exponentiellement modifiée. En raison de la complexité de la deuxième distribution, la modélisation du champ de charge d'espace a été réalisée pour un faisceau gaussien dans les dimensions radiale et longitudinale.

J'ai ensuite développé le modèle de charge d'espace pour un faisceau gaussien de protons non relativistes et implémenté les champs calculés par celui-ci dans notre code réduit DoPPLIGHT sous forme d'un module pouvant être activé et désactivé. Ce champ de charge d'espace est résolu dans le temps et n'est pas auto-consistant, afin de ne pas augmenter la complexité de notre modèle réduit. Il tient également compte de la charge des électrons se propageant à travers le faisceau de protons. Nous avons ensuite validé ce module en comparant les champs électromagnétiques et le spectre de protons à la sortie de l'hélice avec le code PIC SOPHIE.

Comme prochaine étape, un meilleur modèle des champs de charge d'espace pourrait être développé afin de calculer les champs de charge d'espace avec une distribution longitudinale des protons modifiée de manière exponentielle.

Conception d'une nouvelle cible hélicoïdale avec dispersion contrôlée

La dernière partie de mon travail a été la conception d'un nouveau schéma de cibles hélicoïdales avec dispersion contrôlée afin d'améliorer l'efficacité de l'accélération des cibles hélicoïdales. Dans le Chapitre 5, j'ai introduit ce nouveau schéma utilisant un tube conducteur entourant l'hélice, créant un mode hybride entre une cible hélicoïdale dispersive et un tube sans dispersion. Cela a été inspiré par les tubes à ondes progressives, qui servent d'amplificateur RF dans le milieu industriel.

Une fois la conception réalisée, j'ai étudié le nouveau schéma avec des simulations PIC et le modèle réduit DoPPLIGHT a été mis à jour pour prendre en compte cette nouvelle géométrie. Cette étude a montré un fort effet sur la propagation du courant dans l'hélice avec une réduction de la dispersion du courant et l'apparition d'une seule impulsion positive se propageant à vitesse constante le long de l'hélice. Cela a été observé sur plusieurs géométries d'hélice et pour différentes sources de courant de décharge, correspondant à différentes classes de lasers.

Cette impulsion crée un champ électrique longitudinal caractéristique dans le cas d'une cible hélicoïdale avec un pas et un diamètre constants. Ce champ longitudinal accélère la population de protons devant l'impulsion de courant et décélère la population de protons derrière l'impulsion, créant deux bunchs de protons autour de l'énergie correspondant à la vitesse de propagation de l'impulsion. Comme pour la réduction de la dispersion, ces paquets ont été observés pour plusieurs géométries de cibles hélicoïdales et différentes sources laser.

J'ai ensuite procédé au calcul d'une loi d'échelle de ces bunchs, en utilisant principalement notre modèle théorique pour la majeure partie des données, avec quelques simulations PIC à grande échelle pour vérifier la validité des résultats de DoPPLIGHT. Réalisées sur un grand nombre de géométries et pour plusieurs sources laser, nous avons obtenu des lois d'échelle de l'énergie des bunchs en fonction de l'énergie caractéristique de l'hélice normalisée par l'énergie de coupure du spectre TNSA d'entrée. Ces lois nous permettent de prédire l'énergie des bunchs attendus sur une source laser donnée, ce qui nous permet de régler notre cible hélicoïdale pour obtenir un bunch à une énergie spécifique, ce qui serait intéressant pour de nombreuses applications, comme la production de radio-isotopes, nécessitant des énergies spécifiques du faisceau de protons pour obtenir la bonne réaction nucléaire.

D'autres travaux sont nécessaires pour valider cette nouvelle conception. En effet, la validation expérimentale de cibles hélicoïdales avec tube reste à obtenir et fera l'objet d'une campagne expérimentale de 2 semaines à l'INRS, où nous nous attendons à observer les bunchs prédits grâce à l'utilisation d'une parabole de Thomson et un rythme de tir plus élevé que lors de nos expériences précédentes.

Perspectives générales

Nous savons maintenant comment focaliser et buncher le faisceau de protons TNSA à l'aide de cibles hélicoïdales avec tube. La prochaine étape sera d'améliorer l'énergie de coupure et le rendement en protons à la sortie de l'hélice. Pour approfondir l'étude des cibles hélicoïdales, plusieurs approches peuvent être envisagées, certaines étant déjà à l'étude à l'heure où j'écris ces lignes.

La première perspective concerne la modélisation théorique des HC avec un pas et/ou un diamètre variables. Cela nous permettrait d'utiliser DoPPLIGHT pour étudier des bobines où nous pourrions faire correspondre la vitesse de l'impulsion de courant avec la vitesse des protons accélérés, de sorte que les protons voient toujours des champs accélérateurs. Cette amélioration nous permettrait de concevoir des cibles HC pour des applications nécessitant des protons de plus haute énergie, mais avec une charge en protons limitée, comme la production de neutrons, car la section efficace des réactions de spallation n'évolue pas linéairement avec l'énergie des protons. Une autre utilisation des HC variables à explorer serait la mise en place de bobines avec une vitesse caractéristique constante mais un diamètre variable afin de maximiser le rendement en protons à la sortie du HC. Cela

permettrait de contrer les champs de charge d'espace en donnant du temps au faisceau de protons pour se disperser et aux champs de charge d'espace de devenir moins intenses que les champs du HC avant de focaliser le faisceau de protons.

Une collaboration est également en cours au CELIA sur l'utilisation de réseaux de neurones artificiels (RNA) [108] pour la conception et l'optimisation des futures cibles HC. En utilisant DoPPLIGHT pour obtenir une quantité suffisante de données sur de nombreuses géométries d'hélices, puis en exécutant un RNA basé sur un auto-encodeur variable (VAE) [109], [110], nous disposerons d'un outil prédictif qui pourra être utilisé pour optimiser une géométrie hélicoïdale avec un pas et un diamètre variables le long de son axe. L'objectif de cette optimisation sera d'augmenter la post-accélération et le rendement en protons. Bien entendu, ce travail dépend du développement précédent de l'extension de DoPPLIGHT aux cibles hélicoïdales variables.

Ce travail serait utilisé pour concevoir des cibles pour des installations à haut taux de répétition où nous pourrions utiliser un set-up à deux lasers, l'un pour le processus TNSA et l'autre pour la génération de courant à l'intérieur de l'hélice. Dans une autre direction, des études préliminaires sont en cours sur l'utilisation de cibles à jet de gaz couplées à une cible hélicoïdale, afin de créer une HC à haut taux de répétition. Cette étude est menée suite à l'observation de courants de décharge lors de l'utilisation de cibles à jet de gaz [111]-[113].

De plus, l'étude de l'adaptabilité des cibles HC à d'autres sources de particules est intéressante, car toute source combinant un courant électrique et une source d'ions pourrait être utilisée en coopération avec les cibles hélicoïdales. D'autres processus d'accélération laser-solide, tels que l'accélération par pression de radiation (RPA) [114], sont également des candidats intéressants pour un couplage avec un HC. Comme le RPA crée un faisceau de protons dont la divergence dépend fortement de l'énergie [115], le couplage avec un HC permettrait d'obtenir un faisceau de protons RPA plus focalisé et contrôlé.

Enfin, nous en sommes maintenant à un stade où nous pouvons concevoir des bobines pour des expériences spécifiques et non seulement pour l'étude de leur effet sur le spectre TNSA. Un travail est en cours en collaboration avec d'autres équipes du CELIA pour créer des faisceaux de protons avec un HC afin de les utiliser dans le domaine des réactions de fusion proton-bore. Dans le cadre de cette collaboration, l'idée d'utiliser les champs du HC pour accélérer des particules α générées par l'interaction laser-plasma au lieu de protons est également à l'étude avec de premiers résultats encourageants.

Résumé en français

Pour des raisons de collaborations internationales avec la co-tutelle de la thèse de Clément Lacoste avec l'INRS-EMT au Canada, ainsi que la présence de membres non-francophones dans mon jury, ce manuscrit a été rédigé en anglais et non en français. Pour la compréhension de mon travail par un plus grand nombre, l'introduction et la conclusion générale ont été traduites en français et cette section introduit un résumé substantiel du contenu de mon manuscrit.

Contexte Théorique

Dans le Chapitre 1, j'ai présenté les concepts théoriques essentiels pour comprendre les phénomènes physiques ayant lieu au coeur des cibles hélicoïdales.

J'ai pour cela d'abord introduit les bases des notions de l'interaction laser-plasma relativistes nécessaires pour comprendre l'accélération d'ions par le processus de Target Normal Sheath Acceleration (TNSA), processus source des protons accélérés tout du long de ce manuscrit.

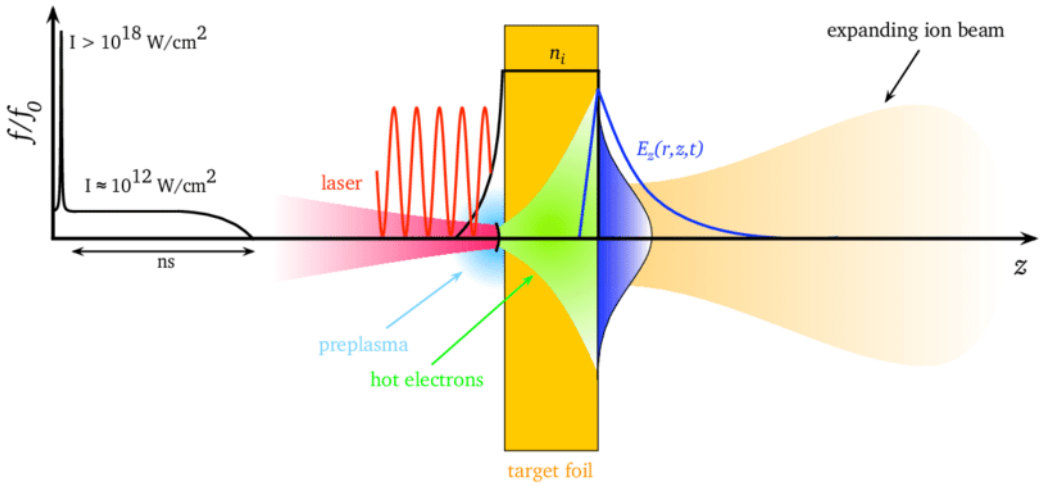

FIGURE 1 – Schéma du procédé d'accélération d'ions Target Normal Sheath Acceleration [56].

J'ai ensuite rapidement décrit la charge d'espace d'un faisceau continu de particules chargées et son effet sur la dynamique des particules du faisceau.

Enfin, j'ai décrit les effets physiques de la propagation d'un courant transitoire le long d'une hélice, source des champs électromagnétiques au coeur de la cible hélicoïdale qui nous servent à post-accélérer, focaliser et buncher le faisceau de protons TNSA

L'ensemble des notions introduites dans ce chapitre, de l'interaction laser-plasma relativiste à la génération des champs électromagnétiques au sein d'une hélice nous permettent donc de comprendre le fonctionnement des cibles hélicoïdales étudiées et d'aborder le travail présenté dans ce manuscrit.

Moyens et Méthodes

Dans le chapitre 2, j'ai introduit les outils expérimentaux et numériques qui ont été essentiels pour mon travail durant mes trois années de thèse.

J'ai présenté les outils numériques utilisés tout au long de mon travail, à la fois pour l'analyse expérimentale et la compréhension théorique de la physique des cibles hélicoïdales. Premièrement, j'ai présenté de manière rapide les codes Particle-In-Cell (PIC), avant de présenter les spécificités du code PIC utilisé durant ces trois années de thèse : SOPHIE, code développé au CEA-CESTA par Olivier Cessenat.

J'ai aussi décrit le code théorique DoPPLIGHT (Dynamics of Particles Produced by Laser Interaction in Grounded Helical Targets) développé par notre équipe autour des équations de Pierce, Kino et Paik présentées au chapitre précédent. Ce code nous permet d'obtenir en quelques minutes sur un ordinateur personnel des spectres protoniques en sortie de cibles hélicoïdales comparables à ceux obtenus lors de calculs longs de plusieurs heures.processeurs sur un super-calculateur via le code SOPHIE.

J'ai enfin donné les paramètres numériques utilisés lors des simulations SOPHIE et de calculs DoPPLIGHT durant mon travail des dernières années.

Tous ces outils seront utilisés dans les chapitres suivants, à commencer par le Chapitre 3 dont le but est l'analyse de la campagne PACMAN 2, en particulier les variations paramétriques de la géométrie des cibles hélicoïdales et de leur impact sur le faisceau de protons.

Analyse de la campagne expérimentale PACMAN 2

L'objectif du Chapitre 3 était d'observer l'impact sur le faisceau de protons TNSA des variations paramétriques sur des cibles hélicoïdales, ce qui était le but de la campagne PACMAN 2.

J'ai tout d'abord introduit la configuration expérimentale de l'expérience PACMAN 2 que j'ai analysée avant de parler en détail du traitement des films radiochromiques (RCF), seul diagnostic sur la campagne PACMAN 2 nous permettant d'obtenir les spectres en énergie des protons obtenus lors des tirs de cette campagne.

J'ai ensuite étudié l'impact de la variation du diamètre des cibles hélicoïdales, car un diamètre plus grand augmente le nombre de protons injectés dans le ressort mais réduit l'intensité des champs à l'intérieur de la bobine. J'ai ensuite mené une étude sur l'influence de la longueur des cibles hélicoïdales : en effet, une particule chargée passant plus de temps dans un champ accélérant sera plus énergétique à la fin de la bobine. Enfin, j'ai étudié l'impact des pas progressifs des cibles hélicoïdales, afin de synchroniser les champs accélérateurs avec les protons accélérés par les champs du ressort.

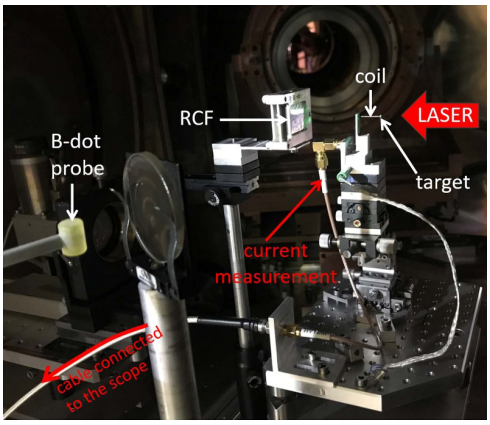

FIGURE 2 – Installation expérimentale pour la campagne PACMAN 2.

Dans ce chapitre, j'ai donc présenté les résultats expérimentaux et de simulation de l'étude paramétrique de la géométrie des cibles hélicoïdales menée sur l'installation LULI2000 [40] lors de la campagne PACMAN 2 en février 2020. L'objectif de cette campagne expérimentale était d'obtenir des lois d'échelle sur les paramètres de géométrie de l'hélice. Ce travail était motivé par la nécessité d'optimiser les futures cibles hélicoïdales pour différentes applications. Ce n'est pas un travail trivial car le diamètre et le pas de l'hélice ne sont pas des variables indépendantes lorsqu'il s'agit de calculer la vitesse géométrique de l'impulsion de courant à l'intérieur de l'hélice et les champs générés par la propagation de cette impulsion.

Tout d'abord, j'ai montré les limitations expérimentales de la campagne PACMAN 2 : la variation d'un tir à l'autre observée sur des cibles hélicoïdales identiques, due à la variation d'un tir à l'autre du processus TNSA sur LULI2000, ainsi que le manque de résolution sur les films radiographiques limitant l'analyse.

J'ai ensuite montré les effets de la géométrie de la cible hélicoïdale sur le faisceau TNSA, en particulier l'existence d'une fluence maximale à un diamètre optimal, observée à la fois expérimentalement et lors de simulations PIC à grande échelle.

Enfin, les deux principales limitations observées lors de cette étude de l'effet des cibles hélicoïdales sur le faisceau de protons sont : la présence d'un fort champ de charge d'espace de défocalisation aux temps initiaux, limitant le rendement des cibles hélicoïdales, et la nature dispersive des cibles hélicoïdales créant une alternance de champs accélérateurs et décélérateurs, limitant l'énergie de coupure du spectre des protons.

Pour étudier les cibles de bobines hélicoïdales et leur impact sur un faisceau de protons TNSA, nous devons développer et mettre en œuvre dans DoPPLIGHT une modélisation de la charge d'espace des protons, un effet identifié à partir des résultats expérimentaux et de l'étude par simulation PIC.

Modélisation de la charge d'espace d'un faisceau de protons dans une cible hélicoïdale

L'objectif du Chapitre 4 était de modéliser les effets de la charge d'espace produite par le faisceau de protons à l'intérieur d'une cible hélicoïdale, comme observé dans le Chapitre 3. Le but était d'implémenter cette modélisation dans notre modèle théorique DoPPLIGHT sans augmenter la complexité du modèle, afin de conserver le gain de temps

par rapport aux simulations PIC à grande échelle. Pour ce faire, j'ai d'abord caractérisé la forme du faisceau de protons TNSA, afin d'adapter notre théorie aux paramètres physiques de notre faisceau. Ensuite, j'ai développé une théorie en 3D axisymétrique de la charge d'espace d'un paquet de protons gaussien non relativistes. Enfin, cette théorie a été implémentée dans DoPPLIGHT, un modèle théorique à résolution temporelle et non auto-consistant de la propagation du faisceau de protons à travers une cible hélicoïdale.

Dans ce chapitre, j'ai présenté le travail réalisé sur la caractérisation et la modélisation électromagnétique du faisceau de protons TNSA observé dans le chapitre précédent. Ce champ de charge d'espace est l'une des raisons du faible rendement des cibles hélicoïdales, comme présenté dans le Chapitre 3. La motivation derrière ce travail était d'avoir un modèle de charge d'espace dans notre code théorique DoPPLIGHT fournissant des résultats proches des simulations PIC à grande échelle, afin d'utiliser ce code pour la conception future de cibles hélicoïdales.

Dans ce chapitre, en utilisant des simulations PIC à grande échelle, j'ai d'abord caractérisé la forme d'un faisceau de protons TNSA dans ses dimensions longitudinale et radiale. Nous avons observé qu'une densité de charge gaussienne était une bonne approximation de la forme de notre faisceau de protons TNSA à la fois dans sa dimension radiale et dans sa dimension longitudinale.

Cela a permis le calcul des champs de charge d'espace d'un faisceau de protons gaussien non relativiste, équivalent à notre faisceau TNSA se propageant dans le vide pendant le premier moment de la propagation à travers la cible hélicoïdale.

Enfin, nous avons pu intégrer la physique de la charge d'espace des protons à l'intérieur de la cible hélicoïdale dans DoPPLIGHT sans augmenter la complexité de notre modèle théorique. Il tient également compte des effets de la cible TNSA sur les champs électriques ainsi que de la déneutralisation progressive de notre faisceau de protons TNSA lors de sa progression à travers le ressort.

Avec ce nouveau module implémenté dans DoPPLIGHT, nous disposons maintenant d'un modèle rapide, efficace et précis pour simuler la dynamique des protons à l'intérieur des cibles hélicoïdales, ce qui nous permet d'optimiser les performances des cibles hélicoïdales en termes de focalisation, post-accélération, groupement et rendement.

Conception d'une nouvelle cible hélicoïdale avec contrôle de la dispersion

Le Chapitre 5 avait pour objectif de présenter une nouvelle conception de cible hélicoïdale avec une dispersion contrôlée. Ce nouveau schéma avait pour but de pallier l'effet limitant de la dispersion sur l'énergie de coupure et le bunching observé dans le Chapitre 3. Pour cela, j'ai d'abord développé un nouveau schéma de cible hélicoïdale avec un tube afin de réduire la dispersion du courant à travers la cible hélicoïdale. J'ai ensuite développé une théorie de la propagation du courant et des champs électromagnétiques pour mettre à jour notre modèle théorique DoPPLIGHT. Nous l'avons ensuite implémenté dans DoPPLIGHT afin d'étudier l'impact de ce nouveau schéma sur un faisceau de protons TNSA.

Dans ce chapitre, j'ai présenté le schéma de développement de la nouvelle cible hélicoïdale avec tube que j'ai conçue pour réduire la dispersion à l'intérieur de l'hélice. Nous l'avons étudié à travers des simulations PIC avec le code SOPHIE et avons développé un modèle théorique que nous avons validé par comparaison avec les simulations PIC à

grande échelle, et nous l'avons implémenté dans DoPPLIGHT. La motivation derrière ce chapitre découle des résultats expérimentaux présentés dans le Chapitre 3, où j'ai montré les limitations expérimentales en matière de bunching et d'énergie de coupure maximale dues à la dispersion du courant à travers la cible hélicoïdale.

Ce nouveau schéma de cibles hélicoïdales avec tube permet de réduire considérablement la dispersion du courant dans la bobine. Ce schéma est simple et relativement facile à mettre en œuvre expérimentalement, car il consiste à entourer la cible hélicoïdale d'un cylindre métallique.

Le modèle simplifié DoPPLIGHT a été révisé afin de prendre en compte les effets du cylindre métallique. Les résultats du modèle concordent avec les simulations PIC à grande échelle réalisées avec le code SOPHIE.

L'étude numérique, à la fois avec SOPHIE et DoPPLIGHT, montre un fort effet en termes de bunching des protons au-dessus et en dessous de l'énergie caractéristique de la cible hélicoïdale, tout en maintenant l'effet de focalisation sur le faisceau de protons, qui avait été observé dans des travaux précédents sur les cibles hélicoïdales classiques.

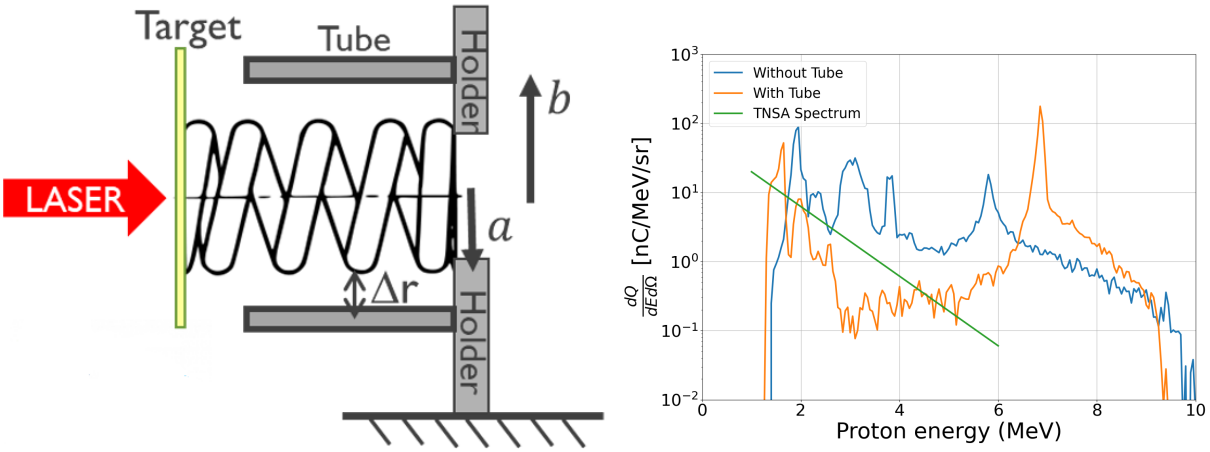

(a) (b)

FIGURE 3 – (A) Schéma d'une cible hélicoïdale avec tube et (B) spectres de protons simulés par simulation PIC : TNSA en entrée de cible hélicoïdale (ligne verte), en sortie de cible hélicoïdale sans tube (ligne bleue), en sortie de cible hélicoïdale avec tube (ligne orange).

De plus, nous obtenons une loi d'échelle de l'énergie des paquets de protons en fonction de l'énergie caractéristique de la cible hélicoïdale, qui est indépendante de la distribution en énergie des protons injectés et peut être utilisée pour concevoir des cibles pour des paquets de protons d'énergie spécifiques. Le bunching est une caractéristique intéressante pour des applications telles que le chauffage isochore des protons, afin de chauffer un matériau à une profondeur spécifique, ou la production de radio-isotopes, qui nécessite des paquets de protons à des énergies spécifiques pour la réalisation de réactions nucléaires spécifiques.

À l'avenir, les cibles hélicoïdales avec tube pourraient être modifiées en introduisant des pas progressifs afin d'augmenter l'énergie de coupure des protons en accélérant les champs longitudinaux en synchronisation avec la vitesse des protons.

Bibliography

[1] E. O. Lawrence and M. S. Livingston, « The production of high speed light ions without the use of high voltages », *Physical Review*, vol. 40, no. 1, p. 19, 1932.

[2] J. D. Cockcroft and E. T. Walton, « Experiments with high velocity positive ions.—(i) further developments in the method of obtaining high velocity positive ions », *Proceedings of the royal society of London. Series A, containing papers of a mathematical and physical character*, vol. 136, no. 830, pp. 619–630, 1932.

[3] T. Tajima and J. Dawson, « Laser electron accelerator », *Phys. Rev. Lett.*, no. 43, pp. 267–270, 1979.

[4] D. Strickland and G. Mourou, « Compression of amplified chirped optical pulses », *Optics communications*, vol. 55, no. 6, pp. 447–449, 1985.

[5] R. Assmann, J. Grebenyuk, *et al.*, « Accelerator physics challenges towards a plasma accelerator with usable beam quality », *Proceedings of IPAC, Germany, Dresden*, pp. 961–964, 2014.

[6] A. Modena, Z. Najmudin, A. Dangor, *et al.*, « Electron acceleration from the breaking of relativistic plasma waves », *nature*, vol. 377, no. 6550, pp. 606–608, 1995.

[7] H. Daido, M. Nishiuchi, and A. S. Pirozhkov, « Review of laser-driven ion sources and their applications », *Reports on progress in physics*, vol. 75, no. 5, p. 056 401, 2012.

[8] A. Macchi, M. Borghesi, and M. Passoni, « Ion acceleration by superintense laser-plasma interaction », *Reviews of Modern Physics*, vol. 85, no. 2, p. 751, 2013.

[9] J. Fuchs, P. Antici, E. d'Humières, *et al.*, « Laser-driven proton scaling laws and new paths towards energy increase », *Nature physics*, vol. 2, no. 1, pp. 48–54, 2006.

[10] P. Patel, A. Mackinnon, M. Key, *et al.*, « Isochoric heating of solid-density matter with an ultrafast proton beam », *Physical review letters*, vol. 91, no. 12, p. 125 004, 2003.

[11] K. Nemoto, A. Maksimchuk, S. Banerjee, *et al.*, « Laser-triggered ion acceleration and table top isotope production », *Applied Physics Letters*, vol. 78, no. 5, pp. 595–597, 2001.

[12] K. Lancaster, S. Karsch, H. Habara, *et al.*, « Characterization of 7 li (p, n) 7 be neutron yields from laser produced ion beams for fast neutron radiography », *Physics of plasmas*, vol. 11, no. 7, pp. 3404–3408, 2004.

[13] M. Roth, T. Cowan, M. Key, *et al.*, « Fast ignition by intense laser-accelerated proton beams », *Physical review letters*, vol. 86, no. 3, p. 436, 2001.

[14] V. Y. Bychenkov, W. Rozmus, A. Maksimchuk, D. Umstadter, and C. Capjack, « Fast ignitor concept with light ions », *Plasma Physics Reports*, vol. 27, pp. 1017–1020, 2001.

[15] M. Borghesi, A. Schiavi, D. Campbell, *et al.*, « Proton imaging: a diagnostic for inertial confinement fusion/fast ignitor studies », *Plasma physics and controlled fusion*, vol. 43, no. 12A, A267, 2001.

[16] M. Borghesi, L. Romagnani, A. Schiavi, *et al.*, « Measurement of highly transient electrical charging following high-intensity laser–solid interaction », *Applied Physics Letters*, vol. 82, no. 10, pp. 1529–1531, 2003.

[17] M. Roth, A. Blazevic, M. Geissel, *et al.*, « Energetic ions generated by laser pulses: a detailed study on target properties », *Physical Review Special Topics-Accelerators and Beams*, vol. 5, no. 6, p. 061 301, 2002.

[18] M. Borghesi, A. Mackinnon, D. H. Campbell, *et al.*, « Multi-mev proton source investigations in ultraintense laser-foil interactions », *Physical Review Letters*, vol. 92, no. 5, p. 055 003, 2004.

[19] T. Cowan, J. Fuchs, H. Ruhl, *et al.*, « Ultralow emittance, multi-mev proton beams from a laser virtual-cathode plasma accelerator », *Physical review letters*, vol. 92, no. 20, p. 204 801, 2004.

[20] R. Snavely, M. Key, S. Hatchett, *et al.*, « Intense high-energy proton beams from petawatt-laser irradiation of solids », *Physical review letters*, vol. 85, no. 14, p. 2945, 2000.

[21] S. Wilks, A. Langdon, T. Cowan, *et al.*, « Energetic proton generation in ultra-intense laser–solid interactions », *Physics of plasmas*, vol. 8, no. 2, pp. 542–549, 2001.

[22] Y. Sentoku, T. Cowan, A. Kemp, and H. Ruhl, « High energy proton acceleration in interaction of short laser pulse with dense plasma target », *Physics of plasmas*, vol. 10, no. 5, pp. 2009–2015, 2003.

[23] T. Schlegel, N. Naumova, V. Tikhonchuk, C. Labaune, I. Sokolov, and G. Mourou, « Relativistic laser piston model: ponderomotive ion acceleration in dense plasmas using ultraintense laser pulses », *Physics of Plasmas*, vol. 16, no. 8, p. 083 103, 2009.

[24] S. Martins, R. Fonseca, L. Silva, and W. B. Mori, « Ion dynamics and acceleration in relativistic shocks », *The Astrophysical Journal*, vol. 695, no. 2, p. L189, 2009.

[25] T. Yang, H. Cheng, Y. Yan, *et al.*, « Designing of active plasma lens for focusing laser-plasma-accelerated pulsed proton beams », *Physical Review Accelerators and Beams*, vol. 24, no. 3, p. 031 301, 2021.

[26] P. Ni, B. Logan, S. Lund, *et al.*, « Feasibility study of the magnetic beam self-focusing phenomenon in a stack of conducting foils: application to tnsa proton beams », *Laser and Particle Beams*, vol. 31, no. 1, pp. 81–88, 2013.

[27] C. McGuffey, J. Kim, M. Wei, *et al.*, « Focussing protons from a kilojoule laser for intense beam heating using proximal target structures », *Scientific reports*, vol. 10, no. 1, pp. 1–10, 2020.

[28] J. Bin, A. Lei, L. Cao, *et al.*, « Influence of the target front-surface curvature on proton acceleration in laser-foil interaction », *Physics of Plasmas*, vol. 16, no. 4, p. 043 109, 2009.

[29] M. Carrié and E. Lefebvre, « Focusing of laser-accelerated proton beams using curved targets, and improved energy deposition », *High Energy Density Physics*, vol. 7, no. 4, pp. 353–360, 2011.

[30] T. Bartal, M. E. Foord, C. Bellei, *et al.*, « Focusing of short-pulse high-intensity laser-accelerated proton beams », *Nature Physics*, vol. 8, no. 2, pp. 139–142, 2012.

[31] B. Qiao, M. Foord, M. Wei, *et al.*, « Dynamics of high-energy proton beam acceleration and focusing from hemisphere-cone targets by high-intensity lasers », *Physical Review E*, vol. 87, no. 1, p. 013 108, 2013.

[32] M. G. Zakova, J. Psikal, F. Schillaci, and D. Margarone, « Improving laser-accelerated proton beam divergence by electric and magnetic fields induced in flat channel-like targets », *Plasma Physics and Controlled Fusion*, vol. 63, no. 8, p. 085 005, 2021.

[33] T. Toncian, M. Borghesi, J. Fuchs, *et al.*, « Ultrafast laser-driven microlens to focus and energy-select mega-electron volt protons », *Science*, vol. 312, no. 5772, pp. 410–413, 2006.

[34] K. Harres, I. Alber, A. Tauschwitz, *et al.*, « Beam collimation and transport of quasineutral laser-accelerated protons by a solenoid field », *Physics of Plasmas*, vol. 17, no. 2, p. 023 107, 2010.

[35] V. Kaymak, E. Aktan, M. Cerchez, *et al.*, « Boosted acceleration of protons by tailored ultra-thin foil targets », *Scientific reports*, vol. 9, no. 1, p. 18 672, 2019.

[36] L. Giuffrida, K. Svensson, J. Psikal, *et al.*, « Manipulation of laser-accelerated proton beam profiles by nanostructured and microstructured targets », *Physical Review Accelerators and Beams*, vol. 20, no. 8, p. 081 301, 2017.

[37] S. Kar, H. Ahmed, R. Prasad, *et al.*, « Guided post-acceleration of laser-driven ions by a miniature modular structure », *Nature communications*, vol. 7, no. 1, pp. 1–7, 2016.

[38] M. Cerchez, R. Prasad, B. Aurand, *et al.*, « Arcturus laser: a versatile high-contrast, high-power multi-beam laser system », *High Power Laser Science and Engineering*, vol. 7, e37, 2019.

[39] M. Bardon, J. Moreau, L. Romagnani, *et al.*, « Physics of chromatic focusing, post-acceleration and bunching of laser-driven proton beams in helical coil targets », *Plasma Physics and Controlled Fusion*, vol. 62, no. 12, p. 125 019, 2020.

[40] *Laboratoire pour l'Utilisation des Lasers Intenses. LULI200*, https://portail.polytechnique.edu/luli/fr/installations/luli2000.

[41] J. W. Yoon, Y. G. Kim, I. W. Choi, *et al.*, « Realization of laser intensity over 10 23 w/cm 2 », *Optica*, vol. 8, no. 5, pp. 630–635, 2021.

[42] L. L. N. Laboratory. (1995), [Online]. Available: http://www.llnl.gov/str/Petawatt.html.

[43] J. Bonvalet, « Optimisation de l'accélération d'ions par choc électrostatique dans un jet de gaz et application à la production de radioisotopes », Theses, Université de Bordeaux, Mar. 2022. [Online]. Available: https://theses.hal.science/tel-03772538.

[44] S. Carrier-Vallieres, « Towards reliable, intense and high repetition-rate laser-driven ion beamlines », Theses, Université de Bordeaux ; Institut national de la recherche scientifique (Québec, province), Dec. 2020. [Online]. Available: https://theses.hal.science/tel-03149754.

[45] V. Ospina-Bohórquez, « Ion acceleration from high-intensity laser interactions with quasi-critical-gas targets : experiments and numerical simulations », Theses, Université de Bordeaux ; Universidad de Salamanca (Espagne). Facultad de ciencias, Dec. 2022. [Online]. Available: https://theses.hal.science/tel-04011154.

[46] M. Göppert-Mayer, « Über elementarakte mit zwei quantensprüngen », *Annalen der Physik*, vol. 401, no. 3, pp. 273–294, 1931.

[47] M. V. Ammosov, N. B. Delone, and V. P. Krainov, « Tunnel ionization of complex atoms and of atomic ions in an alternating electromagnetic field », *Soviet Journal of Experimental and Theoretical Physics*, vol. 64, no. 6, p. 1191, 1986.

[48] P. Gibbon, *Short pulse laser interactions with matter: an introduction*. World Scientific, 2005.

[49] J. L. Hansen, « Imaging molecular frame dynamics using spatially oriented molecules », Ph.D. dissertation, 2012.

[50] E. Clark, K. Krushelnick, M. Zepf, *et al.*, « Energetic heavy-ion and proton generation from ultraintense laser-plasma interactions with solids », *Physical Review Letters*, vol. 85, no. 8, p. 1654, 2000.

[51] A. Mackinnon, Y. Sentoku, P. Patel, *et al.*, « Enhancement of proton acceleration by hot-electron recirculation in thin foils irradiated by ultraintense laser pulses », *Physical review letters*, vol. 88, no. 21, p. 215 006, 2002.

[52] A. Link, R. R. Freeman, D. Schumacher, and L. Van Woerkom, « Effects of target charging and ion emission on the energy spectrum of emitted electrons », *Physics of Plasmas*, vol. 18, no. 5, 2011.

[53] R. Nuter, L. Gremillet, E. Lefebvre, A. Lévy, T. Ceccotti, and P. Martin, « Field ionization model implemented in particle in cell code and applied to laser-accelerated carbon ions », *Physics of Plasmas*, vol. 18, no. 3, 2011.

[54] S. Gitomer, R. Jones, F. Begay, A. Ehler, J. Kephart, and R. Kristal, « Fast ions and hot electrons in the laser–plasma interaction », *The Physics of fluids*, vol. 29, no. 8, pp. 2679–2688, 1986.

[55] M. Hegelich, S. Karsch, G. Pretzler, *et al.*, « Mev ion jets from short-pulse-laser interaction with thin foils », *Physical review letters*, vol. 89, no. 8, p. 085 002, 2002.

[56] M. Roth and M. Schollmeier, « Ion acceleration-target normal sheath acceleration », *arXiv preprint arXiv:1705.10569*, 2017.

[57] F. Brunel, « Not-so-resonant, resonant absorption », *Physical review letters*, vol. 59, no. 1, p. 52, 1987.

[58] E. S. Weibel, « Anomalous skin effect in a plasma », *The Physics of Fluids*, vol. 10, no. 4, pp. 741–748, 1967.

[59] E. Gamalii and V. Tikhonchuk, « Effect of intense ultrashort light pulses on a substance », *JETP Lett*, vol. 48, no. 8, 1988.

[60] V. L. Ginzburg, « The propagation of electromagnetic waves in plasmas », *International Series of Monographs in Electromagnetic Waves*, 1970.

[61] W. L. Kruer, *The physics of laser plasma interaction*, 1988.

[62] P. Catto and R. M. More, « Sheath inverse bremsstrahlung in laser produced plasmas », *The Physics of Fluids*, vol. 20, no. 4, pp. 704–705, 1977.

[63] J. Mendonça, « Threshold for electron heating by two electromagnetic waves », *Physical Review A*, vol. 28, no. 6, p. 3592, 1983.

[64] Z.-M. Sheng, K. Mima, Y. Sentoku, *et al.*, « Stochastic heating and acceleration of electrons in colliding laser fields in plasma », *Physical review letters*, vol. 88, no. 5, p. 055 004, 2002.

[65] A. Bourdier, D. Patin, and E. Lefebvre, « Stochastic heating in ultra high intensity laser-plasma interaction », *Laser and Particle Beams*, vol. 25, no. 1, pp. 169–180, 2007.

[66] W. L. Kruer and K. Estabrook, « J× b heating by very intense laser light », *The Physics of fluids*, vol. 28, no. 1, pp. 430–432, 1985.

[67] S. Wilks, W. Kruer, M. Tabak, and A. Langdon, « Absorption of ultra-intense laser pulses », *Physical review letters*, vol. 69, no. 9, p. 1383, 1992.

[68] G. Malka and J. Miquel, « Experimental confirmation of ponderomotive-force electrons produced by an ultrarelativistic laser pulse on a solid target », *Physical review letters*, vol. 77, no. 1, p. 75, 1996.

[69] A. Debayle, J. J. Honrubia, E. d'Humières, and V. T. Tikhonchuk, « Divergence of laser-driven relativistic electron beams », *Phys. Rev. E*, vol. 82, p. 036 405, 3 Sep. 2010.

[70] A. Macchi, *A superintense laser-plasma interaction theory primer*. Springer Science & Business Media, 2013.

[71] S. Wilks, A. Langdon, T. Cowan, *et al.*, « Energetic proton generation in ultra-intense laser–solid interactions », *Physics of plasmas*, vol. 8, no. 2, pp. 542–549, 2001.

[72] P. Mora, « Plasma expansion into a vacuum », *Physical Review Letters*, vol. 90, no. 18, p. 185 002, 2003.

[73] J. Badziak, E. Woryna, P. Parys, *et al.*, « Fast proton generation from ultrashort laser pulse interaction with double-layer foil targets », *Physical Review Letters*, vol. 87, no. 21, p. 215 001, 2001.

[74] T. Z. Esirkepov, S. Bulanov, K. Nishihara, *et al.*, « Proposed double-layer target for the generation of high-quality laser-accelerated ion beams », *Physical review letters*, vol. 89, no. 17, p. 175 003, 2002.

[75] S. Fourmaux, S. Buffechoux, B. Albertazzi, *et al.*, « Investigation of laser-driven proton acceleration using ultra-short, ultra-intense laser pulses », *Physics of Plasmas*, vol. 20, no. 1, 2013.

[76] D. Raffestin, L. Lecherbourg, I. Lantuéjoul, *et al.*, « Enhanced ion acceleration using the high-energy petawatt petal laser », *Matter and Radiation at Extremes*, vol. 6, no. 5, 2021.

[77] R. A. Simpson, G. Scott, D. Mariscal, *et al.*, « Scaling of laser-driven electron and proton acceleration as a function of laser pulse duration, energy, and intensity in the multi-picosecond regime », *Physics of Plasmas*, vol. 28, no. 1, p. 013 108, 2021.

[78] M. Passoni, V. Tikhonchuk, M. Lontano, and V. Y. Bychenkov, « Charge separation effects in solid targets and ion acceleration with a two-temperature electron distribution », *Physical Review E*, vol. 69, no. 2, p. 026 411, 2004.

[79] A. Bell, A. Robinson, M. Sherlock, R. Kingham, and W. Rozmus, « Fast electron transport in laser-produced plasmas and the kalos code for solution of the vlasov–fokker–planck equation », *Plasma Physics and controlled fusion*, vol. 48, no. 3, R37, 2006.

[80] J. R. Pierce, « Traveling-wave tubes », *The bell System technical journal*, vol. 29, no. 2, pp. 189–250, 1950.

[81] G. Kino and S. Paik, « Circuit theory of coupled transmission systems », *Journal of Applied Physics*, vol. 33, no. 10, pp. 3002–3008, 1962.

[82] C. Lacoste and al., « Dopplight 2 », *To be submitted*, 2023.

[83] I. Lantuéjoul, B. Vauzour, A. Duval, *et al.*, « Absolute measurement of proton spectra for petal experiments », *In preparation*,

[84] C. K. Birdsall, « Particle-in-cell charged-particle simulations, plus monte carlo collisions with neutral atoms, pic-mcc », *IEEE Transactions on plasma science*, vol. 19, no. 2, pp. 65–85, 1991.

[85] S. Di Fede, M. Magarotto, S. Andrews, and D. Pavarin, « Simulation of the plume of a magnetically enhanced plasma thruster with spis », *Journal of Plasma Physics*, vol. 87, Dec. 2021.

[86] O. Cessenat, « Sophie, an fdtd code on the way to multicore, getting rid of the memory bandwidth bottleneck better using cache », *arXiv preprint arXiv:1301.4539*, 2013.

[87] K. Yee, « Numerical solution of initial boundary value problems involving maxwell's equations in isotropic media », *IEEE Transactions on antennas and propagation*, vol. 14, no. 3, pp. 302–307, 1966.

[88] TOP500. « Top 500 hpc list ». (2023), [Online]. Available: https://www.top500.org//.

[89] J. P. Boris and R. A. Shanny, « Proceedings of the conference on the numerical simulation of plasmas (4th) held at the naval research laboratory, washington, dc on 2, 3 november 1970 », 1971.

[90] H. Childs, « Visit: an end-user tool for visualizing and analyzing very large data », 2012.

[91] E. Lefebvre, N. Cochet, S. Fritzler, *et al.*, « Electron and photon production from relativistic laser–plasma interactions », *Nuclear Fusion*, vol. 43, no. 7, p. 629, 2003.

[92] J. Derouillat, A. Beck, F. Pérez, *et al.*, « Smilei: a collaborative, open-source, multi-purpose particle-in-cell code for plasma simulation », *Computer Physics Communications*, vol. 222, pp. 351–373, 2018.

[93] M. Bardon and al., « Dopplight: an efficient model to study and design helical coil targets for laser-driven ion acceleration », *To be submitted*, 2023.

[94] INRS. « Alls ». (2023), [Online]. Available: https://alls.inrs.ca/.

[95] A. Poyé, J.-L. Dubois, F. Lubrano-Lavaderci, *et al.*, « Dynamic model of target charging by short laser pulse interactions », *Physical Review E*, vol. 92, no. 4, p. 043 107, 2015.

[96] Z. Liu, Z. Mei, D. Kong, *et al.*, « Synchronous post-acceleration of laser-driven protons in helical coil targets by controlling the current dispersion », *High Power Laser Science and Engineering*, vol. 11, e51, 2023.

[97] R. Baartman and D. Yuan, « Space charge neutralization studies in the h-beam », Triumf, Tech. Rep., 1988.

[98] R. Wanzenberg, « Nonlinear motion of a point charge in the 3d space charge field of a gaussian bunch », Dt. Elektronen-Synchrotron DESY, Tech. Rep., May 2010.

[99] S. Kar, H. Ahmed, G. Nersisyan, *et al.*, « Dynamic control of laser driven proton beams by exploiting self-generated, ultrashort electromagnetic pulses », *Physics of Plasmas*, vol. 23, p. 055 711, 2016.

[100] H. Ahmed, S. Kar, G. Cantono, *et al.*, « Investigations of ultra-fast charge dynamics in laser-irradiated targets by a self probing technique employing laser driven protons », *Nuclear Instruments and Methods in Physics Research Section A: Accelerators, Spectrometers, Detectors and Associated Equipment*, vol. 829, pp. 172–175, 2016.

[101] H. Ahmed, S. Kar, A. Giesecke, *et al.*, « Proton probing of laser-driven em pulses travelling in helical coils », *High Power Laser Science and Engineering*, vol. 5, e4, 2017.

[102] E. Aktan, H. Ahmed, B. Aurand, *et al.*, « Parametric study of a high amplitude electromagnetic pulse driven by an intense laser », *Physics of Plasmas*, vol. 26, no. 7, p. 070 701, 2019.

[103] S. Ferguson, P. Martin, H. Ahmed, *et al.*, « Dual stage approach to laser-driven helical coil proton acceleration », *New Journal of Physics*, 2023.

[104] H. Freund, E. Zaidman, and T. Antonsen Jr, « Theory of helix traveling wave tubes with dielectric and vane loading », *Physics of Plasmas*, vol. 3, no. 8, pp. 3145–3161, 1996.

[105] J. Jiao, L. Qiu, L. Zhang, B. Hao, J. Feng, and Y. Wang, « A key design and experiment of a broadband high-power pulsed helix twt », in *2019 International Vacuum Electronics Conference (IVEC)*, IEEE, 2019, pp. 1–2.

[106] J. Freund, M. Kodis, and N. Vanderplaats, « Self-consistent field theory of a helix traveling wave tube amplifier », *IEEE transactions on plasma science*, vol. 20, no. 5, pp. 543–553, 1992.

[107] J. J. Thomson, « Xlvii. on rays of positive electricity », *The London, Edinburgh, and Dublin Philosophical Magazine and Journal of Science*, vol. 13, no. 77, pp. 561–575, 1907.

[108] C. Lamy, « Étude de l'utilisation de réseaux de neurones artificiels pour des calculs de haute performance dédiés à la modélisation du transport de sources énergétiques », Theses, Université de Bordeaux, Nov. 2022. [Online]. Available: https://theses.hal.science/tel-03908443.

[109] D. P. Kingma and M. Welling, « Auto-encoding variational bayes », *arXiv preprint arXiv:1312.6114*, 2013.

[110] D. J. Rezende, S. Mohamed, and D. Wierstra, « Stochastic backpropagation and approximate inference in deep generative models », in *International conference on machine learning*, PMLR, 2014, pp. 1278–1286.

[111] N. Kugland, B. Aurand, C. Brown, *et al.*, « Demonstration of a low electromagnetic pulse laser-driven argon gas jet x-ray source », *Applied Physics Letters*, vol. 101, no. 2, 2012.

[112] P. Bradford, M. Ehret, V. Ospina-Bohorquez, *et al.*, « Emp emission from laser interactions with gas jets », *In preparation*,

[113] P. Bradford, « Emp emission from laser interactions with gas jets », Sep. 2022.

[114] T. Esirkepov, M. Borghesi, S. Bulanov, G. Mourou, and T. Tajima, « Highly efficient relativistic-ion generation in the laser-piston regime », *Physical review letters*, vol. 92, no. 17, p. 175 003, 2004.

[115] N. Dover, C. Palmer, M. Streeter, *et al.*, « Buffered high charge spectrally-peaked proton beams in the relativistic-transparency regime », *New Journal of Physics*, vol. 18, no. 1, p. 013 038, 2016.

Appendix

Appendix A

Design of a new helical coil with controlled dispersion

In this appendix, are the PIC simulations and DoPPLIGHT calculations results for different geometries of coils with constant radius and pitch. We can observe that, for all these geometries, we observe the same behaviour of the current when we surround the helical coil with a tube with a drastic reduction of the dispersion and the appearance of a positive current pulse going at $V = 1.2\ V_{\mathrm{HC}}$.

A.1 HC Parameters: L=40 mm, a=0.6 mm and h=0.3 mm

A.1.1 ALLS input

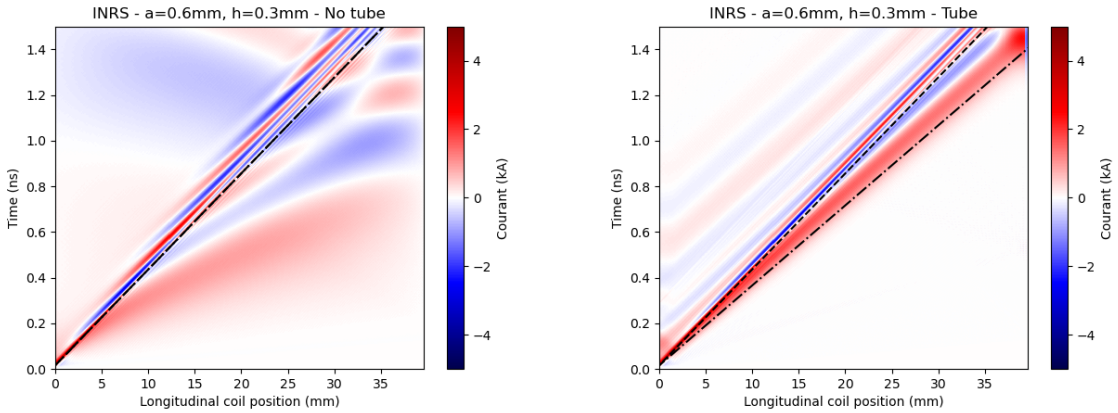

(a) (b)

Figure 1 – PIC simulation of the current pulse intensity in kA for a helical coil (a) without tube and (b) with tube as a function of time and along the HC axis. The particles features are defined in Table 2.2 for ALLS. The HC parameters are: length $L = 40$ mm, radius in the heart of the coil $a = 0.6$ mm, external radius 0.7 mm and step $h = 0.3$ mm with a tube of radius $b = 1$ mm. The dashed line corresponds to V_{HC}, the geometrical speed of the HC, the dash-dotted line corresponds to $V = 1.2\ V_{\mathrm{HC}}$.

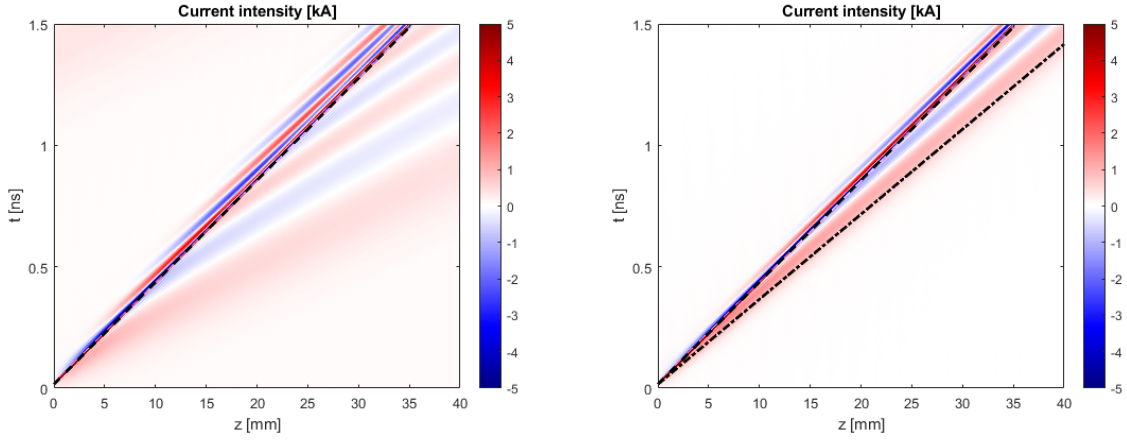

(a) (b)

Figure 2 – DoPPLIGHT calculation of the current pulse intensity in kA for a helical coil (a) without tube and (b) with tube as a function of time and along the HC axis. The particles features are defined in Table 2.2 for ALLS. The current is defined analytically by a gaussian with FWHM $\tau_{FWHM} = 3$ ps and amplitude $I_0 = 7$ kA at $z = 0$ mm, delayed with respect to the particule emission by 6 ps. The HC parameters are: length $L = 40$ mm, radius of the thin cylinder $a = 0.6$ mm and step $h = 0.3$ mm with a tube of radius $b = 0.9$ mm. The dashed line corresponds to V_{HC}, the dash-dotted line corresponds to $V = 1.2\ V_{\mathrm{HC}}$.

A.1.2 LULI2000 input

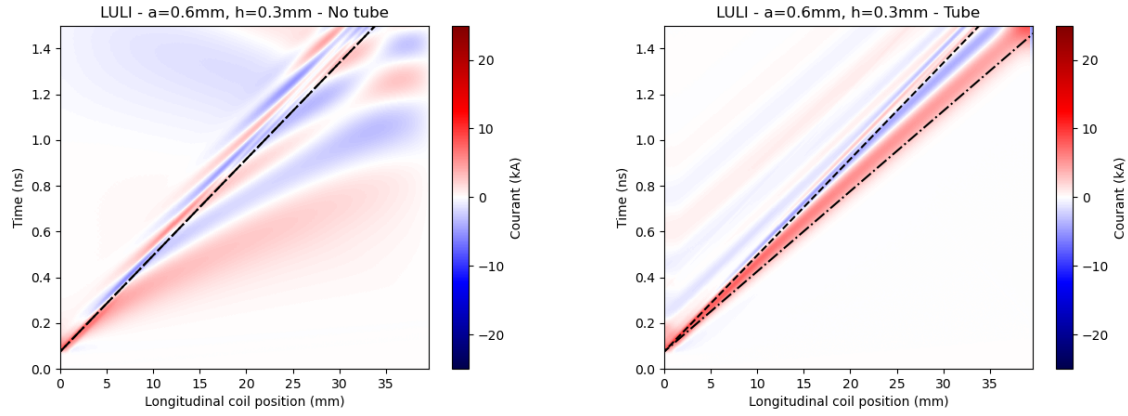

(a) (b)

Figure 3 – PIC simulation of the current pulse intensity in kA for a helical coil (a) without tube and (b) with tube as a function of time and along the HC axis. The particles features are defined in Table 2.2 for LULI. The HC parameters are: length $L = 40$ mm, radius in the heart of the coil $a = 0.6$ mm, external radius 0.7 mm and step $h = 0.3$ mm with a tube of radius $b = 1$ mm. The dashed line corresponds to V_{HC}, the geometrical speed of the HC, the dash-dotted line corresponds to $V = 1.2\ V_{\mathrm{HC}}$.

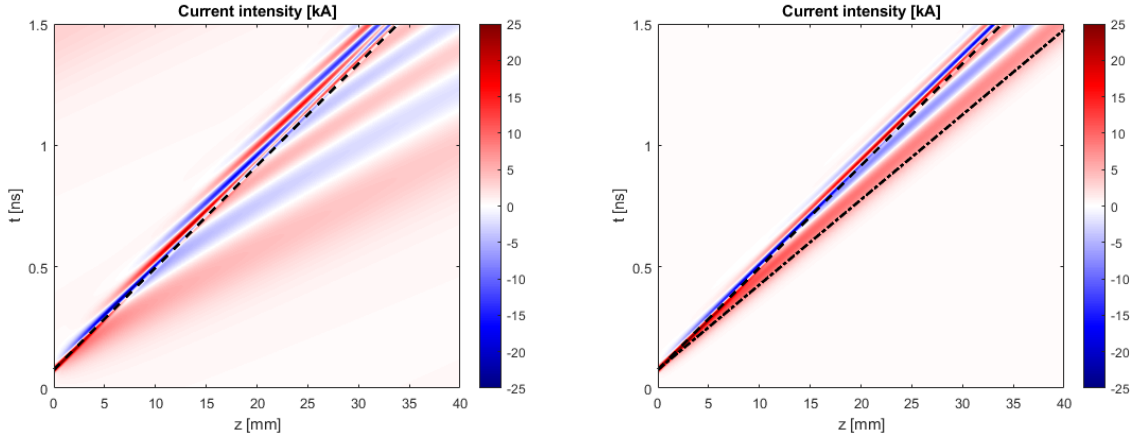

(a) (b)

Figure 4 – DoPPLIGHT calculation of the current pulse intensity in kA for a helical coil (a) without tube and (b) with tube as a function of time and along the HC axis. The particles features are defined in Table 2.2 for LULI. The current is defined analytically by a gaussian with FWHM $\tau_{FWHM} = 8.5$ ps and amplitude $I_0 = 30$ kA at $z = 0$ mm, delayed with respect to the particule emission by 6 ps. The HC parameters are: length $L = 40$ mm, radius of the thin cylinder $a = 0.6$ mm and step $h = 0.3$ mm with a tube of radius $b = 0.9$ mm. The dashed line corresponds to V_{HC}, the dash-dotted line corresponds to $V = 1.2\ V_{\mathrm{HC}}$.

A.2 HC Parameters: L=40 mm, a=0.5 mm and h=0.5 mm

A.2.1 LULI2000 input

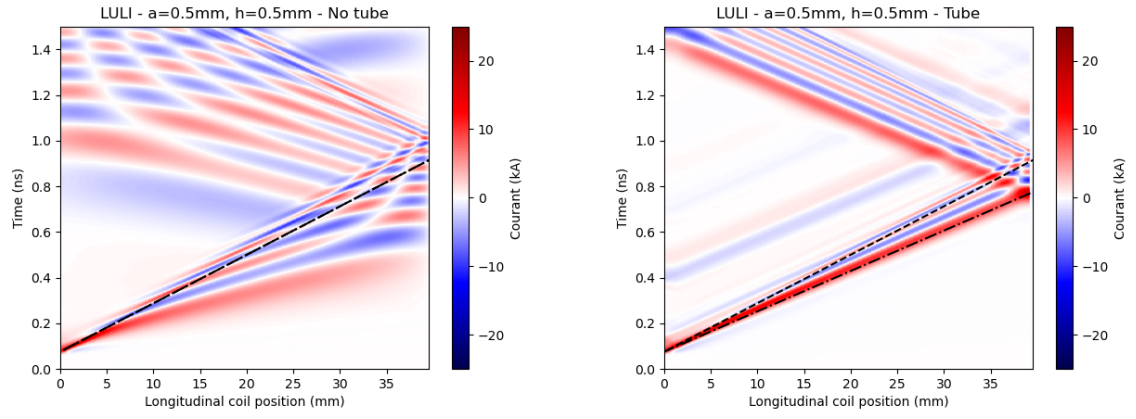

(a) (b)

Figure 5 – PIC simulation of the current pulse intensity in kA for a helical coil (a) without tube and (b) with tube as a function of time and along the HC axis. The particles features are defined in Table 2.2 for LULI. The HC parameters are: length $L = 40$ mm, radius in the heart of the coil $a = 0.5$ mm, external radius 0.6 mm and step $h = 0.5$ mm with a tube of radius $b = 0.9$ mm. The dashed line corresponds to V_{HC}, the geometrical speed of the HC, the dash-dotted line corresponds to $V = 1.2\ V_{\mathrm{HC}}$.

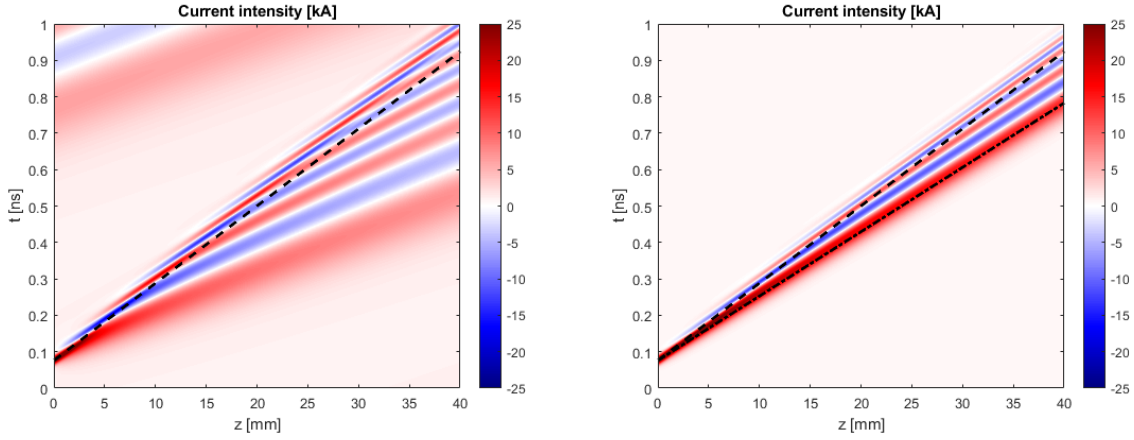

(a) (b)

Figure 6 – DoPPLIGHT calculation of the current pulse intensity in kA for a helical coil (a) without tube and (b) with tube as a function of time and along the HC axis. The particles features are defined in Table 2.2 for LULI. The current is defined analytically by a gaussian with FWHM $\tau_{FWHM} = 8.5$ ps and amplitude $I_0 = 30$ kA at $z = 0$ mm, delayed with respect to the particule emission by 6 ps. The HC parameters are: length $L = 40$ mm, radius of the thin cylinder $a = 0.5$ mm and step $h = 0.5$ mm with a tube of radius $b = 0.8$ mm. The dashed line corresponds to V_{HC}, the dash-dotted line corresponds to $V = 1.2\ V_{\mathrm{HC}}$.